

Institut für Physikalische Chemie  
Fakultät Mathematik und Naturwissenschaften  
Technische Universität Dresden

**Molybdenum chalcogenide nanowires as building blocks of  
nanodevices**

Dissertation  
zur Erlangung des  
Doktorgrades der Naturwissenschaften  
(Doctor rerum naturalium)

vorgelegt von  
Diplomphysiker Igor Popov  
geboren in Belgrad

Dresden 2008



Eingereicht im Juni, 2008

1. Gutachter: Prof. Dr Gotthard Seifert
2. Gutachter: Prof. Dr Gianaurelio Cuniberti
3. Gutachter: Prof. Dr Milan Damnjanovic

Verteidigt im November, 2008

## Table of contents

1	Introduction.....	5
1.1	Demand of industry.....	5
1.2	Molecular electronics and nanotechnology as parts of the new paradigm .....	7
1.2.1	Advantages of molecular electronics and nanotechnology.....	8
1.2.2	Disadvantages of new paradigm .....	9
1.3	Potential ancestors of silicon .....	11
1.3.1	Conjugated carbon-based molecules.....	11
1.3.2	Carbon nanotubes (CNTs) .....	11
1.3.3	Other candidates.....	12
1.4	Potential of molybdenum chalcogenide nanostructures for use in the electronic devices.....	12
1.4.1	Mechanical response.....	13
1.4.2	Nanowire-electrode contacts.....	14
2	Methodology.....	17
2.1	Density functional theory.....	17
2.1.1	First Hohenberg-Kohn theorem: proof of existence .....	17
2.1.2	Second Hohenberg-Kohn theorem: variational principle .....	18
2.1.3	The Kohn-Sham equations.....	18
2.1.4	Local-density approximation (LDA) .....	20
2.1.5	Generalized gradient approximation (GGA) .....	21
2.1.6	Pseudopotential .....	23
2.2	Density-functional based tight-binding method.....	25
2.2.1	Kohn-Sham equations in DFTB.....	26
2.2.2	Repulsion potential .....	29
2.2.3	Matrix form of the <i>Kohn-Sham</i> equations .....	30
2.2.4	Interatomic forces .....	31
2.2.5	Second-order self-consistent charge extension (SCC-DFTB) .....	32
2.3	Parameters for DFTB calculations.....	35
2.3.1	Basic DFTB parameters.....	35
2.3.2	Repulsion potential .....	36
2.3.3	Stability of gold surface .....	37
2.4	Formalism of Green's functions .....	40
2.4.1	Retarded and advanced Green's functions.....	40
2.4.2	Relation between $G^R$ and $G^A$ .....	42
2.4.3	Self-energy .....	43
2.4.4	Spectral function .....	47
2.4.5	Density of states in open systems .....	48
2.4.6	Electronic current.....	50
3	Unique structural and transport properties of molybdenum chalcogenide nanowires.....	55
3.1	Introduction.....	55
3.2	Computational details .....	56
3.3	Details on the atomic structure .....	57
3.4	The electronic structure.....	63
3.5	Conclusions.....	66
4	Reliability of the DFTB method for description of energetic and electronic properties of the molybdenum chalcogenide nanowires.....	69

4.1	Comparison of binding energies .....	69
4.2	Comparison of electronic structure of $\text{Mo}_6\text{S}_{6-x}\text{I}_x$ nanowires calculated with the DFT and DFTB methods .....	70
4.3	Conclusions.....	75
5	Structural and electronic response of $\text{Mo}_6\text{S}_6$ nanowire to mechanical deformations .....	77
5.1	Introduction.....	77
5.2	Computational details .....	78
5.3	The investigated geometries of the mechanically deformed nanowires .....	78
5.4	The energetic and structural properties.....	80
5.5	The electronic transmission .....	81
5.6	The origin of the metal-semiconductor transition in bent $\text{Mo}_6\text{S}_6$ nanowire .....	82
5.7	Conclusions.....	87
6	Structural and electronic properties of $\text{Mo}_6\text{S}_8$ clusters deposited on a Au (111) surface .....	89
6.1	Introduction.....	90
6.2	Computational details .....	92
6.3	Geometries .....	94
6.4	Structural properties.....	96
6.5	Binding energies .....	100
6.6	Potential energy surface.....	102
6.7	Classical model for the self-assembly.....	105
6.8	Electronic structure .....	109
6.9	Discussion and conclusions .....	115
7	Unique electronic and transport properties of contacts between $\text{Mo}_6\text{S}_6$ nanowires and gold electrodes .....	119
7.1	Introduction.....	120
7.2	Computational details .....	121
7.3	Electronic and transport properties .....	124
7.3.1	Transport properties .....	124
7.3.2	Electronic properties .....	126
7.3.3	The potential barrier.....	128
7.4	Conclusions.....	129
8	Summary .....	131
9	Bibliography .....	135

## 1 Introduction

*The physics and chemistry of molybdenum chalcogenide nanowires have been investigated during last decades. However, their potential for building electronic devices has not been addressed so far. This is the primary aim of this thesis: to investigate the potential of the molybdenum chalcogenide systems as building blocks in electronic nanometer-sized devices. Before proceeding with very interesting results of this research, in this chapter an overview will be given of molecular electronics and nanotechnology in order to get insight to the motivation for this work as well as to put it on wider concept of current and future science and technology.*

### 1.1 Demand of industry

Accelerating change from positive feedback is a common pattern in science, technology and evolution. We entered an era of exponential growth in biotechnology, molecular engineering, supercomputing, nanotechnology, etc. The combination of these formerly discrete domains further increases our rate of learning and our engineering capabilities. This inspires new approaches, like bottom-up manufacturing of electronic devices, exploiting self-assembling of molecules, the feature that is a basic mechanism of most biological processes. Silicon microelectronics has undergone amazing miniaturization during the past decades, leading to dramatic improvements in computer development and therefore computational capacity and speed. The main measure of the miniaturization progress is the empirical Moore's law<sup>1</sup>, which states that the number of transistors in a silicon microchip doubles every 18 months. Intriguingly, this trend is known to be valid since 60-ties, when the transistor revolution has begun. However, miniaturization of traditional semiconductor chips is approaching some fundamental physical limits. One of the problems is the simultaneous exponential increase of the power dissipation with the increase of the transistor density. Just 15 years ago, an average microchip dissipated only few watts per square centimeter, and the external cooling was not necessary. Modern microprocessors dissipate hundreds of W/cm<sup>2</sup>,

and even the air-cooling is often not enough to keep the microchip at nominal working temperature. Another physical limit is the atomic limit. Intel<sup>1</sup>, the leader company in microelectronic industry, has recently started a serial production of new microprocessors manufactured with 45 nm lithographic process. The thickness of the gate oxide in transistors is only 3 atomic layers, which is achieved using nanostructuring of *high-k* dielectrics. The quantum mechanical tunneling is a cause for parasitic gate current at the atomic scale of the gate oxide, which can approach and even exceed the channel current so that transistors cannot be controlled by the gate anymore. Another issue is the cost of fabrication, which is doubling every three years. The manufacturing process is more demanding for each generation of microprocessors. The cost of building a new factory for the production of the microprocessors is projected to reach 15 to 30 billion dollar by 2010<sup>2</sup> and could be as much as 200 billion dollar by 2015<sup>3</sup>. As devices increase in complexity, defect and contamination control become even more important since defect tolerance is very low (nearly every device must work perfectly). For instance, impurities in the chemicals that are used in the fabrication process, such as sulfuric acid, are measured in the part-per-billion (ppb) range. With decrease in feature size, the presence only of a few ppb of metal contamination could lead to low chip yields. Therefore, the industry has been driving a progress of chemical production with only part-per-trillion (ppt) contamination levels, raising the cost of the materials. Depending on the complexity of the device, the thousands of individual processing steps might be required<sup>4</sup>. It can take 30 to 40 days for a single wafer to complete the manufacturing process. Many of the steps are cleaning steps, requiring thousands of liters of ultra-pure water per minute<sup>5</sup>. Thus, during next decade, the life of Moore's law could approach its end, if the current technology will not adopt some fundamentally different paradigm.

---

<sup>1</sup> [www.intel.com](http://www.intel.com)

## ***1.2 Molecular electronics and nanotechnology as parts of the new paradigm***

The electronic and other devices that are shrunk down to the nanometer size have properties not typical for their larger counterparts. The reason for this is that small systems behave under quantum mechanical rules, which become more prominent as the spatial dimensions of the devices decrease. This can significantly affect the normal operation of the small devices. A fundamental new paradigm appeared in the scientific community and the industry: Instead of pertaining the common design of the classical electronic devices, it may be advantageous to exploit these appearing quantum phenomena for unique functions of the nanometer-scaled devices. Possible ancestors of the post-silicon paradigm are the molecular electronics and the nanotechnology, with the goal to make advantage of specific properties of the molecular and the other quantum systems in order to improve the present solid-state electronic devices. The most recent miniaturization of electronic devices suggested that ultimately single molecules and nanotubes might be used as building blocks in the future applications. We have witnessed a great amount both of fundamental and applied research in molecular electronics<sup>6-18</sup>. The understanding of the synthesis and mechanisms of the molecular devices is rapidly growing today. Some commercial products based on the new paradigm are already in their beta testing stage. For example, Nantero<sup>2</sup> employs carbon nanotubes suspended above metal electrodes on silicon to create high-density nonvolatile memory chips. Hewlett Packard<sup>3</sup> and ZettaCore<sup>4</sup> produce memory elements from self-assembled organic molecules along pre-patterned regions of exposed silicon. Since the '80-ties and the discovery of scanning tunneling microscopy (STM) by Gerd Binnig and Heinrich Rohrer (at IBM Zürich), it has become possible to manipulate a single atom by a STM tip. Recently, this manipulation is raised even to a higher level: Using an STM to manipulate individual carbon monoxide molecules, IBM built a 3-input sorter by arranging those molecules precisely on a copper surface. It is more than 200000 times smaller than the equivalent circuit based on the traditional silicon technology.

---

<sup>2</sup> [www.nantero.com](http://www.nantero.com)

<sup>3</sup> [www.hp.com](http://www.hp.com)

<sup>4</sup> [www.zetacore.com](http://www.zetacore.com)

### 1.2.1 Advantages of molecular electronics and nanotechnology

Several advantages of molecular electronics and nanotechnology over the modern silicon technology are known so far:

**Size:** The characteristic scale for the quantity of molecules in a substance is Avogadro number  $6.022 \cdot 10^{23}$  1/mol, which is larger than total number of transistors in all-electronic devices produced till today. Within a common area of  $1 \text{ cm}^2$  of an integrated circuit it is possible to integrate approximately  $10^{14}$  typical molecules spanning 1-3 nm each, which are six orders of magnitude larger than the density of transistors in the modern devices.

**Heat dissipation:** The inefficiency of the modern silicon-based transistor for the current transmission appears in the high heat dissipation. In contrast, the devices at nanometer scale can obey different physics for electronic transport. The mean free path of the electrons for the inelastic scattering in carbon nanotubes exceeds several hundred nanometers, which is longer than the dimensions of the device. Without the inelastic scattering the energy is not transferred from the current to the crystal lattice, which enhances the conductivity of the device and decreases the heat dissipation.

**Manufacturing cost:** Exponential increase of the number of transistors in modern microprocessors introduces large difficulties for the conventional lithographical methods, which processing time becomes significantly time consuming. This traditional *top-down* approach that involves the carving of raw material into a functional element is non applicable to molecular electronics any longer. A new promising approach, usually referred to as a *bottom-up* approach, offers a new paradigm for nanoelectronic devices. Like in chemical reactions where large quantity of molecules interact and make new compounds, certain type of molecules may self-assemble onto a surface, or even build 3D structures, resulting in much higher complexity that is incomprehensible for the lithographic techniques. Self-assembling techniques are inspired by the natural bio-processes occurring in biological systems.



### 1.2.2 Disadvantages of new paradigm

Besides the obvious advantages, molecular electronics and nanotechnology face some issues that have to be solved in order to make the applications of nanometer-sized devices in future technology possible. Four major problems are listed in following:

**Addressability:** In the currently used integrated circuits each individual transistor can be addressed and connected to power supply, which is more difficult for the large number of molecules. The problem of addressability also appears in the connection of nano- and macro-elements, which is still not fully understood at the fundamental level. Additionally, self-assembled monolayers are usually not homogeneous, where some regions of the substrate are covered better than another. The lack of the homogeneity can be, for instance, caused by the uneven relaxation of the substrate, or topological defects like existence of edges.

**Determinism:** Apart from the addressability of individual molecules, the interfaces between molecules and addressing nodes can become unpredictable, because of the undeterministic nature of the quantum systems to which molecule-electrode contacts belong.

**Heat dissipation:** Depending on the molecule and its chemical and physical properties, a strong electron-phonon coupling for device with  $10^{14}$  molecules may result in huge heat dissipation.

**Contact properties:** The chemical potential should be equal across the interface between the molecule and the metal (electrode) in isolated systems. In order to balance their chemical potentials, electronic levels of the molecule and metal shift with respect to each other, which usually leads to redistribution of the electronic charge between the molecule and the surface. A consequence of this redistribution is an electric dipole formed at the interface. The electric current through such contacts is often not linear with respect to applied voltage, i.e. the contacts are usually not *Ohmic*-like. On the other side, the contacts may influence significantly transport properties of the nanometer-sized devices, which is in clear contrast to the properties of usual macroscopic electronic devices. Ideally, the contacts should be perfectly transparent for the injection of the current through the interfaces. Thus, one seeks a

contact that obeys Ohm's law <sup>19</sup> with low resistance as possible. Such properties of the contacts are usually not easy to achieve.

One of the possible solutions for these problems is considered to be the so called *Nanocell* <sup>16</sup>. In this approach, the conjugated carbon-based molecules are self-assembled in a network, whereas the exact position of each individual molecule is not known. Only a small number of input and output nodes (molecules) of this system have to be addressable, i.e. accessible by the rest of the electronic circuit. Hence, the problem of addressability could be elegantly solved within this approach. The rest of *Nanocell* network could be a *black box*, which functionality may be trained for certain logical operation, like neural networks, by accessing only the input and output nodes (for details see ref. <sup>16</sup>). Therefore, the *Nanocell* could produce deterministically a desired output for each input signals it is trained for. As stated above, this is difficult to achieve using only one individual molecule (because of uncertainty of the molecule and the molecule-electrode contacts). The idea for *Nanocell* is only a theoretical concept up to date, and experimental support does not exist yet. Concerning now only the issue of the heat dissipation, three solutions have been suggested <sup>16</sup>:

1. Utilizing molecules with low enough electron-phonon coupling;
2. Utilizing systems which consume 1-100 electrons per bit of information, against to 15000-20000 electrons per bit in the present devices;
3. Utilizing systems that transmit information not by the electric current, but rather by means of some other transfer of the information (an example of this approach is *quantum cellular automata* <sup>16</sup>).

### **1.3 Potential ancestors of silicon**

#### **1.3.1 Conjugated carbon-based molecules (CCBMs)**

Carbon nanotubes (CNTs) and various conjugated carbon-based molecules (CCBMs) have been so far considered as potential building blocks for molecular electronic devices. These systems have intriguing physical and chemical features. For instance, CCBMs can be either isolating or conducting depending on angle between their phenyl rings. If they are coplanar, a molecule is conducting because of existence of the delocalized electronic state encompassing p- $\pi$  electrons of the phenyl rings. If the rings are twisted by a non-zero angle, the delocalized state vanishes and good conductance disappears. It was shown by Reed *et al.*<sup>14</sup> that conformation of some conjugated molecules could be engineered by applying a bias voltage with a certain threshold amplitude and a certain direction with respect to the orientation of the molecules. This switching behavior was experimentally demonstrated<sup>14</sup>. The chemistry Nobel Prize in 2000 given to A. J. Heeger, A.G. MacDiarmid, and H. Shirakawa for the “discovery and development of conductive polymers” was a clear recognition by the community of the importance of obtaining conjugated one-dimensional metallic systems.

#### **1.3.2 Carbon nanotubes (CNTs)**

CNTs are other structures, which physical and chemical properties attract immense interest of the scientific community since their discovery in 1991<sup>20</sup>. Carbon nanotube is a honeycomb lattice rolled into a hollow cylinder with a nanometer-sized diameter and length ranging from a few nm up to  $\mu\text{m}$ . As there are infinite possibilities for rolling a sheet into a cylinder, which defines the tube chirality, a large variety of possible helical geometries with different diameters and physical properties can be potentially created. For instance, the electronic and transport properties crucially depend on the diameter and tube chirality. CNTs can be metallic or semiconducting with direct or indirect band gap. These quasi-1D systems are mechanically very stable with axial stiffness exceeding the stiffness of steel by six orders of magnitude. It is very difficult to synthesize a single CNT as a rolled graphene sheet. So

called multi-wall CNTs (MWCNTs, usually synthesized in laboratories), represent nanotubes, commonly with different chiralities, axially nested one into another. Since the electronic and transport properties of CNTs are very sensitive to their chirality, the features of MWCNT are usually tedious to determine, and the routine synthesis of MWCNT with desired properties is still not achieved. Besides, even a single impurity of CNT can drastically change its structural and transport properties. So called single-wall CNTs (SWCNTs)<sup>21</sup> often group into bundles due to mutual Van der Waals interaction. The electronic properties of individual CNT in the bundle are affected by inter-tube interactions. Separating a single nanotube from the bundle is not a trivial task and it needs additional efforts. However, for the applications in nanodevices, well-controlled properties of CNTs are imperative. Thus, only the SWCNT with precisely defined chirality and diameter can be used in nanodevices.

### **1.3.3 Other candidates**

Apart from conjugated carbon-based molecules and carbon nanotubes on one side, silicon, gallium-arsenide, boron-nitrogen, etc. nanowires and nanotubes have been also extensively addressed by the scientific community. However, these systems will not be considered in the thesis.

## ***1.4 Potential of molybdenum chalcogenide nanostructures for use in the electronic devices***

*The physics and chemistry of molybdenum chalcogenide nanowires have been in detail investigated during last decades. However, their potential for building electronic devices has not been addressed so far. This is the primary aim of the thesis: to investigate the possibility for employing the molybdenum chalcogenide systems as building blocks in electronic nanometer-sized devices. The mechanical, electronic and transport properties of the systems will be compared to the corresponding systems based on carbon nanotubes (CNTs) and conjugated carbon-based molecules (CCBMs). The research will be focused first*

*on the intrinsic properties of ideal molybdenum chalcogenide nanowires, their mechanical response, and finally on properties of their contacts with the noble metal electrodes.*

#### **1.4.1 Mechanical response**

The electronic and transport properties of CCBMs and CNTs exhibit very interesting features when they undergo structural changes. For instance, the conductance of a tolaniethiol molecule depends on the angle between its phenyl rings<sup>16</sup>. The molecule is in the conducting state when its phenyl rings lie in the same plane, and the conduction-insulating state transition occurs upon rotating the phenyl rings with respect to each other. In the uni-planar molecular configuration the p- $\pi$  orbitals from neighboring phenyl rings (orthogonal to these phenyl rings) strongly overlap; hence a well-conducting, delocalized state is constituted along the molecule. In contrast, the rotation of the rings breaks the overlap between the p- $\pi$  orbitals, therefore the delocalization is lowered and the molecule becomes insulating<sup>16</sup>.

The mechanical deformations of CNTs also show very interesting effects, and the twisting of CNTs is the most intriguing one. It has been recently shown in the experiments by Karni *et al.*<sup>22</sup> that the conductance of twisted CNTs oscillates with change of the torsion angle. These oscillations are explained<sup>22</sup> considering a model in the reciprocal lattice, which will be briefly explained in the following: Depending on the diameter and chirality of the nanotube that determine the point group of the nanotube, the sub-bands may, or may not, include the corners of Brillouin zone, which leads to metallic or semiconducting nanotubes, respectively. Torsion of CNT deforms its Brillouin zone, which corners can move closer or away from the nearest sub-band. This opens or closes a band gap, i.e. causes metal-semiconductor and semiconductor-metal transitions.

In the present thesis, the electronic response of the molybdenum sulfide nanowires to twisting is investigated. In contrast to the response of CNTs, which conductance oscillates with change of the torsion angle, the opening of the band gap in the twisted molybdenum sulfide wire monotonically increases with the increase of the torsion angle. These wires have simpler geometric and electronic structures than CNTs, and the metal-semiconductor transition has a genuinely simple explanation, which will be discussed in detail.

Other type of deformation, bending, also investigated in this thesis as it will be shown below, does not introduce any significant changes to the electronic and transport properties of the molybdenum sulfide nanowire, which remains metallic even under curvatures larger than ones observed in the experiments with the isoelectronic  $\text{Mo}_6\text{Se}_6$  wires<sup>23</sup>. In contrast to CNTs, the molybdenum sulfide nanowires are more flexible, i.e. the energy necessary for their bending is by order of magnitude smaller than in typical CNT. This indicates that nanowires may easily adapt to very fine features of a nanostructured template, and hence be used as nanocables.

Therefore, the molybdenum sulfide nanowires possess unique properties that make them suitable for the application in the nanometer-sized electronic devices. On one hand, the switching nature of the twisted nanowire allows one to use it as a logic device. At zero Kelvin, the wire can be in one of only two distinct states: conducting and insulating. At higher temperatures, the gap may determine the resistance of the wire, which increases linearly with the torsion angle. Thus, the wire can be used as a nano-potentiometer, an analog device. Although nano-potentiometers are not commonly present in high-tech devices in the modern digital age, they might be employed in larger extent in the new paradigm about which was discussed before. On the other hand, the bent nanowire remains metallic irrespective to its curvature, which is necessary to transmit electronic signals and informations across integrated electronic circuits in flexible and secure way.

#### 1.4.2 Nanowire-electrode contacts

In the macroscopic devices the resistance at interface between the electrode and the rest of the device is usually just a negligible perturbation, while the influence of the contact can be an important issue for the nanosystems with relatively small number of channels<sup>17</sup>. Even reflectionless contacts obey a fundamental resistance:

$$G_C^{-1} = \frac{h}{2e^2} \cdot \frac{1}{M} \approx \frac{12.9 \text{ k}\Omega}{M},$$

where  $M$  is number of transverse conducting modes in the wire. When  $M$  is large enough, like in the macroscopic devices, the contact resistance rapidly decays. However, the number of modes becomes significantly smaller in molecular and nanowires, where the energy difference between electronic levels (i.e. transverse modes) is much larger than in macroscopic systems. Hence, the contact resistance is significant and the number of modes accessible by applied bias is by many orders of magnitude smaller in nanoscale systems than in macrosystems. The question how contact conductance influences the overall transport properties of nanodevices is addressed in various studies, where it has been shown that the calculated conductance changes over several orders of magnitude against arbitrary variation of the contact coupling and/or geometry<sup>18, 24-27</sup>. Theoreticians also tackled the conundrum of the interfaces. A few disputed its significance in molecular conduction, but the manner of its representation in the calculation evoked a wide range of approaches and criticisms<sup>28</sup>. The problem can be approached by treating the interface as a simple Schottky–Mott interface, where the vacuum levels are simply aligned, and the Fermi level determines the electron and hole barriers. However, this neglects the charge transfer across the interface, which causes a vacuum level shift and, thus, an interface dipole is formed. Experimentally, ultraviolet photoemission spectroscopy (UPS) has been used to determine this shift<sup>29</sup>, which has shown that interface dipole barriers are formed at nearly all interfaces<sup>30</sup>. The nature of the dipole is determined by the extent of the charge transfer between the metal and the molecule and by the effect of the displacement and rearrangement of the metal surface charge<sup>30</sup>. Several studies noted the significance of the angle at which certain molecules were fixed to the contact, suggesting that the  $\pi$ -orbital coupling were maximized when these molecules lied orthogonal to the surface plane<sup>31</sup>. In order to represent the statistical distribution of experimental configurations in the best possible way, multiple calculations over a variety of angles have been performed to understand the conductance dependence<sup>32</sup>. Because of the importance of the contact geometry for the transport properties, in the present thesis the geometry of contacts between molybdenum chalcogenide nanowires and gold electrodes is analyzed in detail, including structural, electronic and transport properties.

Thiol end-groups are often employed in experiments because they can be readily attached to gold. The gold-thiol attachment rises further controversy. Results of various theoretical calculations specified the most energetically favorable contact to be the fcc-hollow site<sup>33, 34</sup> and the bridge-like position (between fcc-hollow and bridge sites)<sup>35</sup>, while

the experimental studies favor the on-top site <sup>36</sup>. Another theoretical study suggests that lateral degrees of freedom preclude the preference of one contact over another <sup>37</sup>. Some studies that examined conduction through all varieties of contacts report better conductance at the hollow site and bridge positions, whereas on-top site is noted for lower conduction, higher sensitivity to tilting angles, and highly nonlinear current-voltage behavior <sup>38, 39</sup>. Yet others find better conduction properties at the on-top contacts compared to the hollow site <sup>26, 40, 41</sup>. It has been suggested that the hydrogen atoms may not always detach upon sulfur attachment to gold, thereby influencing this contact in yet another unexpected way <sup>42</sup>.

In the present thesis, the investigated nanowires comprise sulfur atoms as their integral part, which bind the nanowires to gold electrodes. Opposite to the usual thiol bonds that are present in devices made of conjugated carbon-based molecules, sulfur atoms are electronically and spatially distinct from the rest of the device, particularly from the conduction channels. This feature is unique in molecular electronics, hence a special effort is made in this thesis to fully understand the physics of the novel contacts and their influence on the transport properties.

The theoretical methods that have been used for the calculations of all properties in the thesis will be introduced in **Chapter 2**. The unique intrinsic properties of the ideal molybdenum chalcogenide nanowires are investigated in **Chapter 3**. Their exceptional advantages with respect to CNTs are emphasized in this, as well as in **Chapter 5**, where the response on mechanical deformations of the molybdenum sulfide nanowires is examined. After first results obtained in **Chapter 3** that are calculated with density functional theory, they are compared with results obtained with an approximated density-functional tight-binding method in **Chapter 4**, in order to gain an insight in reliability of this method for description of molybdenum chalcogenide structures. A detailed analysis of the molybdenum sulfide clusters deposited on a gold surface is given in **Chapter 6**. The relaxed structural geometries that are obtained in this chapter are employed in **Chapter 7**, where the electronic transport properties between molybdenum sulfide nanowires and gold electrodes are examined. General conclusions about the work are derived in **Chapter 8**.



## 2 Methodology

### 2.1 Density functional theory

Density functional theory was born in 1964 when a landmark paper<sup>43</sup> by Hohenberg and Kohn appeared in the Physical Review. The most important results of their study are two theorems, which opened the possibility of reviewing the traditional quantum chemical methods.

#### 2.1.1 First Hohenberg-Kohn theorem: proof of existence

According to the Hohenberg-Kohn theorem the external potential  $V_{ext}(\mathbf{r})$ , to within a constant, is a unique functional of  $\rho(\mathbf{r})$ . Since, in turn  $V_{ext}(\mathbf{r})$  fixes Hamiltonian, the many-particle ground state is a unique functional of  $\rho(\mathbf{r})$ . In other words, there cannot be two different  $V_{ext}(\mathbf{r})$  that yield the same ground state electron density.

Since the complete ground state energy is a functional of the ground state electron density, so must be its individual components, hence the total energy functional can be written as

$$E_0[\rho_0] = T[\rho_0] + E_{ee}[\rho_0] + E_{Ne}[\rho_0]. \quad (1)$$

It is convenient at this point to separate this energy expression into the part that depends on the specifics of actual system, i.e., the potential energy due to the nuclei-electron attraction,  $E_{Ne}[\rho_0] = \int \rho_0(\mathbf{r}) V_{Ne} d\mathbf{r}$ , and the system-independent part:

$$E_0[\rho_0] = \int \rho_0(\mathbf{r}) V_{Ne} d\mathbf{r} + F_{HK}[\rho_0], \quad (2)$$

where  $F_{HK}[\rho_0] = T[\rho_0] + E_{ee}[\rho_0]$  represents the system-independent part. However, both functionals, the exact form of the kinetic energy  $T[\rho_0]$  and the electron-electron interaction

$E_{ee}[\rho_0]$  are not known, which represent the major challenge in the density functional theory. It is interesting to notice that the ground state electron density uniquely determines the Hamiltonian operator, which makes all states of the system, including excited ones. The density functional theory is usually considered to be valid only for the ground state, which is a consequence of the second *Hohenberg-Kohn* theorem.

### 2.1.2 Second Hohenberg-Kohn theorem: variational principle

According to the second Hohenberg-Kohn theorem  $F_{HK}[\rho]$  gives the lowest total energy of the system if and only if the input density is the true ground state density,  $\rho_0$ . In other words that means for any other electron density  $\tilde{\rho}(\mathbf{r})$  associated with the external potential  $V_{ext}(\mathbf{r})$ , the energy obtained from the functional (1) represents an upper bound to the true ground state energy  $E_0$ . This  $E_0$  can be obtained from the functional (1) if and only if the exact ground state density is inserted in Eq. (2).

### 2.1.3 The Kohn-Sham equations

The central idea originated from *Kohn* and *Sham* is the realization that most of the problems in direct density functionals (e.g. the *Thomas-Fermi* method) are connected with the kinetic energy functional part. Realizing that orbital-based approaches (e.g. the Hartree-Fock) perform much better in this respect, Kohn and Sham introduced the concept of a non-interacting reference system built from a set of orbitals (i. e., one electron functions) such that the major part of the kinetic energy can be computed with a good accuracy. The non-interacting reference system is setup by Hamiltonian

$$H_s = -\frac{1}{2} \sum_i^N \nabla_i^2 + \sum_i^N V_s(\mathbf{r}_i), \quad (3)$$

which does not contain any electron-electron interactions. Accordingly, its ground state wave function is represented by a Slater determinant, where the spin-orbitals are determined from one-electron eigen-equations:

$$\hat{f}^{KS} \varphi_i = \varepsilon_i \varphi_i \quad (4)$$

with the one-electron *Kohn-Sham* operator

$$\hat{f}^{KS} = -\frac{1}{2} \nabla^2 + V_s(\mathbf{r}). \quad (5)$$

The one-electron spin-orbitals are usually called the *Kohn-Sham* orbitals. The connection of this artificial system to the real one established by choosing the effective potential  $V_s$  such that the density  $\rho_s$  resulting from the summation of the moduli of the squared orbitals  $\{\varphi_i\}$  exactly equals the ground state density  $\rho_0$  of the real target system of interacting electrons,

$$\rho_s(\mathbf{r}) = \sum_i^N \sum_s |\varphi_i(\mathbf{r}, s)|^2 = \rho_0(\mathbf{r}). \quad (6)$$

The exact kinetic energy of the non-interacting electrons is known, but it is different from the system with the interacting electrons. The difference is accounted in the following separation of the functional  $F[\rho]$ :

$$F[\rho] = T_s[\rho] + J[\rho] + E_{xc}[\rho], \quad (7)$$

where  $J$  is the classical Coulomb electron-electron interaction, and  $E_{xc}$  is the exchange-correlation functional, which includes the error of the kinetic energy together with the unknown electron-electron interactions:

$$E_{xc}[\rho] = (T[\rho] - T_s[\rho]) + (E_{ee}[\rho] - J[\rho]). \quad (8)$$

In order to determine the form of  $V_s$  so that it can provide the Slater determinant characterized by exactly the same density as the real interacting system, the expression for the energy functional of the interacting system has to be written in terms of the separation described in (7):

$$E[\rho(\mathbf{r})] = -\frac{1}{2} \sum_i^N \langle \varphi_i | \nabla^2 | \varphi_i \rangle + \frac{1}{2} \sum_i^N \sum_j^N \iint |\varphi_i(\mathbf{r}_1)|^2 \frac{1}{r_{12}} |\varphi_j(\mathbf{r}_2)|^2 d\mathbf{r}_1 d\mathbf{r}_2 + E_{xc}[\rho(\mathbf{r})] -$$

$$-\sum_i^N \int \sum_A^M \frac{Z_A}{R_{1A}} |\varphi_i(\mathbf{r}_1)|^2 d\mathbf{r}_1. \quad (9)$$

Varying the functional with respect to the *Kohn-Sham* orbitals  $\varphi_i(\mathbf{r})$  leads to the following single-electron equations:

$$\begin{aligned} & \left( -\frac{1}{2} \nabla^2 + \left[ \int \frac{\rho(\mathbf{r}_2)}{r_{12}} d\mathbf{r}_2 + V_{xc}(\mathbf{r}_1) - \sum_A^M \frac{Z_A}{r_{1A}} \right] \right) \varphi_i \equiv \\ & \equiv \left( -\frac{1}{2} \nabla^2 + V_{eff}(\mathbf{r}_1) \right) \varphi_i = \varepsilon_i \varphi_i \end{aligned}, \quad (10)$$

where

$$V_{xc} \equiv \frac{\delta E_{xc}}{\delta \rho}. \quad (11)$$

From the comparison of eq. (10) with eqs. (4) and (5), it can be seen that  $V_{eff} = V_S$ . It should be noted that  $V_{eff}$  already depends on the density (and thus on the orbitals) through the Coulombic term as shown in equation (9). Therefore, the Kohn-Sham one-electron equations (10) have to be solved iteratively. It is important to realize that if the exact forms of  $E_{xc}$  (or  $V_{xc}$ ) were known (which is unfortunately not the case), the Kohn-Sham DFT would lead to the exact ground state energy. Also important to notice is the fact that the *Kohn-Sham* eigenvalues are not the energies of the single-particle electron states, but rather the derivatives of the total energy with respect to the occupation numbers of these states<sup>44</sup>. However, if the exchange-correlation potential is exact, the highest occupied eigenvalue in atomic or molecular calculations is the unrelaxed ionization energy for that system<sup>45</sup>.

### 2.1.4 Local-density approximation (LDA)

The easiest approach to implement density functional approximation is the local density approximation, in which the functional is a simple integral over a function of the density at each point in space:

$$E_{xc}^{loc}[\rho] = \int \rho(\mathbf{r}) \varepsilon_{xc}(\rho(\mathbf{r})) d\mathbf{r}, \quad (12)$$

where  $\varepsilon_{xc}$  denotes the exchange-correlation energy per particle of the uniform electron gas of density  $\rho(\mathbf{r})$ . The local approximation is exact for the special case of a uniform electronic system, where the homogeneous electron gas is placed within a uniform positive external potential, chosen to preserve overall charge neutrality. The exchange-correlation energy can be factorized into two independent contributions: exchange and correlation. The approximate expression of the exchange energy is given by:

$$E_x[\rho] = C \int \rho^{4/3}(\mathbf{r}) d\mathbf{r} \quad (13)$$

with the constant  $C = -\frac{3}{4} \sqrt{\frac{3}{\pi}}$ .

In contrast to the exchange energy, the exact form of the correlation energy is not known. It should be noted, however, that highly accurate numerical quantum *Monte-Carlo* simulations of the homogeneous electron gas can be used towards this as shown by *Ceperly* and *Alder* in 1980<sup>46</sup>.

### 2.1.5 Generalized gradient approximation (GGA)

The local density approximation is derived from the assumption that electrons behave like an uniform electronic gas. This approximation gives highly accurate results for the metals, where the real electronic system has high degree of uniformity. However, in many other systems LDA is not sufficient to describe main features of the systems, especially if these features are very sensitive to non-homogeneity of the electronic density. An improvement of the exchange-correlation functional can be achieved by extending eq. (12) using the *gradient* of the charge density in order to account for the non-homogeneity of the true electron density. Thus, LDA can be interpreted as a first term of a Taylor expansion of the density, with the gradient of electron density as a first-order correction:

$$E_{xc}[\rho] = \int \rho \varepsilon_{xc}(\rho) d\mathbf{r} + \int C(\rho) \frac{\nabla \rho}{\rho^{2/3}} d\mathbf{r} . \quad (14)$$

It has been shown that this so called *gradient expansion approximation (GEA)* does not improve LDA but even degrades its accuracy in most cases. The reason for this failure is that the well-known exchange-correlation *hole* loses many of its fundamental properties, which makes the LDA *hole* physically meaningful <sup>47</sup>. The issue of the GEA can be solved in a straight-forward way, by *a priori* neglecting the terms that do not obey the fundamental properties of the exchange-correlation *hole*. Functionals that include the gradients of the charge density but with the *hole* constraints restored are collectively known as *generalized gradient approximations (GGA)*. Two groups of the GGA functionals exist so far:

1. The functionals designed to recover the exchange energy density asymptotically at distances far from the finite system. They utilize an empirical parameter, which makes them to be non *ab initio* strictly speaking. Functionals related to this approach include among others the FT97 functional of *Filatov and Thiel* <sup>48</sup>, the PW91 exchange functional <sup>49</sup>, and the CAM(A) and CAM(B) functionals developed by *Handy and coworkers* <sup>50</sup>.
2. The other group consists of the functionals that employ rational functions of the reduced density gradient. These functionals are parameter-free. Prominent representatives are the early functionals by *Becke* <sup>51</sup>, *Perdew* <sup>52</sup>, the functional by *Lacks and Gordon* <sup>53</sup>, and the implementation of *Perdew, Burke, and Ernzerhof (PBE)* <sup>54</sup>.

In this thesis a variety of the exchange-correlation functionals are employed. For DFT investigation of the intrinsic properties of molybdenum-chalcogenide nanowires, the *Perdew-Zunger* form <sup>55</sup> of LDA is used. In the research of the molybdenum-sulfide cluster deposition on *Au* (111) surface, both LDA and GGA are utilized. The LDA functional is parametrized with the *Teter-Pade* scheme <sup>56</sup>, which reproduces the Perdew-Wang exchange-correlation functional (in the final instance it is based on the Ceperly-Alder parametrisation). The binding energies are further refined with the PBE GGA exchange-correlation functional <sup>54</sup>. For density-functional based tight-binding (DFTB) calculations, including the electronic transport calculations based on DFTB method extended with Green's function formalism, the *Ceperly-Alder* LDA functional is used.

### 2.1.6 Pseudopotential

Despite the major advances in computer technology in last decades, the magnitude of the computational efforts necessary to calculate the physical properties of complex systems is still enormous, and therefore additional modifications to DFT are desirable. Since the atomic core-electron wavefunctions remain essentially unchanged when placed into different chemical environments, the true atomic potential can be replaced by pseudopotentials that effectively reproduce the core-electron interaction. Then, the core-electrons are not directly considered in the most computationally expensive self-consistent cycles of DFT, but rather indirectly via the pseudopotential. Two approaches were established to address the problem of the construction of physically reasonable pseudopotentials:

1. Core pseudopotentials of enforced smoothness were empirically fitted to reproduce experimental energies of the atom<sup>57, 58</sup>. The smoothness is of special interest when the plane-waves are chosen for the basis set. The wavefunctions close to core usually have highly oscillatory behaviour, which requires a large number of plane-waves in the basis set. Employing a smooth non-oscillating pseudopotential in that region significantly reduces the size of the basis set.
2. The orthogonalized-plane-wave (OPW) concept in connection with the pseudopotential method was used in order to derive *ab initio* pseudopotentials from atomic calculations without employing the empirical parameter<sup>59, 60</sup>. This approach is closer to main idea of DFT since it is a parameter-free method, but some problems still remain. For instance, the potentials are highly repulsive at distances close to the atomic center (hence they are often called *hard-core pseudopotentials*); the resulting wavefunction though exhibiting a correct form outside the core region, but can differ from the real wavefunction by a normalization factor.

In order to reproduce the results of all-electron calculations, the pseudopotentials have to obey the following properties:

1. Eigenvalues of the valence orbitals have to be equal both for the real and the pseudo-atom;
2. Eigenfunctions of the real and the pseudo-atom have to agree beyond a chosen core-radius  $r_c$ ;
3. The integrals from 0 to  $r$  of the real and pseudo-charge densities agree for  $r > r_c$ ;

4. The logarithmic derivatives  $\varphi'/\varphi$  of the real and pseudo wave-function with respect to energy have to agree for  $r > r_c$ .

Pseudopotentials meeting these four conditions are commonly referred to as *norm-conserving pseudopotentials*. According to Gauss' theorem, property 3 guarantees that the behavior of the electrostatic potential outside the core region is the same as in the real atom, whereas the properties that depend on the derivative of the wavefunctions of the real cores are reproduced by the point 4.

Throughout the work in the present thesis, the *Troullier-Martin* parametrization<sup>61</sup> of the pseudopotential was employed, both for DFT with plane-wave and local atomic-like basis set. The DFTB method that is also employed in this thesis introduces a somewhat different approach, which will be described in detail in the following.



## 2.2 Density-functional based tight-binding method

Until the '90-ties the performance of the computers could not serve ever increasing demand for high-accurate atomic calculations. Even the density functional theory could be employed only for relatively small systems of few tens of atoms; only very small molecules with less than 10-15 atoms were accessible for post-Hartree-Fock methods. One possible way for addressing larger systems was usage of empirical methods. However, fitted empirical parameters were usually not satisfactory transferable from one to another system. The density-functional based tight-binding (DFTB) method was suggested as a compromise between empirical and *ab initio* methods. It was originally developed in 1986 by Seifert and co-workers for efficient calculations of molecules<sup>62, 63</sup>. During last decade the DFTB method was systematically improved, including the self-consistent-charge extension (SCC-DFTB) as derived from the second-order expansion of the Kohn-Sham energy with respect to the atomic charge fluctuations<sup>64</sup>, spin-dependent formulation<sup>65</sup>, and time-dependent description of excited states<sup>66</sup>. The standard DFTB and SCC-DFTB have shown high accuracy in determination of geometries where the optimized bond-length between various systems deviates only by 3-5% from more computationally demanding DFT implementations<sup>67-80</sup>. The strong efficiency and satisfactory accuracy of DFTB motivated its implementation and application for investigation of variety of molecular properties. For example, molecular vibrations<sup>81, 82</sup>, nuclear magnetic resonance shifts<sup>67, 83</sup>, and linear-scaling formulation of the secular problem<sup>84</sup> can be described well in the DFTB framework. The DFTB method was also extended with (non)-equilibrium Green's function formalism for calculation of the electronic transport in molecules or solid-state systems<sup>85, 86</sup>.

Even today when the computer performance is by three orders of magnitude higher than in '80-ties, the *ab initio* and DFT methods are too much demanding for the needs of modern technology and biotechnology. This is particularly true for large biomolecules, adsorption studies of molecules on surfaces, molecular dynamics studies of nanosecond time scales, computer aided drug and nanomaterials design. The DFTB can be a method of

choice, with the speed that matches well the speed of standard semiempirical methods, but with accuracy approaching *ab initio* and DFT methods.

### 2.2.1 Kohn-Sham equations in DFTB

The total energy of a system comprised of  $M$  electrons in the field of  $N$  nuclei can be expressed, according to *Hohenberg-Kohn* theorem, as a functional of the charge density

$$E_{tot}[n(\mathbf{r})] = T[n(\mathbf{r})] + \iint d\mathbf{r} d\mathbf{r}' \frac{n_N(\mathbf{r}) n(\mathbf{r}')}{|\mathbf{r} - \mathbf{r}'|} + \frac{1}{2} \iint d\mathbf{r} d\mathbf{r}' \frac{n(\mathbf{r}) n(\mathbf{r}')}{|\mathbf{r} - \mathbf{r}'|} + \frac{1}{2} \iint d\mathbf{r} d\mathbf{r}' \frac{n_N(\mathbf{r}) n_N(\mathbf{r}')}{|\mathbf{r} - \mathbf{r}'|} + E_{xc}[n(\mathbf{r})], \quad (1)$$

where  $T(n)$  is the functional of the kinetic energy,  $n(\mathbf{r})$  and  $n_N(\mathbf{r})$  are the electronic and nuclear charge density distributions, respectively, and  $E_{xc}(n)$  is the functional of the exchange and correlation energy. The electron density distribution

$$n(\mathbf{r}) = \sum \psi_i^*(\mathbf{r}) \psi_i(\mathbf{r}) \quad (2)$$

can be calculated from the *Kohn-Sham* equations

$$\left[ -\frac{1}{2} \nabla^2 + V_{eff}(\mathbf{r}) \right] \psi_i(\mathbf{r}) = \epsilon_i \psi_i(\mathbf{r}), \quad (3)$$

where the effective potential is the sum of the *Hartree* and exchange-correlation potentials

$$V_H = \int d\mathbf{r}' \frac{n(\mathbf{r}') + n_N(\mathbf{r}')}{|\mathbf{r} - \mathbf{r}'|}, \quad (4a)$$

$$V_{xc} = \frac{\delta E_{xc}}{\delta n}. \quad (4b)$$

The total energy can be obtained from the energy functional (1) using the variational principle with respect to the electron density

$$E_{tot} = \min_n E(n) \approx E(\tilde{n}), \quad \tilde{n} \approx n. \quad (5)$$

In such way obtained electron density  $\tilde{n}$  corresponds to the approximate solution of the *Kohn-Sham* equations

$$\left[ -\frac{1}{2}\nabla^2 + V_s(\mathbf{r}) \right] \tilde{\psi}_i(\mathbf{r}) = \tilde{\epsilon}_i \tilde{\psi}_i(\mathbf{r}), \quad (6a)$$

$$\tilde{n}(\mathbf{r}) = \sum \tilde{\psi}_i^*(\mathbf{r}) \tilde{\psi}_i(\mathbf{r}) \quad (6b)$$

(see eq. (3) in **Section 2.1.3** for more details). After substitution of the approximate charge density distribution into the functional of the total energy (5), the latter one gets the following form

$$E_{tot}[\tilde{n}] = \frac{1}{2} \left\{ T(\tilde{n}) + \sum_i^{occ} \tilde{\epsilon}_i + \int d\mathbf{r} (\tilde{V}_H + \tilde{V}_{XC} - V_s(\mathbf{r})) \tilde{n} + \int d\mathbf{r} \tilde{V}_H n_N \right\} + \\ + E_{XC}[\tilde{n}] - \frac{1}{2} \int d\mathbf{r} \tilde{V}_{XC} \tilde{n} \quad (7)$$

The summing in (7) is obtained over occupied states only. The approximate effective potential is different from  $\tilde{V}_H + \tilde{V}_{XC}$ , hence the third term on the right side of the energy functional is not zero, as it would be in the case of the exact charge density distribution.

In the DFTB method the *Kohn-Sham* single-particle wavefunctions  $\psi_i(\mathbf{r})$  are represented as a linear combination of the valence atomic orbitals  $\varphi_\mu$ :

$$\psi_i(\mathbf{r}) = \sum_\mu C_\mu^i |\varphi_\mu\rangle. \quad (8)$$

The orthogonality of the atomic basis functions to the core atomic orbitals has to be fulfilled, which can be accomplished with Gram-Schmidt orthogonalization procedure, yielding the new basis:

$$|\varphi_\mu\rangle = |\varphi_\mu\rangle - \sum_{l \neq j} \sum_{c_l} |\varphi_{c_l}\rangle \langle \varphi_{c_l} | \varphi_\mu \rangle, \quad (9)$$

where the core orbitals at atom  $l$  are denoted by  $|\varphi_{c_l}\rangle$ .

The substitution of the linear combination of the orthogonal basis functions into the approximate *Kohn-Sham* equations (6) gives the new form for the single-particle energies

$$\tilde{\varepsilon}_i = \sum_{\mu} \sum_{\nu} C_{\mu}^i \left[ \left( \varphi_{\mu} \left| -\frac{1}{2} \nabla^2 + V_S \right| \varphi_{\nu} \right) - \sum_{c_l} \sum_{c_l'} \left( \varphi_{\nu} \left| \varphi_{c_l} \right) \varepsilon_{c_l} \left( \varphi_{c_l'} \left| \varphi_{\mu} \right) \right] C_{\nu}^i, \quad (10)$$

where  $\varepsilon_{c_l}$  are the energies of the core states at the center  $l$ . Thus a sum of the approximate potential  $V_S$  and the core correction term (see eq. (10)) can be interpreted as a pseudopotential ( $\mathbf{w}_{\mathbf{PP}}$ ) that yields a compact form of the *Kohn-Sham* energies:

$$\tilde{\varepsilon}_i = \sum_{\mu} \sum_{\nu} C_{\mu}^i \left[ \left( \varphi_{\mu} \left| -\frac{1}{2} \nabla^2 + \mathbf{w}_{\mathbf{PP}} \right| \varphi_{\nu} \right) \right] C_{\nu}^i. \quad (11)$$

To confirm the interpretation of  $\mathbf{w}_{\mathbf{PP}}$  as a pseudopotential, the approximate effective potential  $V_S$  can be written as a superposition of atom centered potentials

$$V_S = \sum_j (V_s)_j (\mathbf{r}_j). \quad (12)$$

With the substitution of (12) into eq. (11) the potential becomes a pseudopotential for all atoms in the system, except for the atoms where  $\varphi_{\mu}$  and  $\varphi_{\nu}$  are centered. Therefore, the pseudopotential appears only in the three-center and the crystal-field terms, whereas the “full” potential enters in all other terms. In the DFTB method all three-center and crystal-field terms are neglected, which leads to the following form of the orbital energies:

$$\tilde{\tilde{\varepsilon}}_i = \sum_{\mu} \sum_{\nu} C_{\mu}^i \left[ \left( \varphi_{\mu} \left| -\frac{1}{2} \nabla^2 + (V_s)_j + (1 - \delta_{jj'}) (V_s)_{j'} \right| \varphi_{\nu} \right) \right] C_{\nu}^i, \quad \mu \in \{j\}, \nu \in \{j'\}. \quad (13)$$

The sum of these orbital energies  $\tilde{\tilde{\varepsilon}}_i$  over all states  $i$  can be written in the form

$$\sum_i \tilde{\tilde{\varepsilon}}_i \equiv \tilde{T} + \int d\mathbf{r} \tilde{V}_s \tilde{n}. \quad (14)$$

It is worth to note that the expectation value of the kinetic energy  $\tilde{T}[\tilde{n}]$  in the orthogonal basis  $|\varphi_{\mu}\rangle$  differs from one in the former basis  $|\varphi_{\mu}\rangle$ . However, in the DFTB method this difference is neglected, i.e.  $T[\tilde{n}] \approx \tilde{T}[\tilde{n}]$ , as well as the difference between the effective

potential and the sum of the Hartree and exchange-correlation potentials, i.e.  $V_S \approx \tilde{V}_H + \tilde{V}_{XC}$ .

These approximations, after decomposing of  $\tilde{n}$ ,  $\tilde{V}_S$  and  $\tilde{V}_{XC}$  into superpositions of atomic contributions, result in the final DFTB form of the total energy functional:

$$E_{tot}[\tilde{n}] \approx \sum_i^{occ} \tilde{\epsilon}_i - \frac{1}{2} \sum_j \sum_l \int d\mathbf{r} \tilde{w}_j \tilde{n}_l - \frac{1}{2} \sum_j \sum_l \int d\mathbf{r} \frac{Z_j}{r_j} \tilde{n}_l + \\ + \frac{1}{2} \sum_j \sum_{l \neq j} \frac{Z_j Z_l}{R_{jl}} + \frac{1}{2} \sum_j \sum_l \left[ \int d\mathbf{r} \tilde{V}_{XC_j} \tilde{n}_l - 2 \int d\mathbf{r} \tilde{n}_j \tilde{n}_l \frac{\delta \epsilon_{XC}}{\delta n} \right]. \quad (15)$$

### 2.2.2 Repulsion potential

At the large interatomic distances the energy terms of the nuclear-nuclear repulsion and the electron-nuclear energy cancel each other

$$\int d\mathbf{r} \frac{Z_j}{r_j} \tilde{n}_l - \frac{Z_j Z_l}{R_{jl}} \approx 0, \quad (16)$$

The electronic potential around each atomic center is completely screened at large enough distance from the nuclei. Therefore, the two-center terms with the potential vanish

$$\sum_j \sum_l \int d\mathbf{r} (\tilde{V}_S)_j \tilde{n} = 0, \quad l \neq j. \quad (17)$$

At the large interatomic distances also the last two terms in eq. (15) with  $l \neq j$  can be neglected, which leaves in eq. (15) only the *Kohn-Sham* single-particle energies  $\sum \tilde{\epsilon}_i$  and the one-center terms. The remaining one-center terms cancel also in the relation for the binding energy

$$E_B = E_{tot} - \sum_j E_j \approx \sum_i \tilde{\epsilon}_i - \sum_j \sum_{n_j} \epsilon_{n_j} \quad (18)$$

where  $\mathcal{E}_{n_j}$  are the orbital energies of free atoms. In the DFTB method an additional gain of the calculation speed is achieved by substituting all above-mentioned canceling terms in eq. (15) with the simple pairwise repulsive energy

$$E_{rep} = \sum_{l \neq j} U(R_{lj}). \quad (19)$$

For large distances this energy vanishes, as dictated by eq. (18). The pair potentials  $U(R_{lj})$  can be obtained as the difference between the binding energy calculated at the given distances  $R_{lj}$  in eq. (15), and the corresponding electronic energy calculated within the DFTB approach for properly chosen reference systems. In the most simple case it is a dimer, but depending on the chemical elements under the consideration, the reference system may be more complex.

### 2.2.3 Matrix form of the *Kohn-Sham* equations

Use of the LCAO ansatz with the valence basis leads to the simple matrix form of the *Kohn-Sham* equations:

$$\sum_{\nu=1}^N C_{\nu i} (H_{\mu\nu} - \tilde{\mathcal{E}}_i S_{\mu\nu}) = 0. \quad (20)$$

The Hamiltonian and overlap matrix elements in eq. (20) are given by

$$H_{\mu\nu} = \begin{cases} \mathcal{E}_{\mu}^{\text{neutral free atom}}, & \text{if } \mu = \nu \\ \langle \varphi_{\mu} | \hat{T} + (V_S)_j^0 + (V_S)_k^0 | \varphi_{\nu} \rangle, & \text{for } \mu \in \{j\}, \nu \in \{k\} \\ 0, & \text{otherwise} \end{cases} \quad (21a)$$

$$S_{\mu\nu} = \langle \varphi_{\mu} | \varphi_{\nu} \rangle. \quad (21b)$$

In DFTB both the Hamiltonian and the overlap matrices are tabulated with respect to the interatomic distances  $R_{jk}$ . Therefore, the speed in DFTB calculations is gained by utilization

of the pre-computed integrals, which must be evaluated for the every iteration step in “full” DFT method.

The pseudo-atomic basis functions  $\varphi_\mu$  are self-consistently obtained by solving the *Kohn-Sham* equations for spherically symmetric spin-unpolarized neutral atoms

$$\left[ \hat{T} + (V_s)_j^0(r) + \left( \frac{r}{r_0} \right)^{n_0} \right] \varphi_\mu(r) = \varepsilon_\mu \varphi_\mu(r). \quad (22)$$

The additional term  $(r/r_0)^{n_0}$  introduced by *Eschrig*<sup>87, 88</sup> for the contraction of the atomic orbitals improves the description of the atomic orbitals in molecules and solid state, because they are more diffusive in free atoms than in the mentioned systems<sup>87</sup>. A variational principle can be applied for the determination of the contraction radii  $r_0$ <sup>87, 89</sup>. From the broad experience accumulated for various elements, it has been found that the best choice for the contraction radii is  $r_0 = 1.85 r_{\text{cov}}$ , where  $r_{\text{cov}}$  is the covalent radius of the atom. The usual choice of the exponent  $n_0$  is either 2 or 4. In eq. (22) the atomic orbitals are represented by the linear combinations of Slater-type orbitals

$$\varphi_\mu(\mathbf{r}) = \sum_{\zeta} \sum_i a_{\zeta i} r^{l+i} e^{-\zeta r} Y_{lm} \left( \frac{\mathbf{r}}{r} \right), \quad (23)$$

where  $l$  and  $m$  are the angular momentum and the magnetic quantum numbers associated with the orbital  $\mu$ , respectively. Extensive tests have shown that only five different values for  $\zeta$  and four values for  $i$  form a sufficiently accurate basis set<sup>87</sup>.

## 2.2.4 Interatomic forces

Interatomic forces for structural optimizations and molecular-dynamics applications are obtained from the derivation of the total energy with respect to nuclear coordinates, at the considered atomic sites. By considering the secular equations (20) the forces on atom  $\alpha$  in the component  $u = (x, y, z)$  can be written as:

$$-\frac{\partial E_{tot}}{\partial (\mathbf{R}_\alpha)_u} = -\sum_i n_i \sum_{\mu, \nu} C_{\mu i} C_{\nu i} \left[ \frac{\partial H_{\mu \nu}}{\partial (\mathbf{R}_\alpha)_u} - \epsilon_i \frac{\partial S_{\mu \nu}}{\partial (\mathbf{R}_\alpha)_u} \right] - \sum_{\beta \neq \alpha} \frac{\partial E_{rep}(|\mathbf{R}_\alpha - \mathbf{R}_\beta|)}{\partial (\mathbf{R}_\alpha)_u}. \quad (24)$$

### 2.2.5 Second-order self-consistent charge extension (SCC-DFTB)

The utilization of the standard DFTB method is efficient when the electron density of a molecule or a solid-state system may be represented as a sum of atomic-like densities. The accuracy of the DFTB approximations become less valid if the chemical bonding is determined by a delicate charge balance, especially in heteronuclear molecules and in polar semiconductors. Therefore, for such systems further corrections to the standard DFTB method have to be addressed. Towards this end the total energy functional is expanded in the Taylor series up to second order in the density fluctuations  $\delta n \equiv \delta n(\mathbf{r}) = n - n_0$  around the reference density  $n_0$ :

$$E = \sum_i^{occ} \langle \varphi_i | \hat{H}_0 | \varphi_i \rangle - \frac{1}{2} \iint \frac{n_0' n_0}{|\mathbf{r} - \mathbf{r}'|} \delta n \delta n' + E_{xc}[n_0] - \int V_{xc}[n_0] n_0 \delta n + E_N + \frac{1}{2} \iint \left( \frac{1}{|\mathbf{r} - \mathbf{r}'|} + \frac{\delta^2 E_{xc}}{\delta n \delta n'} \bigg|_{n_0} \right) \delta n \delta n' + \dots \quad (25)$$

After decomposition of the electronic charge distribution into atom-centered contributions  $\delta n = \sum_\alpha \delta n_\alpha$ , the second-order correction in (25) becomes

$$E^2[n, n_0] \equiv \frac{1}{2} \sum_{\alpha, \beta} \iint \left[ \frac{1}{|\mathbf{r} - \mathbf{r}'|} + \frac{\delta^2 E_{xc}[n]}{\delta n \delta n'} \right] \delta n_\alpha(\mathbf{r}) \delta n_\beta(\mathbf{r}'). \quad (26)$$

The atom-centered fluctuations of the charge density can be further expanded into a sum of multipole contributions

$$\delta n_\alpha(\mathbf{r}) = \sum_{l, m} K_{ml} F_{ml}^a(|\mathbf{r} - \mathbf{R}_\alpha|) Y_{lm} \left( \frac{\mathbf{r} - \mathbf{R}_\alpha}{|\mathbf{r} - \mathbf{R}_\alpha|} \right) \approx \Delta q_\alpha F_{00}^\alpha(|\mathbf{r} - \mathbf{R}_\alpha|) Y_{00}, \quad (27)$$



where  $F_{ml}^\alpha$  is the radial part of the density fluctuation on atom  $\alpha$ . In the SCC-DFTB method only the monopole term is retained, while all other terms are omitted. The higher-order interactions decay much more rapidly with increasing the interatomic distance. After substitution of eq. (27) into eq. (26), the second-order correction gets the following form:

$$E^2[n, n_0] = \frac{1}{2} \sum_{\alpha, \beta} \Delta q_\alpha \Delta q_\beta \gamma_{\alpha\beta} \quad (28)$$

with

$$\gamma_{\alpha\beta} = \iint \Gamma[\mathbf{r}, \mathbf{r}', n_0] \frac{F_{00}^\alpha(|\mathbf{r} - \mathbf{R}_\alpha|) F_{00}^\beta(|\mathbf{r}' - \mathbf{R}_\beta|)}{4\pi}, \quad (29)$$

where  $\Gamma[\mathbf{r}, \mathbf{r}', n_0]$  is an abbreviation for the Hartree and exchange-correlation terms. In the asymptotic case of large interatomic distances, the exchange-correlation is negligible within LDA and  $E^2[n, n_0]$  takes the form of a pure Coulombic interaction between two point charges  $\Delta q_\alpha$  and  $\Delta q_\beta$ . In the opposite case of the charges originating only from one atom, the calculation of  $\gamma_{\alpha\alpha}$  requires a proper choice for  $E_{xc}$ , which is not well determined within LDA. The quantity  $\gamma_{\alpha\alpha}$  is then approximated by the difference between the atomic ionisation potential and the electron affinity<sup>90</sup>. On the other hand, the difference is approximately equal to double value of the chemical hardness  $\eta_\alpha$ <sup>91</sup> (or the Hubbard parameter  $U_\alpha$ ) via the relations  $\gamma_{\alpha\alpha} \approx I_\alpha - A_\alpha \approx 2\eta_\alpha \approx U_\alpha$ . Within the monopole approximation and DFT framework, the Hubbard parameter is the second derivative of the total energy  $E^{at}$  of free atom  $\alpha$  with respect to the atomic charge

$$E^2[n, n_0] \approx \frac{1}{2} \frac{\partial^2 E^{at}[n_\alpha^0]}{\partial q_\alpha^2}. \quad (30)$$

According to Janak's theorem<sup>44</sup>, the latter second derivative corresponds to the derivative of the energy of the highest occupied atomic orbital with respect to its occupation number

$$\frac{1}{2} \frac{\partial^2 E^{\text{at}}[n_{\alpha}^0]}{\partial q_{\alpha}^2} \rightarrow \frac{\partial \epsilon_{\text{homo}}}{\partial n_{\text{homo}}}. \quad (31)$$

Therefore, the second-order correction of the total energy can be also obtained from the first principles.

In conclusion, the DFTB method is an approximate DFT method, which retains all essential features of DFT, providing 2-3 orders of magnitude higher computational speed for the same molecular or solid state structures. Opposite to semiempirical quantum chemical methods, the DFTB scheme is free from empirical parameters. The Hamiltonian and overlap matrices are calculated within DFT, and the repulsion potential is obtained from the reference structures as the difference between the DFT and the DFTB binding energies.

## 2.3 Parameters for DFTB calculations

### 2.3.1 Basic DFTB parameters

The basics of the DFTB method are derived in **Chapter 2.2**. It is shown that DFTB approximations lead to major speed-up with respect to the “full” DFT method, although pertaining the relatively good accuracy of the latter one. The speed-up of DFTB calculations in many respects relies on the use of pre-calculated Hamiltonian and overlap matrices. As it has been discussed above, a proper choice of the contraction radius  $r_0$  and exponent  $n_0$  (in eq. (22) of **Chapter 2.2.3**) is important. As already mentioned, a good choices for the values of  $n_0$  are usually 2 or 4, whereas the best choice for the contraction radii is  $r_0 = 1.85 r_{\text{cov}}$ , where  $r_{\text{cov}}$  is the covalent radius of the atom in question. The latter relation is the result of broad experience accumulated in the field of DFTB<sup>87, 89</sup>. The contraction radii of molybdenum, sulfur and iodine atoms utilized in the thesis are obtained from this formula. The corresponding values for gold are chosen such that the DFTB electronic band structure of the gold surface would correspond to the DFT results as close as possible (see below for more details). A dependence of the radii  $r_0$  on the orbital angular momentum quantum number of the free atom can be also taken into account in eq. (22) of **Chapter 2.2.3**. The *Ceperly-Alder* parametrization<sup>46</sup> is utilized for the calculations of Hamiltonian and overlap matrices for all elements considered in the thesis. The DFTB method utilizes only the valence basis for representing different chemical elements. In order to speed up the calculations even more, *d*-orbitals were excluded from the basis functions of sulfur and iodine. Test calculations performed for the molybdenum chalcogenide nanowires with *d*-functions included showed no essential improvements, which support our choice of the smaller basis sets for *S* and *I* atoms. The basis set for each chemical element considered in this thesis, as well as the values of exponents  $n_0$  and contraction radii  $r_0$  are tabulated in **Table 1**. The quality of these parameters will be evaluated by comparing the DFTB results for the electronic properties of  $\text{Mo}_6\text{S}_{6-x}\text{I}_x$  nanowires with corresponding results obtained with DFT (detailed analysis is given in **Chapter 4** after presentation of data about  $\text{Mo}_6\text{S}_{6-x}\text{I}_x$  nanowires in **Chapter 3**).

**Table 1:** DFTB parameters for *Mo*, *S*, *I*, and *Au*.  $n_0$  and  $r_0$  in second and third column correspond to the exponent and the contraction radius in eq. (22) of **Chapter 2.2.3**. The contraction radii are tabulated for *s*-, *p*-, and *d*- orbitals. In right-most column are given atomic orbitals that form the valence basis for each element.

	$n_0$	$r_0$ (s) c	$r_0$ (p) [Bohr]	$r_0$ (d) [Bohr]	orbitals
<i>Mo</i>	4	4.9	4.9	4.9	5s,5p,4d
<i>S</i>	4	3.9	3.9	N/A	3s,3p
<i>I</i>	4	4.6	4.6	N/A	5s,5p
<i>Au</i>	2	4.0	6.0	5.0	6s,6p,5d

### 2.3.2 Repulsion potential

The repulsion potential is defined in **Chapter 2.2.2**. As it has been already discussed in detail, a purpose of this potential is to compensate terms neglected in the DFTB method. New repulsion potentials were obtained for each pair of chemical elements investigated in the thesis excluding gold (*Mo-Mo*, *S-S*, *I-I*, *Mo-S*, *Mo-I*, and *S-I*). They were calculated using the binding energies of dimers for most combinations of elements, whereas a special care was given to the *Mo-Mo* pair whose repulsion potential was evaluated from the *Mo-Mo* interaction in the *Mo<sub>4</sub>* cluster (tetrahedron). The calculated data were fitted to the polynomial.

$$U_{\text{rep}} = \sum_{i=2}^8 C_i (r - r_0)^i$$

The coefficients of the fitted polynomials are listed in **Table 2**.

**Table 2:** Coefficients of the polynomial fit for different repulsion potentials.

	$C_2$	$C_3$	$C_4$	$C_5$	$C_6$	$C_7$	$C_8$
<i>Mo-Mo</i>	0.108	-0.079	0.047	0.000	0.000	0.000	0.000
<i>Mo-S</i>	0.361	-0.194	2.132	-1.913	0.944	-0.237	0.024
<i>Mo-I</i>	0.094	-0.221	0.376	-0.318	0.153	-0.038	0.004
<i>S-I</i>	0.054	-0.106	0.103	-0.054	0.016	-0.003	0.001

### 2.3.3 Stability of gold surface

It can be noticed that the repulsion potential between gold and other elements are not represented in **Table 2**. A reason for this is the problem with the stability of the gold surface (or rather thin gold films), which will be explained in this section. It turned out that layers in gold films were mutually strongly repulsive within DFTB calculations even when the repulsion potential was zero. The final optimized geometry appeared to correspond to a set of isolated gold monolayers separated by more than 3.5 Å. On other hand, the geometry optimization performed using DFT with the plane-wave basis<sup>5</sup> gave a stable structure, with *Au-Au* bondlengths of around 2.88 Å. In order to get an insight why the DFTB result differs considerably from the DFT result, the electronic band structures of gold *fcc* crystal calculated with DFT<sup>6</sup> and DFTB methods are compared in **Figure 1**. It seems that electronic bands at energy region from -10 up to about 8 eV around Fermi level calculated with DFTB method correspond very well to the electronic bands obtained with the DFT method. Hence, the electronic structure of the *fcc* gold crystal is explained very well within DFTB method. Only the electronic states positioned below the Fermi level and in the narrow region above it are important for all electronic properties studied in the thesis. Besides, the states above the Fermi level are not well established within DFT (and also DFTB) anyway, since it is a ground-state theory as based on the *Hohenberg-Kohn* theorems (see **Chapter 2**).

Next, the electronic band structures of the gold film consisting of 15 layers calculated with the DFTB and DFT methods are compared in **Figure 2**. The DFT calculations were performed using the mixed basis set consisting of plane waves and a set of localized functions centered at the atomic sites<sup>92</sup>. For easier comparison the DFTB band structure is overlayed over that one obtained with the DTF method. A very good agreement between the two

---

<sup>5</sup> As implemented in the ABINIT code.

<sup>6</sup> As implemented in the FPLO code. Since both FPLO and DFTB utilize the atomic-like basis rather than the plane-wave basis from ABINIT implementation of DFT, a direct comparison between FPLO and DFTB electronic structures is more appropriate.

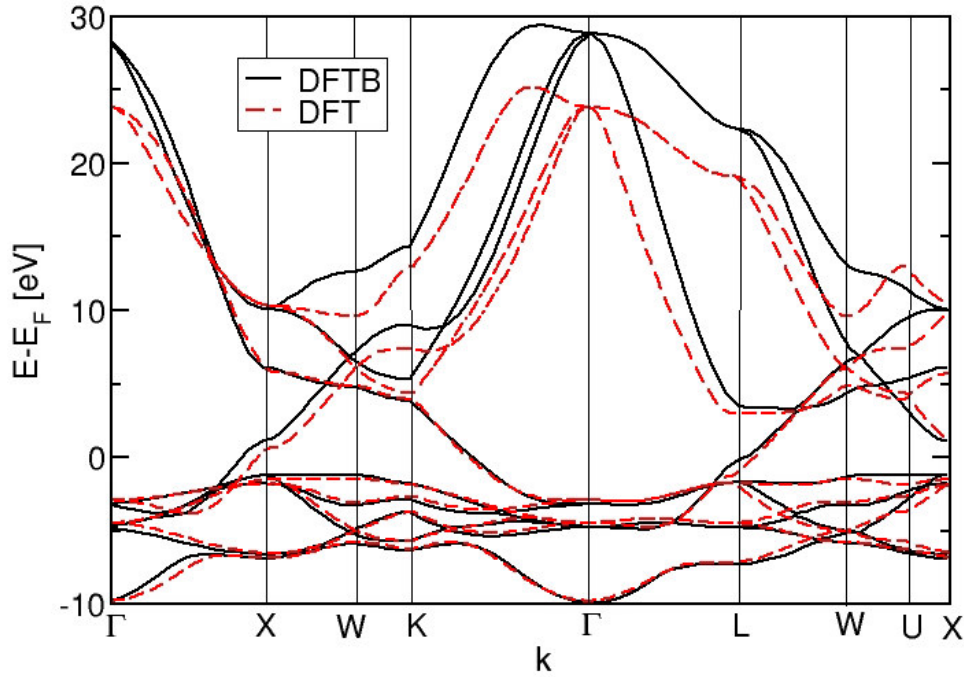


**Figure 1:** Electronic band structure of bulk gold (*Au fcc* crystal) obtained with DFTB (full black lines) and DFT (dashed red lines).

band structures demonstrate a good quality of DFTB for evaluation of the electronic properties of gold. Therefore, the electronic properties of gold are explained relatively accurately within DFTB method. However, the problem of the instability of gold films in DFTB calculations remains.

A gold surface appears to be stable in “full” DFT calculations when a large enough plane-wave basis is utilized (see **Chapter 6**). DFTB is, as the method derived from DFT introducing some approximations and using minimal basis set (see **Chapter 2.2**), somewhat more pronounced to the gold surface instability. Since some systems considered in the thesis include the gold surface as an electrode (see **Chapter 7**), the optimization of the part of its structure that contains the gold surface is done with “full” DFT (**Chapter 6**). These optimized geometries are then kept fixed and utilized in the DFTB calculations of transport and electronic properties of the system.

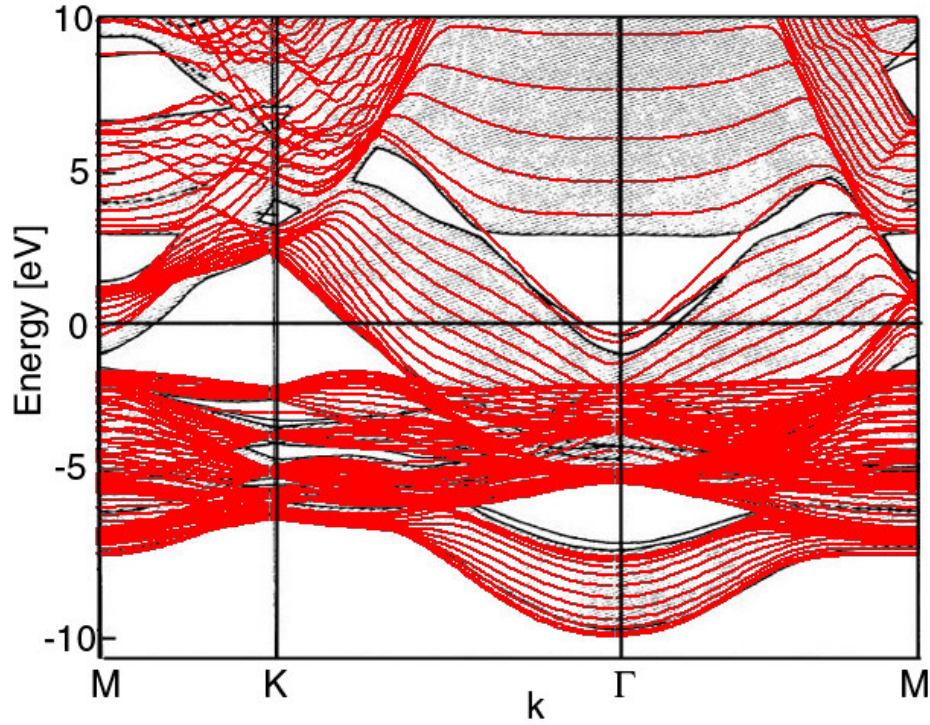


**Figure 2:** Electronic band structure of a gold film consisting of 15 layers, obtained with DFT (gray shadow) and DFTB method (red lines). Fermi level is at zero. DFT data is taken from ref. <sup>92</sup>.

Although not directly related with gold films, it could be worth to notice that also some experimental results indicate the instability of gold nanoparticles: It has been observed that gold nanoparticles considerably shrink during time of 2-3 weeks after they are synthesized <sup>93</sup>, <sup>94</sup>. It is possible that nanoparticles “lose” the gold atoms layer by layer, until a stable cluster with certain size remains.

## 2.4 Formalism of Green's functions

*The Green's functions were extensively used in the research of the electronic transport in the present thesis. Therefore, it is desirable to present the most important aspects of this formalism, which will be accomplished in this chapter. First, the advanced and retarded Green's functions will be defined in **Section 2.4.1**, and their relation will be derived in **Section 2.4.2**. The introduction of the self-energy as an additional term to the Hamiltonian of the system will follow, which is an important operator that accounts the semi-infinite electrodes and the interaction between electrodes and the central scattering region of the system. In contrast to the original Hamiltonian of the system, the self-energy is not a Hermitian operator. This fact has some important physical consequences, which will be discussed in **Section 2.4.3**. The spectral function will be defined in **Section 2.4.4**, along with its important relation to the Green's function, which will be used for the derivation of the final formula for the transmission function  $T(E)$  in **Section 2.4.6**. The spectral function represents the available density of states that can be populated by bound or propagating electrons through the open system. Its relation to the electron density will be derived in **Section 2.4.5**. The broadening function, defined in **Section 2.4.4**, determines the lifetime of the propagating electrons, which is for the open systems connected to the rate at which the electrons escape to/from electrodes from/to the central scattering region. Therefore, using the broadening function the current outflow into the electrodes can be found as a quantum average of the escape rate. This fact will be used for the derivation of the electronic current in **Section 2.4.6**, which comparison to the Buttiker formula for the current will lead to the final expression for the transmission function that was employed in the calculations of the transport properties in this thesis. Non-equilibrium Green's function formalism is employed only briefly in this thesis, hence it will not be discussed in detail.*

### 2.4.1 Retarded and advanced Green's functions

Green's functions formalism<sup>17</sup> is an elegant way to describe the response  $R$  of the system excitation  $S$ , connected with the differential operator  $\hat{D}$ :

$$\hat{D} R = S . \quad (1)$$



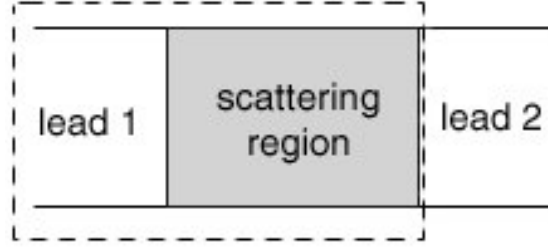


**Figure 3:** Schematic representation of an open system with two leads. With dashed line is marked a subsystem with only one lead that is considered in the text.

The Green's function  $\hat{G}$  is defined as an inverse of the operator  $\hat{D}$

$$R = \hat{D}^{-1}S \equiv \hat{G}S. \quad (2)$$

In the following an open system will be considered (see **Figure 3**), which consists of one finite part (termed as *scattering region*) connected with one or more semi-infinite parts (termed as *leads* or *electrodes*). The Schrödinger equation has to be written in a modified form for the open system:

$$(E - \hat{H})\psi = S, \quad (3)$$

where  $S$  denotes an excitation term due to a electronic “wave” incident from one of the leads. According to eq. (2), the Green's function for the open system can be obtained from:

$$\hat{G} = (E\hat{I} - \hat{H})^{-1}. \quad (4)$$

The physical meaning of the Green's function is more obvious when it is represented in terms of eigenvectors of the radius-vector operator  $\hat{\mathbf{r}}$ . Then, for two eigenvectors  $\mathbf{r}$  and  $\mathbf{r}'$ , the Green's function  $G(\mathbf{r}, \mathbf{r}')$  represents the response of the system at  $\mathbf{r}'$  when the excitation is originated at  $\mathbf{r}$ . From its definition as an inverse of a differential operator, the Green's function is not uniquely defined without proper boundary conditions. The so-called *retarded* Green's function corresponds to waves originated at the point of the excitation  $\mathbf{r}$  and spreading away from it. On the other hand, the *advanced* Green's function represents a wave incoming into the point of the excitation. In order to eliminate this double-fold nature of the Green's function, an infinitesimal imaginary part  $i\eta$ ,  $\eta > 0$  can be added to the Hamiltonian, which causes that the advanced Green's function becomes infinite far enough from the point of the

excitation. This feature eliminates the advanced Green's function as a non-physical solution. In the following text, the retarded and advanced Green's functions will be denoted as  $G^R$  and  $G^A$ , respectively.

#### 2.4.2 Relation between $G^R$ and $G^A$

In order to derive the relation between the retarded and advanced Green's functions, first they have to be expanded in the basis of eigenfunctions  $\psi_\alpha(\mathbf{r})$  of the Hamiltonian operator  $\hat{H}$  ( $\hat{H}\psi_\alpha(\mathbf{r}) = \varepsilon_\alpha\psi_\alpha(\mathbf{r})$ ):

$$G^R(\mathbf{r}, \mathbf{r}') = \sum_{\alpha} C_{\alpha}(\mathbf{r}') \psi_{\alpha}(\mathbf{r}), \quad (5)$$

where the non-local nature of the retarded Green's function is pronounced in terms of coefficients  $C_{\alpha}(\mathbf{r}')$  and eigenfunctions  $\psi_{\alpha}(\mathbf{r})$ , which are given at two different positions  $\mathbf{r}$  and  $\mathbf{r}'$ . The eigenfunctions form a complete orthogonal set:

$$\int \psi_{\alpha}^*(\mathbf{r}) \psi_{\beta}(\mathbf{r}) = \delta_{\alpha\beta}. \quad (6)$$

Assuming the excitation  $S$  as a Dirac delta function, and substituting eq. (6) into (3) (with the additional infinitesimal imaginary part included in order to eliminate non-physical solution of the Green's function), eq. (3) obtains the following representation

$$\sum_{\alpha} (E - \varepsilon_{\alpha} + i\eta) C_{\alpha} \psi_{\alpha} = \delta(\mathbf{r} - \mathbf{r}'). \quad (7)$$

The expansion coefficients can be obtained after multiplying eq. (7) by  $\psi_{\beta}^*(\mathbf{r})$ , integrating over  $\mathbf{r}$ , and taking into account the orthogonality condition (6):

$$C_{\alpha} = \frac{\psi_{\alpha}^*(\mathbf{r}')}{E - \varepsilon_{\alpha} + i\eta}. \quad (8)$$

This gives the final form for the expansion of the retarded Green's function in the basis  $\psi_\alpha(\mathbf{r})$

$$G^R(\mathbf{r}, \mathbf{r}') = \sum_\alpha \frac{\psi_\alpha(\mathbf{r})\psi_\alpha^*(\mathbf{r}')}{E - \varepsilon_\alpha + i\eta}. \quad (9)$$

Following the same procedure, the advanced Green's function gains the form

$$G^A(\mathbf{r}, \mathbf{r}') = \sum_\alpha \frac{\psi_\alpha(\mathbf{r})\psi_\alpha^*(\mathbf{r}')}{E - \varepsilon_\alpha - i\eta}, \quad (10)$$

which implies the following relation between the retarded and advanced Green's functions

$$G^A = [G^R]^\dagger. \quad (11)$$

### 2.4.3 Self-energy

Technically, it is not possible to obtain the Green's function directly from eq. (4) by matrix inversion, since the matrix  $(E\hat{I} - \hat{H})$  (or, more accurately  $[(E + i\eta)\hat{I} - \hat{H}]$ ) is infinite-dimensional due to the semi-infinite dimensions of the electrodes. A simple truncation of the matrix at some finite dimension would result in a wrongly defined closed system with ideally reflective boundaries, which would be essentially different from the original infinite system. However, the problem of the open boundaries can be elegantly solved as follows. First, the overall electronic device under the investigation can be partitioned into a scattering region and one or more electrodes. If only one electrode is present in the system, the Green's function can be partitioned into sub-operators

$$\begin{bmatrix} G_p & G_{ps} \\ G_{sp} & G_s \end{bmatrix} = \begin{bmatrix} (E + i\eta)\hat{I} - H_p & (E + i\eta)\hat{I} - \hat{V}_{s\alpha}^+ \\ (E + i\eta)\hat{I} - \hat{V}_{sp} & E\hat{I} - H_s \end{bmatrix}^{-1}, \quad (12)$$

where the operator  $(E + i\eta)\hat{I} - H_p$  describes the isolated electrode, while  $E\hat{I} - H_s$  represents the isolated scattering region. The  $G_{sp}$  and  $G_{ps}$  elements correspond to the

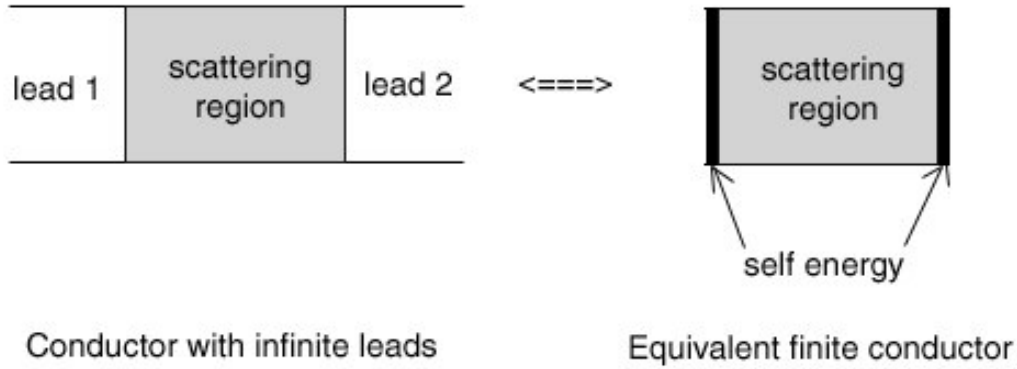


**Figure 4:** Reducing the infinite open-system to finite system upon the introduction of the self-energy.

coupling between the electrode and the scattering region. These terms correspond to  $(E + i\eta)\hat{I} - \hat{V}_{sp}$  and  $(E + i\eta)\hat{I} - \hat{V}_{sa}^+$  elements of the matrix  $((E + i\eta)\hat{I} - \hat{H})$ , where  $\hat{V}_{sp}$  represents the part of the Hamiltonian  $\hat{H}$  responsible for the coupling between the leads and the scattering region. The expression for the Green's function of the scattering region can be derived from eq. (12)

$$G_s = [E\hat{I} - \hat{H}_s - \Sigma_p^R]^{-1}, \quad (13)$$

where

$$\Sigma_p^R = [(E + i\eta)\hat{I} - \hat{V}_{sa}] \hat{g}_p^R \tau_p [(E + i\eta)\hat{I} - \hat{V}_{sa}^+] \quad (14)$$

is the so-called *self-energy*, and

$$\hat{g}_p^R = [(E + i\eta)\hat{I} - \hat{H}_p]^{-1} \quad (15)$$

is the Green's function of the isolated semi-infinite electrode, often referred to as the *surface Green's function*. The problem of the inversion of an infinite matrix is still present, however it is transformed into the inversion of the  $(E + i\eta)\hat{I} - \hat{H}_p$  matrix, which corresponds exclusively to a semi-infinite electrode. A variety of methods for the calculation of the surface Green's function are developed. For instance, the *decimation technique* that is a recursive algorithm based on the renormalization theory<sup>95-97</sup>. This technique has been

employed in the calculations of thesis. It should be also noticed that an exact approach exists based on a conformal mapping<sup>98</sup>. Therefore, assuming that self-energy is known, the problem of the infinite open-system is deduced to a finite one schematically shown in **Figure 4**. For the system with more than one electrode, eq. (13) is simply summed over index  $p$

$$G_s = [E \hat{I} - \hat{H}_s - \Sigma^R]^{-1}, \quad (16)$$

where  $\Sigma^R = \sum_p \Sigma_p^R$ . The infinite open system is therefore reduced to the finite one in the scattering region only. The Green's function in eq. (16) is obtained by inversion of the finite matrix, which is technically possible. The infinite contacts and their interaction with the rest of the system are mapped into complex self-energies, which can be understood as an additional potential to the scattering part of the Hamiltonian.

The expansion (10) of the overall Green's function with eigenfunctions of the modified Hamiltonian with the self-energy is not valid, since the eigenfunctions of the original Hamiltonian do not form a complete basis for the modified Hamiltonian  $[\hat{H}_s + \Sigma^R]$ . The expansion of the Green's function is achievable in the *dual basis*, which consists of the eigenfunctions of the operators  $[\hat{H}_s + \Sigma^R]$  and  $[\hat{H}_s + \Sigma^A]$ , where

$$\Sigma^A = [\Sigma^R]^\dagger. \quad (17)$$

The vectors in the dual basis are orthogonal, i.e.:

$$\int \phi_\alpha(\mathbf{r}) \psi_\beta^*(\mathbf{r}) d\mathbf{r} = \delta_{\alpha\beta} \quad (18)$$

where

$$[\hat{H}_s + \Sigma^R] \psi_\alpha = \epsilon_\alpha \psi_\alpha \quad (19)$$

and

$$[\hat{H}_s + \Sigma^A] \phi_\alpha = \epsilon_\alpha \phi_\alpha. \quad (20)$$

The representation of the Green's function in the dual basis obeys the form

$$G^R(\mathbf{r}, \mathbf{r}') = \sum_{\alpha} \frac{\psi_{\alpha}(\mathbf{r}) \phi_{\alpha}^*(\mathbf{r}')}{E - \varepsilon_{\alpha}}. \quad (21)$$

It is important to notice that the self-energy, in general, is not a Hermitian operator, hence the energies  $\varepsilon_{\alpha}$  in eigenequations (18) and (19) are complex numbers. This property yields a fundamental consequence on the time-dependence of the eigenstates of the modified Hamiltonian  $H_S + \Sigma^R$ . The eigenenergies  $\varepsilon_{\alpha}$  can be written in the canonical form

$$\varepsilon_{\alpha} = \varepsilon_{\alpha 0} - \Delta_{\alpha} - i \frac{\gamma_{\alpha}}{2}. \quad (22)$$

Upon the coupling to the electrodes, the eigenenergies  $\varepsilon_{\alpha 0}$  of the isolated scattering region (eigenvalues of the Hamiltonian  $H_S$ ) are shifted by  $\Delta_{\alpha}$ . The time-dependent eigenfunction of the full system is proportional to

$$\exp[-i\varepsilon_{\alpha}t/\hbar] \equiv \exp[-i(\varepsilon_{\alpha 0} - \Delta_{\alpha})t/\hbar] \exp[-\gamma_{\alpha}t/\hbar]. \quad (23)$$

The probability of finding an electron in a state  $\alpha$  is square of the corresponding wavefunction corresponding, i.e. it is proportional to  $\exp[-2\gamma_{\alpha}t/\hbar]$  which gives the physical nature of the quantity  $\hbar/2\gamma_{\alpha}$ . This introduces the  $\hbar/2\gamma_{\alpha}$  as a “lifetime”, or an average time for an electron remaining in the state  $\alpha$  before it “decays” into one of the electrodes. The usual physics of the closed systems is recovered when the Hamiltonian is purely Hermitian, which assures the existence of only real eigenvalues, hence the  $\gamma_{\alpha} = 0$  and consequently the “lifetime” of the electron  $\hbar/2\gamma_{\alpha}$  becomes unlimited.

#### 2.4.4 Spectral function

Another consequence of the non-hermitian nature of the modified Hamiltonian is the form of the spectral function defined with

$$A = i[G^R - G^A]. \quad (24)$$

In the representation of the dual basis (eqs. (18) and (19)), the spectral function obtains the following form

$$A(\mathbf{r}, \mathbf{r}') = \sum_{\alpha} \psi_{\alpha}(\mathbf{r}) \phi_{\alpha}^*(\mathbf{r}') \frac{\gamma_{\alpha}}{(E - \varepsilon_{\alpha 0} + \Delta_{\alpha})^2 + (\gamma_{\alpha}/2)^2} \quad (25)$$

It is important to notice that  $A(\mathbf{r}, \mathbf{r}')$  is not a simple superposition of the Lorentzian-like functions  $\frac{\gamma_{\alpha}}{(E - \varepsilon_{\alpha 0} + \Delta_{\alpha})^2 + (\gamma_{\alpha}/2)^2}$  of the energy  $E$ . The eigenfunctions  $\psi_{\alpha}(\mathbf{r})$  and  $\phi_{\alpha}(\mathbf{r})$  are functions of energy as well, which may give a large deviation of the Lorentzian-like forms in case of large coupling of the scattering region with the electrodes. On the other hand, the Lorentzian-like peaks in the spectral function indicate only a weak coupling between the electrodes and the scattering region. This is obtained in the present thesis for the system consisting of a molybdenum sulfide nanowire coupled between two gold electrodes.

Before proceeding, an important relation between the spectral function and the Green's function has to be derived, which will be used in derivation of the final expression of current through the system that is a main goal of this chapter. From eq. (16) it follows that

$$[G^R]^{-1} - [G^A]^{-1} = \Sigma^A - \Sigma^R = i\Gamma, \quad (26)$$

where a new quantity, so called *broadening function* is introduced:

$$\Gamma = i[\Sigma^R - \Sigma^A]. \quad (27)$$

After multiplying eq. (26) by  $G^R$  from the left and by  $G^A$  from the right side, the desired relationship is obtained:

$$A = G^R \Gamma G^A. \quad (28)$$

#### 2.4.5 Density of states in open systems

The density matrix corresponding to eigenstate  $\varepsilon_k$  is, by definition, a matrix function

$$\hat{\rho}_k = f_0(\hat{H} + (\varepsilon_k - \mu)\hat{I}), \quad (29)$$

where  $f_0$  is the Fermi function. Using the property of the delta-function

$$f(x_0) = \int_{-\infty}^{\infty} f(x) \delta(x - x_0) dx \quad (30)$$

the eq. (29) can be rewritten in the form

$$\hat{\rho}_k = \int_{-\infty}^{\infty} f_0(E + \varepsilon_k - \mu) \delta(E\hat{I} - \hat{H}) dE. \quad (31)$$

Utilizing the standard expression for the delta function

$$\delta(x) = \frac{1}{2\pi} \lim_{\varepsilon \rightarrow 0^+} \left( \frac{2\varepsilon}{x^2 + \varepsilon^2} \right) = \frac{i}{x + i0^+} - \frac{i}{x - i0^+} \quad (32)$$

the matrix delta-function takes the form

$$\delta(E\hat{I} - \hat{H}) = \frac{i}{2\pi} \left( \left[ (E + i0^+)\hat{I} - \hat{H} \right]^{-1} - \left[ (E - i0^+)\hat{I} - \hat{H} \right]^{-1} \right). \quad (33)$$



Substitution of eq. (33) into (31) gives the density matrix

$$\hat{\rho}_k = \frac{1}{2\pi} \int_{-\infty}^{\infty} f_0(E + \varepsilon_k - \mu) \hat{A}(E) dE, \quad (33)$$

where  $\hat{A}(E)$  is the spectral function defined in eq. (24). It can be concluded from eq. (34) that the spectral function  $A/2\pi$  can be interpreted as the available density of states populated up to the Fermi level.

The relation between density of states for finite and opened systems can be understood from the following arguments. The density of states in the case of finite systems is given by:

$$N(E) = \sum_{\alpha} \delta(E - \varepsilon_{\alpha}). \quad (34)$$

Dirac delta-function can be defined as a limiting case of an infinitesimally narrow Lorentzian function

$$\delta(E - \varepsilon) = \lim_{\gamma \rightarrow 0} \frac{1}{2\pi} \frac{\gamma}{(E - \varepsilon)^2 + (\gamma/2)^2}. \quad (35)$$

Using the complex eigenenergies (22) of the opened system, and substituting eq. (35) into (34), a generalized form of the density of states is obtained

$$N(E) = \frac{1}{2\pi} \text{Tr}[A(E)], \quad (36)$$

where the trace on the spectral density is given by:

$$\text{Tr}[A(E)] = \int A(\mathbf{r}, \mathbf{r}) d\mathbf{r} = \sum_{\alpha} \frac{\gamma_{\alpha}}{(E - \varepsilon_{\alpha 0} + \Delta_{\alpha})^2 + (\gamma_{\alpha}/2)^2}. \quad (37)$$

The local density of states is an important property for the analysis of the electronic and transport properties both of opened and closed systems. In analogy to the derivation of the total density of states given above, the local density of states will be also derived inductively, from the form for the closed system

$$\rho(\mathbf{r}, E) = \sum_{\alpha} |\psi_{\alpha}(\mathbf{r})|^2 \delta(E - \varepsilon_{\alpha}). \quad (38)$$

Representing the Dirac delta-function with the limit of a Lorentzian function, and substituting the energy  $\varepsilon_{\alpha}$  by the complex form (21) of the opened system, the generalized local density of states obtains the following form:

$$\rho(\mathbf{r}, E) = \frac{1}{2\pi} A(\mathbf{r}, \mathbf{r}; E). \quad (39)$$

Utilizing the definition (24) of the spectral density  $A = i[G^R - G^A]$  in conjunction with the transforming property (11) between retarded and advanced Green's functions  $G^A = [G^R]^{\dagger}$  leads to the functional dependence of the local density of states on diagonal elements of the Green's function:

$$\rho(\mathbf{r}, E) = -\frac{1}{\pi} \text{Im}[G^R(\mathbf{r}, \mathbf{r}; E)]. \quad (40)$$

#### 2.4.6 Electronic current

The broadening function  $\Gamma$  (see eq. (27)) is defined from the self-energy, which, on the other hand, determines the electron lifetime, or equivalently, the rate at which the electrons escape to/from the electrodes from/to the scattering region. Hence, it can be shown that  $\Gamma/\hbar$  represents the escape rate. The energy-resolved current outflow into the electrode  $p$

can be found as a quantum statistical expectation value of the escape rate, weighted by the density matrix

$$I_{\text{out}}(E) = \text{Tr} \left[ \frac{\hat{\Gamma}_p \hat{\rho}}{\hbar} \right], \quad (41)$$

where  $\hat{\rho}$  is a density matrix of the scattering region. The density matrix can be evaluated from the summation of eq. (33)

$$\hat{\rho} = \sum_k \rho_k = \frac{1}{2\pi} \int F(E - \mu) \hat{A}(E) dE, \quad (42)$$

where  $F(E - \mu) = \sum_k f_0(E + \varepsilon_k - \mu)$ . From eq. (42) the energy resolved density matrix can be also obtained

$$\hat{\rho}(E) = \frac{1}{2\pi} F(E - \mu) \hat{A}(E). \quad (43)$$

For the later use, it is convenient to expand the density matrix from eq. (43) into a sum of contributions from each electrode (we assume only two electrodes, but the generalization for arbitrary number of leads is straightforward):

$$\hat{\rho}(E) = \frac{1}{2\pi} [F_p \hat{A}_p(E) + F_q \hat{A}_q(E)]. \quad (44)$$

Hence, the electronic states are populated with electrons from both electrodes. The total current escaping the scattering region is the current spectrum summed over all energies

$$I_{\text{out}} = -q \int I_{\text{out}}(E) dE, \quad (45)$$

where  $q$  is the elementary charge. The influx current from the electrode into the scattering region can be obtained similar to eq. (45):

$$I_{\text{in}} = -q \int I_{\text{in}}(E) dE. \quad (46)$$

However, the input current spectrum is quantum statistically averaged

$$I_{\text{in}}(E) = \text{Tr} \left[ \frac{\hat{\Gamma}_p \hat{\rho}_p}{\hbar} \right], \quad (47)$$

where the density matrix

$$\hat{\rho}_p \equiv \frac{1}{2\pi} \left( F_p \hat{A}_p(E) + F_p \hat{A}_q(E) \right) \quad (48)$$

is used to weight the averaging in eq. (47). The spectral density of each electrode in the system contributes to the density matrix. The influx and outflux currents of the contact  $p$  are equal for the system at the steady-state current flow. Therefore, the total current at the contact  $p$  can be obtained by equalizing  $I_{\text{in}}(E)$  and  $I_{\text{out}}(E)$ , which yields

$$I = -\frac{q}{h} \int \text{Tr} \left( \hat{\Gamma}_p \hat{A}_q \right) (F_p - F_q) dE. \quad (49)$$

A similar expression holds for the terminal current at the contact  $q$ :

$$I = -\frac{q}{h} \int \text{Tr} \left( \hat{\Gamma}_q \hat{A}_p \right) (F_p - F_q) dE. \quad (50)$$

The expressions (49) and (50) for the current have exactly the same form as in the Landauer-Buttiker formalism<sup>17</sup>:

$$I = -\frac{q}{h} \int T(E) (F_p - F_q) dE, \quad (51)$$

Comparison of eq. (50) and (51) yields the expression for the transmission

$$T(E) = \text{Tr}(\hat{\Gamma}_q \hat{A}_p), \quad (52)$$

which can be further transformed using relation (28) into the final form:

$$T(E) = \text{Tr}(\Gamma_p G^R \Gamma_q G^A). \quad (53)$$

The relationship (53) for the transmission function is the main result directly applicable for the applications in the research of the electronic transport of the molecular systems and solids.



### 3 Unique structural and transport properties of molybdenum chalcogenide nanowires

*Ab initio density functional and quantum transport calculations based on the nonequilibrium Green's function formalism are employed to compare structural, electronic, and transport properties of  $\text{Mo}_6\text{S}_{6-x}\text{I}_x$  nanowires with carbon nanotubes. The systems with  $x = 2$  are found to be particularly stable and rigid, with their electronic structure and conductance close to that of metallic (13,13) single-wall carbon nanotubes.  $\text{Mo}_6\text{S}_{6-x}\text{I}_x$  nanowires are conductive irrespective of their structure, more easily separable than carbon nanotubes, and capable of forming ideal contacts to Au leads through thio-groups.*

#### 3.1 Introduction

Chalcogenides of molybdenum and other transition metals are known to form stable, intriguing 2- and 1-dimensional structures<sup>99</sup> with an unusual combination of electronic properties<sup>93</sup> including good conductance, superconductivity, magnetism, and nonlinear polarizability. These layered or filamentous substances are known as catalysts<sup>100</sup> and, to a much larger degree, as excellent solid lubricants<sup>100-102</sup>. Their potential to become unique building blocks of nano-devices has barely been noticed so far<sup>100</sup>, in stark contrast to popular carbon nanotubes<sup>103</sup>. Recent progress in the synthesis of  $\text{Mo}_x\text{S}_y\text{I}_z$  nanowires<sup>104</sup> with no involvement of alkali counter-ions suggests that these monodisperse, self-supporting nanostructures may nicely complement carbon nanotubes by avoiding their shortcomings such as a strong dependence of conductivity on the nanotube structure characterized by their chiral index (n,m) and difficulty to separate bundled tubes<sup>103</sup>.

In the present chapter *ab initio* density functional theory<sup>43, 105</sup> and quantum transport calculations based on the nonequilibrium Green's function formalism<sup>106, 107</sup> are combined in

order to compare structural, electronic, and transport properties of  $Mo_6S_{6-x}I_x$  nanowires (NWs) to those of carbon nanotubes (CNTs). It will be shown that systems with iodine content  $x = 2$  to be particularly stable and rigid, with their electronic structure and conductance close to that of metallic (13,13) single-wall carbon nanotubes.  $Mo_6S_{6-x}I_x$  nanowires are conductive irrespective of their structure and capable of forming ideal contacts to Au leads through thio-groups. Due to the weak inter-wire interaction,  $Mo_6S_{6-x}I_x$  systems should be more easily separable than carbon nanotubes.

As mentioned before, chalcogenide compounds containing  $Mo$  and  $S$  have been studied for a long time<sup>99, 108</sup>. Whereas the best known allotropes, including  $MoS_2$ , are insulating and form layered compounds, more interesting structures often occur at lower sulfur concentrations. Well known are Chevrel phases, characterized as cluster compounds with  $Mo_6S_8$  subunits, furthermore finite clusters with a similar structure, and needle-like quasi-1D compounds<sup>109</sup>. All these interesting structures necessitate the presence of metal counter-ions for their synthesis. Besides providing structural stability, the main role of the counter-ions is to transfer electrons into the chalcogenide substructures<sup>23, 110</sup> thereby forming an ionic crystal<sup>111</sup>. In their most stable electronic configuration, many of these compounds contained  $(Mo_6S_6)^{2-}$  building blocks<sup>108</sup>.

The main idea of the present chapter is to study the possibility of stabilizing  $Mo$ -based nanowires by substituting the divalent sulfur by a monovalent halogen (I) with a similar electronegativity. In this way, the “magic” electronic configuration could be preserved, while maintaining a covalent character of the system and avoiding the formation of an ionic crystal, where electron correlations would dominate the electronic structure. In the following is presented the study of the properties of  $Mo_6S_{6-x}I_x$  nanowires, where iodine was used to substitute for sulfur.

### 3.2 Computational details

To gain insight into structural and electronic properties of the proposed systems, the geometry of infinite  $Mo_6S_{6-x}I_x$  nanowires is optimized for  $x = 0 - 6$  using density functional theory (DFT). Perdew-Zunger<sup>55</sup> form of the exchange-correlation functional has been



employed in the local density approximation (LDA) to DFT, as implemented in the SIESTA code<sup>112</sup>. The behavior of valence electrons was described by norm-conserving Troullier-Martins pseudopotentials<sup>61</sup> with partial core corrections in the Kleinman-Bylander factorized form<sup>113</sup>. Double-zeta basis is employed in the calculations, including initially unoccupied *Mo*5p orbitals.

To accelerate the global structure optimization of the nanowires with 36-72 degrees of freedom per unit cell, the configurational space was explored and pre-optimized the systems using the faster density functional based tight binding (DFTB) method<sup>63, 114</sup>, which had been used successfully to describe the deformation of *MoS*<sub>2</sub> layers to tubular structures<sup>79</sup>, as well as other molybdenum chalcogenide systems<sup>115-117</sup>.

### 3.3 Details on the atomic structure

The numerical results were obtained for the primitive unit cell of length *a*, containing 12 atoms, depicted in **Figure 5**. In order to explore the effect of structural constraints, for

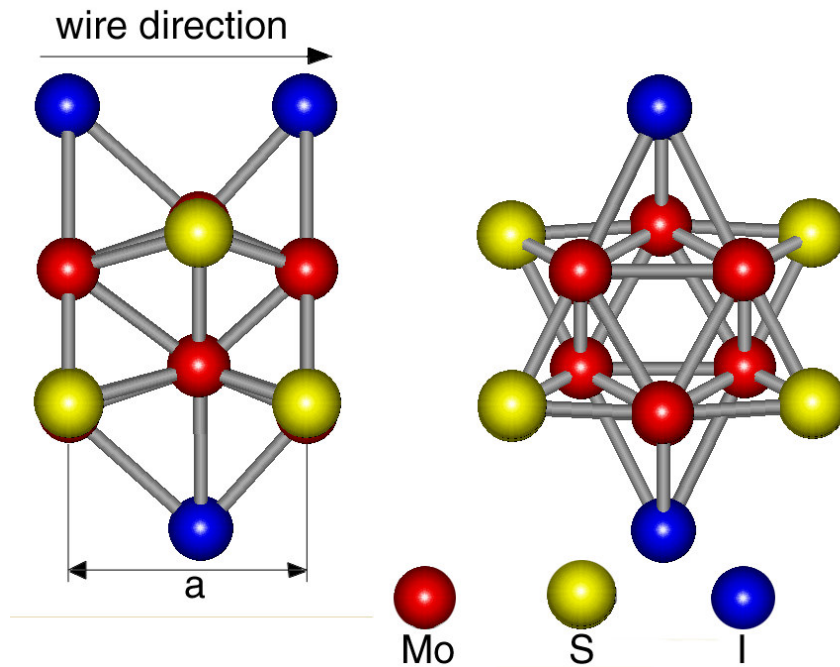


**Figure 5:** Schematic presentation of the atomic structure of a *Mo*<sub>6</sub>*S*<sub>6-*x*</sub>*I*<sub>*x*</sub> nanowire in side and end-on view.

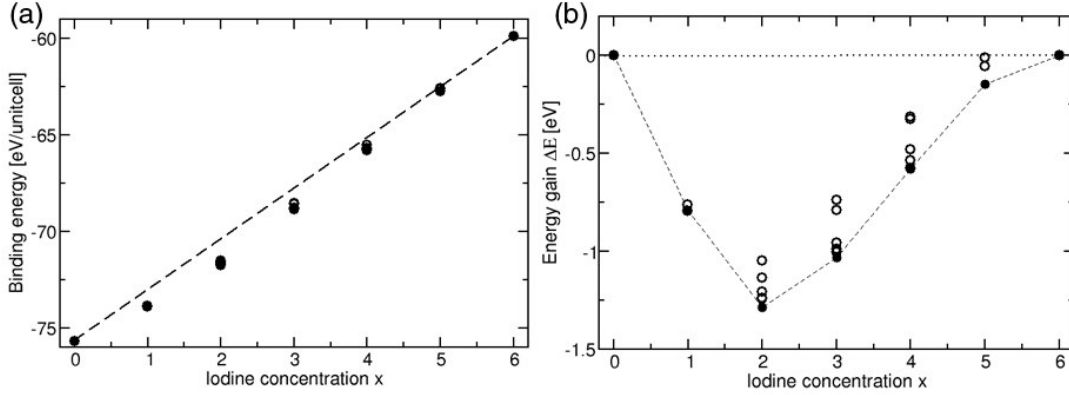


**Figure 6:** (a) Binding energy of the nanowires with respect to the iodine content  $x$ . (b) Energy gain upon forming a  $Mo_6S_{6-x}I_x$  nanowire from noninteracting  $Mo_6S_6$  and  $Mo_6I_6$  segments of proper length ratio. Binding energy presented in (a) is defined as difference between the energy of  $Mo_6S_{6-x}I_x$  nanowires and the atomic energies of their constituting  $Mo$ ,  $S$ , and  $I$  atoms.

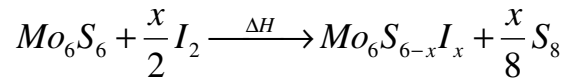
selected structures, the results are compared to those for a double unit cell with 24-atoms. To describe isolated nanowires while using periodic boundary conditions, the nanowires are arranged on a tetragonal lattice with a large inter-wire separation of 20 Å. The rather short Brillouin zone of these 1D structures was sampled by at least 8 k-points. The charge density and potentials were determined on a real-space grid with a mesh cutoff energy of 150 Ry, which was sufficient to achieve a total energy convergence of better than 2 meV/atom during the self-consistency iterations. Maximum force on atom sites of 0.04 eV/Å was criterium for the convergence of the structural optimizations.

The optimized structure of  $Mo_6S_{6-x}I_x$  nanowires, shown in **Figure 5**, consists of a  $Mo$  backbone decorated by  $S$  and  $I$  ligands. The  $Mo$  core structure is formed by  $Mo$  trimers of alternating orientation forming a chain. There is one  $Mo_6S_6$  octahedron per unit cell, surrounded by  $(6-x)$  sulfur atoms and  $x$  iodine atoms. For each value of  $x$  an exhaustive isomer search and a global structure optimization was performed. In general, the  $Mo-Mo$  bond length increases from about 2.6 Å when close to sulfur to about 2.7 Å when close to the larger iodine. Introduction of iodine also causes an increase of the equilibrium lattice constant from  $a_{eq}(Mo_6S_6) = 4.34$  Å to  $a_{eq}(Mo_6I_6) = 4.55$  Å.

The calculations showed that  $Mo_6S_{6-x}I_x$  nanowires to be rather stable, with an average binding energy per atom ranging from 5.0 eV in  $Mo_6I_6$  to 6.3 eV in  $Mo_6S_6$  with respect to isolated atoms (see **Figure 6** (a)). The nanowires thus rival the stability of graphite with 7.3 eV/atom, and the slightly less stable carbon nanotubes. Changing the iodine content  $x$  in  $Mo_6S_{6-x}I_x$  nanowires, one could naïvely expect the binding energy  $E$  to vary linearly between that of  $Mo_6S_6$  and  $Mo_6I_6$ , showing no dependence on the particular structural isomer. In reality, deviations from this linear behavior, depicted as  $\Delta E$  in **Figure 6** (b), are substantial, suggesting that the stability of the various structural isomers at a particular composition varies by up to a large fraction of an eV.  $\Delta E$  is the energy gain upon forming a  $Mo_6S_{6-x}I_x$  nanowire from noninteracting  $Mo_6S_6$  and  $Mo_6I_6$  segments of proper length ratio. Focusing on the most stable isomers, a general tendency is obtained to selectively stabilize particular chalcogenide stoichiometries, such as  $Mo_6S_4I_2$ . As it will be shown below, this “magic” composition optimizes the electronic configuration of the building blocks to agree with the optimum charge state identified above using heuristic arguments.

Among the many structural isomers of  $Mo_6S_{6-x}I_x$ , the structures with the largest separation between iodine atoms are the most stable. When increasing the variational freedom in the arrangement of iodine atoms by doubling the unit cell size, the geometries are identified that further stabilize the structures by providing energy gain per unit cell ranging from 0.09 eV for  $x = 1$  to 0.29 eV for  $x = 3$ .

The selectivity of a possible synthesis pathway becomes apparent, when studying the reaction energy  $\Delta H$  of the substitution reaction



depicted in **Figure 7**. Clearly, substitution of sulfur in  $Mo_6S_6$  by gas-phase iodine is only exothermic for the “magic” iodine content  $x = 2$ .

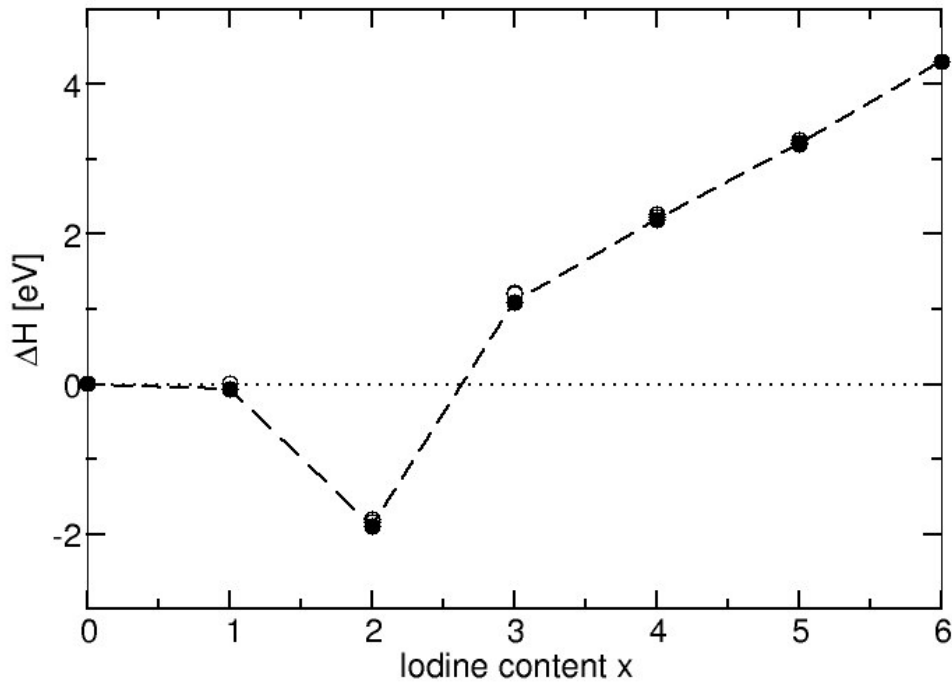


**Figure 7:** Energy  $\Delta H(x)$  of the substitution reaction (see text) leading to the formation of a  $Mo_6S_{6-x}I_x$  nanowire as a function of composition. Among the data points for all structural isomers (empty circles), the most stable structures are identified by solid circles.

It should be noted that one of the products of the reaction is the cluster  $S_8$  that is an unusually stable system<sup>118</sup>.

In the following, the various properties of  $Mo_6S_{6-x}I_x$  nanowires to those of carbon nanotubes are compared. As will become clear later on, the electronic structure of the chalcogenide nanowires matches well that of a conducting (13,13) carbon nanotube with a diameter of 17.6 Å. The equilibrium unit cell size  $a_{eq}(13,13) = 2.46$  Å of the armchair nanotube is about half the value of the “magic” nanowire,  $a_{eq}(Mo_6S_4I_2) = 4.45$  Å.

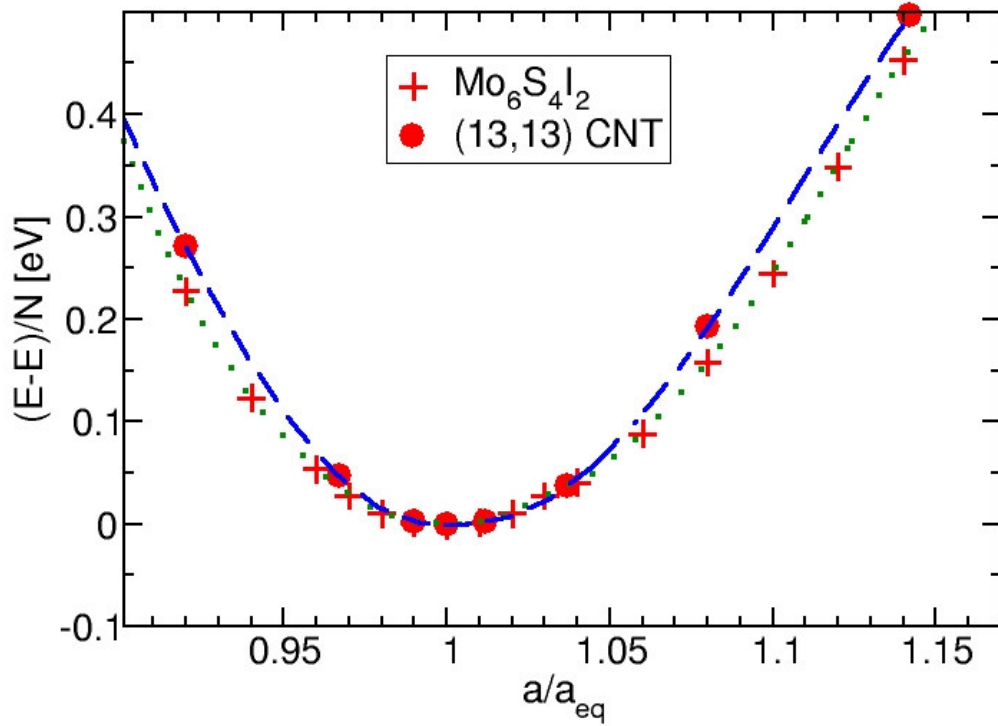


**Figure 8:** Deviation from the equilibrium binding energy  $E_0$  as a function of the relative unit cell size  $a/a_{eq}$ , for a segment of a magic  $Mo_6S_4I_2$  nanowire containing  $N$   $Mo$  atoms, and for an  $N$ -atom segment of the (13,13) carbon nanotube.

The axial stiffness of a  $Mo_6S_4I_2$  nanowire in comparison to that of a (13,13) carbon nanotube can be inferred from **Figure 8**. In order to have a fair comparison between the different systems, the energy investment upon axial strain should be normalized by the number of  $Mo$  backbone atoms in the nanowire and number of  $C$  atoms in the nanotube. Inspection of the results in **Figure 8** suggests that the high axial stiffness, based on the above definition, is nearly the same in the two systems. The  $Mo_6S_4I_2$  nanowire differs significantly in its rigidity from the accordion-like behavior identified recently in the “floppy”  $Mo_6S_{4.5}I_{4.5}$  nanowire<sup>119</sup>.

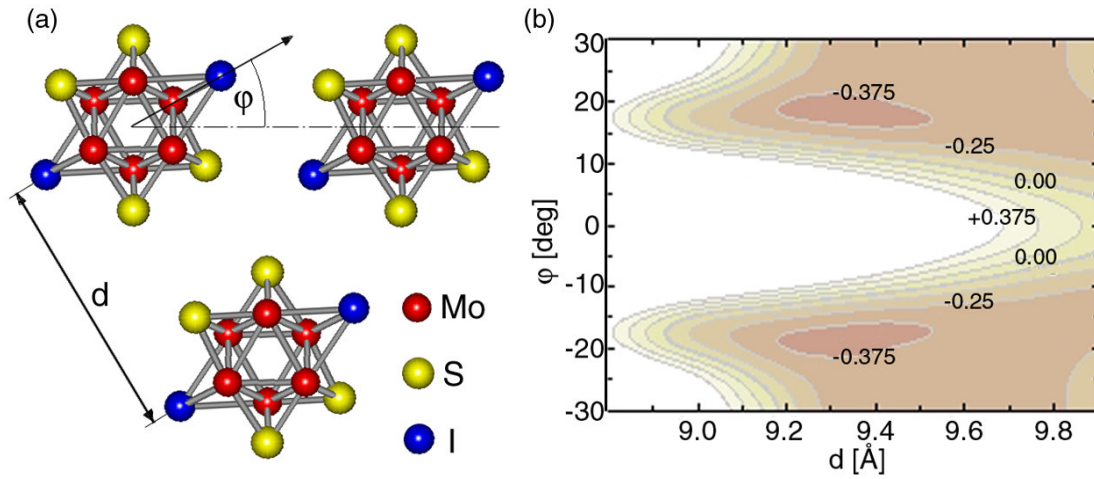


**Figure 9:** (a) Structure of  $Mo_6S_4I_2$  nanowires arranged on a simple hexagonal lattice in a plane normal to the wire axes. (b) Contour plot of the nanowire binding energy in this lattice as a function of the wire orientation  $\phi$  and separation  $d$ . The energy is given in eV per formula unit.

Contrasting with the high stability and axial stiffness of the  $Mo_6S_4I_2$  nanowires is their lateral inter-wire interaction, discussed in **Figure 9**. The binding energy of straight nanowires on a simple hexagonal lattice with respect to isolated nanowires was calculated using DFTB, augmented by Van der Waals interactions<sup>120</sup>. The results for the binding energy as a function of the inter-wire separation  $d$  and the wire orientation  $\phi$  obtained using the relaxed atomic arrangement of an isolated nanowire, are presented in **Figure 9** (b). The binding energy is found to be generally weak and strongly anisotropic. The most stable arrangement occurs at an inter-wire separation  $d = 9.3$  Å. The binding energy in this geometry corresponds to 0.1 eV for a 1 Å long nanowire segment and equals that of a corresponding segment of bundled (10,10) CNTs<sup>121</sup>. In realistic bundles, individual nanowires and nanotubes are likely to be twisted rather than being perfectly straight over long distances<sup>122</sup>. Then, their effective interaction should be closer to an average over all possible orientations. Due to its anisotropy, seen in **Figure 9** (b), the effective attraction between  $Mo_6S_4I_2$  nanowires is strongly reduced or changes to repulsion when averaging over  $\phi$ , whereas the rather isotropic interaction between nanotubes does not affect their strong binding<sup>121</sup>. For comparison CNTs gain about 9 meV per atom when mounted to a (10,10) bundle, which corresponds to  $40 \times 9 \text{ meV} / 2.46 \text{ Å} = 150 \text{ meV/Å}$ . This explains the observation that bundled chalcogenide nanowires are much easier to separate than bundled carbon nanotubes.

### 3.4 The electronic structure

Among the different properties of  $Mo_6S_{6-x}I_x$  nanowires, the electronic structure is found to be most intriguing. In **Figure 10** are compared the band structure  $E(k)$ , the density of states (DOS), and ballistic conductance of isolated  $Mo_6S_4I_2$  and  $Mo_6S_6$  nanowires to those of an isolated  $(n,n)$  single-wall carbon nanotube. Independent of composition, all  $Mo_6S_{6-x}I_x$  nanowires are metallic or semi-metallic. This is appealing in view of the fact that carbon nanotubes may be conducting or semiconducting, depending on their chiral index  $(n,m)$ <sup>103</sup>.

In **Figure 10** (a-f), the electronic properties of the  $Mo_6S_4I_2$  and the  $Mo_6S_6$  nanowires can be compared side-by side. External gating or doping can furthermore be used to shift the Fermi level of the chalcogenide NWs, as indicated by the dotted lines in **Figure 10**. Similar to conducting  $(n,n)$  carbon nanotubes, an energy range with a constant DOS is present also near the Fermi energy of the gated chalcogenide NWs, suggesting high electron mobility, which is flanked by a pair of van Hove singularities. As can be seen by comparing **Figure 10** (e) and (h), the energy separation of the van Hove singularities in the  $Mo_6S_6$  nanowire is best matched by the metallic (13,13) carbon nanotube. For the sake of easy comparison with carbon nanotubes, the focus on the externally gated/doped chalcogenide NWs is made in the following.

The band dispersion of gated  $Mo_6S_{6-x}I_x$  nanowires and the (13,13) carbon nanotube are compared in the left panels of **Figure 10**. In all three systems considered nearly free-electron bands can be identified in the vicinity of  $E_F$ . Whereas the constant DOS near  $E_F$  in the (13,13) carbon nanotube, shown in **Figure 10** (h), derives from bands of C2p- $\pi$  character, a very similar constant DOS of  $Mo_6S_6$  in **Figure 10** (e) derives from  $a_2$  bands<sup>108</sup> with predominant Mo4d- $\sigma$  character. In general, the stability of any system is expected to increase when populating bonding or depopulating antibonding states. In  $Mo_6S_{6-x}I_x$  nanowires, the optimum stabilization is achieved by filling the Mo4d-derived  $a_2$  band up to the folding point at  $x$ .

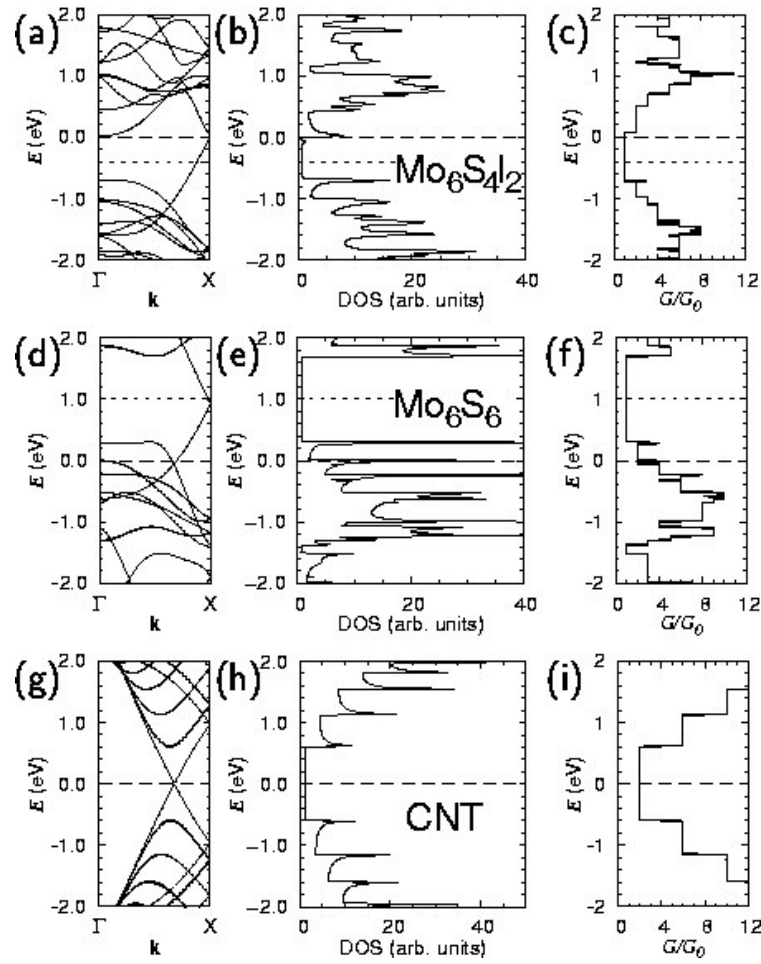


**Figure 10:** Electronic properties of a  $Mo_6S_{6-x}I_x$  nanowire (a)-(f) in comparison to a (13,13) carbon nanotube (g)-(i). Displayed is the band structure  $E(k)$  of the  $Mo_6S_{6-x}I_x$  nanowires in (a),(d) their DOS in (b), (e), and quantum conductance  $G(E)$  in units of the conductance quantum  $G_0$  (c), (f). The corresponding quantities for the (13,13) carbon nanotube are shown in (g)-(i).  $E = 0$ , given by the dashed lines, corresponds to the Fermi level in (a),(b),(d),(e),(g),(h), and to zero source-drain voltage in (c),(f),(i). The dotted lines show the position of  $E_F$  in externally gated or doped chalcogenide nanowires resembling carbon nanotubes. Data in this figure is obtained by DFT method (SIESTA and TranSIESTA).

As suggested by comparing **Figure 10** (a,d), (b,e), the main effect of changing the composition of  $Mo_6S_{6-x}I_x$  nanowires by iodine substitution prior to gating is to electronically dope the system by shifting the Fermi level. This finding agrees qualitatively with that in  $Li_2Mo_6S_6$  nanowires<sup>111</sup>, where the most stable  $x = 2$  composition has been associated with the “magic”  $(Mo_6S_6)^{2-}$  complexes. As suggested above, stabilization of the system should depend on the oxidation state of the  $Mo$  backbone. In that case, initial withdrawal of 12 electrons



from  $Mo_6$  by divalent sulfur ligands, followed by adding two electrons to  $Mo_6$  in the “magic”  $(Mo_6S_6)^{2-}$  complexes, should be equivalent to withdrawing only 10 electrons from  $Mo_6$  in the first place, by substituting two divalent sulfurs by monovalent iodines. Further increase in the concentration of  $Li$  or  $I$  should increase the population of the antibonding levels and thus destabilize the system. This reasoning is confirmed by the observed unusual stability of  $Li_2Mo_6S_6$  and  $Mo_6S_4I_2$ , both of which should display a similar electronic configuration of the  $Mo$  backbone.

In order to understand the interplay between doping and structural changes, DFTB calculations of  $(Mo_6S_6)^{q-}$  nanowires carrying  $q = 0...6$  extra electrons per unit cell have been performed. This artificial doping first increases the population of the  $Mo4d$ -derived bonding and subsequently the antibonding states. This effect is competing with the destabilization caused by Coulomb repulsion of additional electrons, which increases with  $q$ , and causes the elongation of the equilibrium unit cell size from 4.34 Å for  $q = 0$  to 4.40 Å when the unitcell is charged with 6 additional electrons (see **Figure 11**).

As seen in **Figure 10** (a,d), substituting sulfur by iodine atoms in  $Mo_6S_{6-x}I_x$  not only shifts the Fermi level, but also opens a narrow band gap, while introducing a new band above  $E_F$ . This nearly free-electron band of predominantly  $Mo4d$  character is also observed in the Li doped  $Mo_6S_6$  system<sup>111</sup> and caused by locally changing the crystal potential along the chains of I or Li atoms in the crystal.

Addressing the usefulness of  $Mo_6S_{6-x}I_x$  nanowires as ballistic conductors, their quantum conductance  $G$  has been calculate as a function of the carrier injection energy  $E$  using the Green's function approach<sup>106, 107</sup>. The conductance results for  $x = 2$  and  $x = 0$ , presented in **Figure 10** (c) and (f), are compared to those for a (13,13) carbon nanotube in **Figure 10** (i). In the gated chalcogenide NWs, the  $Mo4d$  character of the states near  $E_F$  suggests that conduction involves mostly the  $Mo$  backbone and not the ligands.

Since all these systems are metallic, with a constant density of states near  $E_F$ , similarities in the conductance spectra of gated  $Mo_6S_{6-x}I_x$  nanowires and metallic carbon nanotubes are apparent. Even moderate doping should shift the Fermi level into the region of

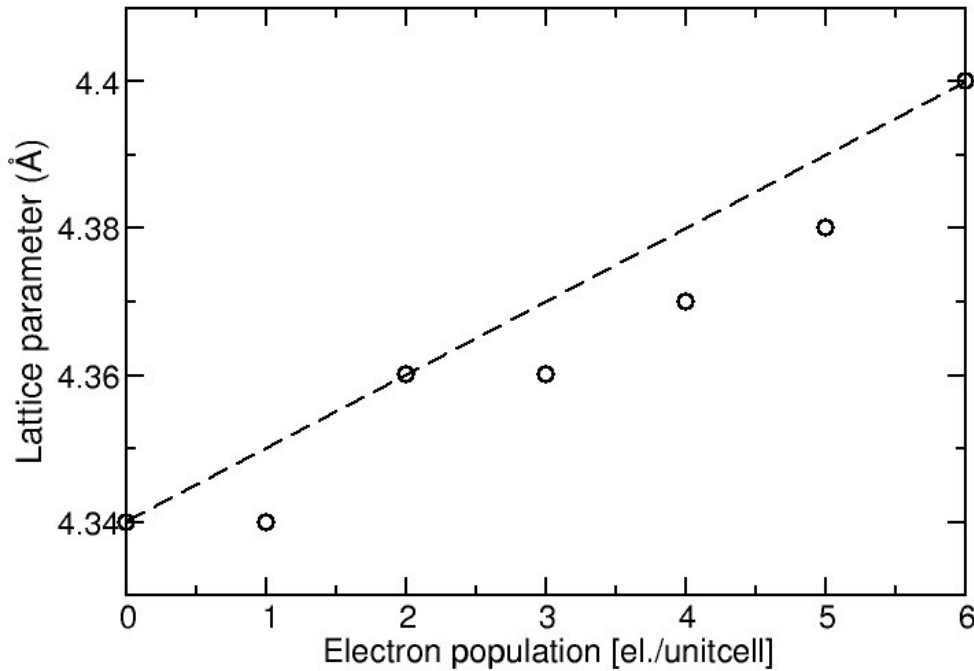


**Figure 11:** Dependence of the lattice parameter on the electron population of  $Mo_6S_6$  nanowire. Dash line is give as a visual guide.

van Hove singularities and thus significantly enhance their conductivity. A major advantage of  $Mo_6S_{6-x}I_x$  nanowires is the natural termination of finite segments by sulfur atoms, which are known to bind to  $Au$  electrodes as thio-groups. The nature of the contacts between the molybdenum sulfide nanowire and  $Au$  electrodes will be analyzed in detail in one of the following chapters.

### 3.5 Conclusions

In conclusion of the present chapter, *ab initio* density functional and quantum transport calculations have been conducted in order to compare structural, electronic, and transport properties of  $Mo_6S_{6-x}I_x$  nanowires with carbon nanotubes. The  $Mo_6S_4I_2$  system may form particularly stable, free-standing quasi-1D nanowires with electronic structure and conductance close to that of metallic (13,13) single-wall carbon nanotubes.  $Mo_6S_{6-x}I_x$

nanowires have advantageous properties in comparison to carbon nanotubes by being conductive irrespective of their structure and more easily separable from the ropes of the nanowires.



## 4 Reliability of the DFTB method for description of energetic and electronic properties of the molybdenum chalcogenide nanowires

*In this chapter a comparison of the results obtained with the density functional theory (DFT) (which are given in **Chapter 3**) and the density-functional based tight-binding (DFTB) method will be presented. Most of the calculations from the remaining parts of thesis are performed for large structures that often include more than three hundred atoms, which is too cumbersome for full self-consistent field DFT calculations. Being more accurate but not-practical for further studies on the nanometer-sized devices, which spatial dimensions exceed ten nanometers, the density functional theory has to be replaced with a faster method. The method of choice in the thesis is DFTB. This method is not only 2-3 orders of magnitude faster than full DFT, but also, as it will be demonstrated below, it has similar qualitative and in many cases quantitative agreement with results obtained by the DFT method.*

### 4.1 Comparison of binding energies

In order to get insight into the correspondence between the DFT and DFTB energies of  $Mo_6S_{6-x}I_x$  isomers, the energy gain  $\Delta E(x)$  upon forming of  $Mo_6S_{6-x}I_x$  nanowire from noninteracting  $Mo_6S_6$  and  $Mo_6I_6$  segments of proper length ratio is shown in **Figure 12**. The left panel represents the DFT results, while the right panel shows the results obtained with DFTB. Remarkably, the isomer with the largest energy gain in DFTB calculations has 3 iodine atoms in the unitcell, which is in clear contrast to the DFT results showing that the largest energy gain corresponds to the isomers with 2 iodine atoms per unitcell. The DFT value of the energy gain for the preferable iodine content of  $x = 2$  is about 0.25 eV larger than the DFTB value. Additionally, the minimum of the DFT curve is more pronounced compared to other isomers than the minimum of DFTB energies. In the DFT results all structures with  $x = 2$  gain more energy than any other isomer with different

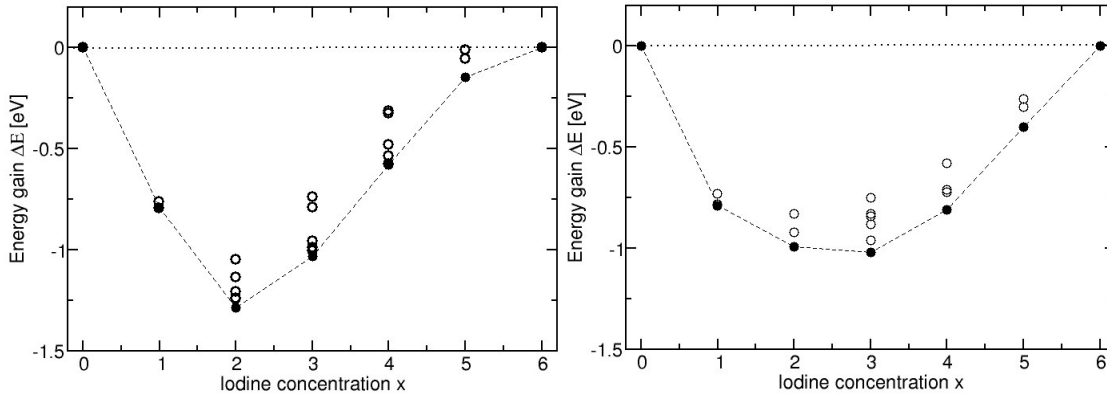


**Figure 12:** Energy gain upon forming a  $Mo_6S_{6-x}I_x$  nanowire from noninteracting  $Mo_6S_6$  and  $Mo_6I_6$  segments of proper length ratio obtained with DFT (left panel) and DFTB (right panel).

iodine content. In contrast to the DFT results, the DFTB energy gain has the overlapping energy regions for a broad range of isomers (for  $x$  values in range from 1 up to 4) and arrangements of iodine atoms in the unitcell. Apart from these clear differences between DFT and DFTB energetics of the molybdenum chalcogenide wires, there exist also an important similarity. Namely, the DFT and DFTB values of energy ordering for the isomers with fixed iodine content  $x$  ( $x = 1...5$ ) and different arrangement of the iodine atoms in the unitcell appears to be identical.

#### 4.2 Comparison of electronic structure of $Mo_6S_{6-x}I_x$ nanowires calculated with the DFT and DFTB methods

It was shown in **Chapter 3** that stabilization of the  $Mo_6S_{6-x}I_x$  systems depend on the oxidation state of the  $Mo$  backbone. The most preferred iodine composition corresponds to the electronic configuration with the system stabilized after completely populating the bonding electronic band. Additional electrons populate the antibonding state, which destabilizes the system. The reason for the mismatch between the most preferred isomers obtained with DFT and DFTB can be understood inspecting **Figure 13**, where the comparison between electronic band structures of the same  $Mo_6S_4I_2$  isomer in the preferred (for DFT) iodine configuration, obtained with the DFT (a) and DFTB (b) methods is given. In

the band structure calculated with DFT, the bonding and antibonding bands touch at the  $k$ -point  $X$ , which is in contrast to DFTB picture where the touching point is by 0.4 eV above the Fermi level. Therefore, a part of the bonding band is still above the Fermi level in the DFTB results; The additional iodine atom would contribute an electron, which would populate the  $Mo$  bonding state and further stabilize the nanowire.

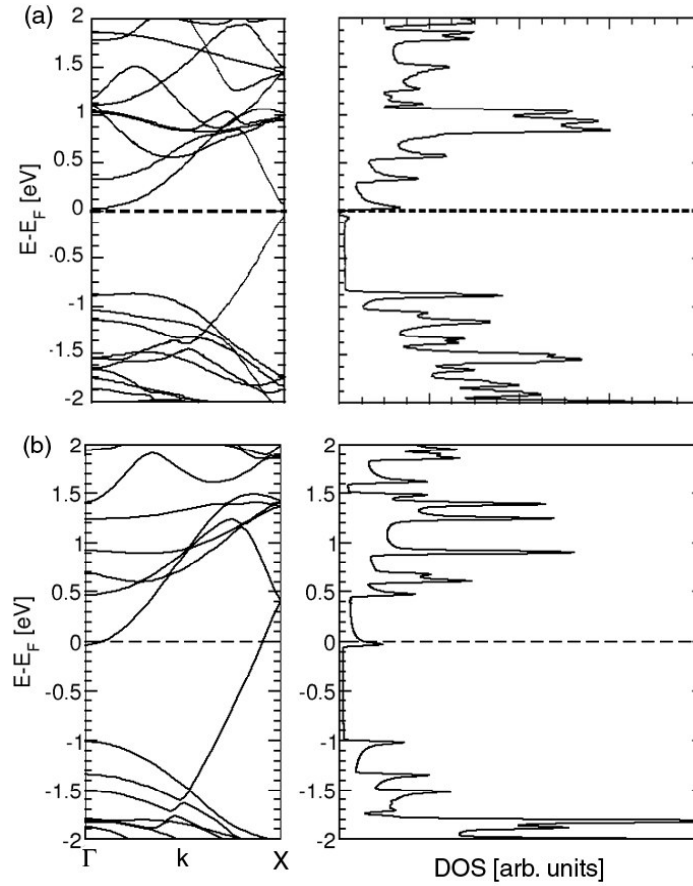


**Figure 13:** Band structure (left panel) and density of states (right panel) of  $Mo_6S_4I_2$  isomer obtained with DFT (a) and DFTB method (b).

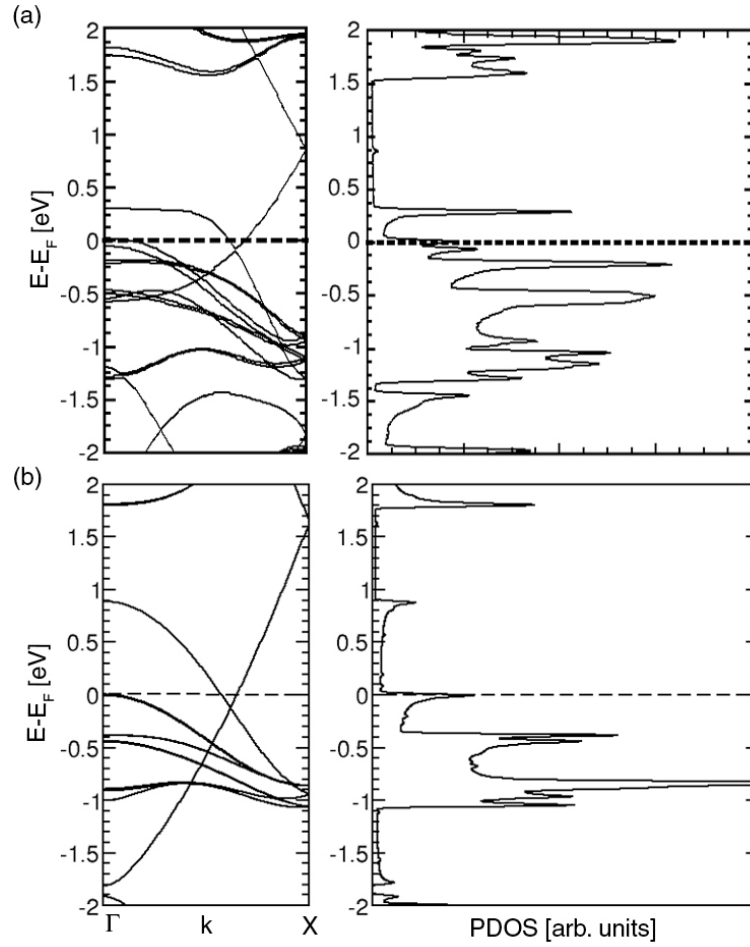


**Figure 14:** Band structure (left panel) and density of states (right panel) of  $Mo_6S_6$  isomer obtained with DFT (a) and DFTB method (b).

Other features of the band structures obtained with the DFT and DFTB methods are qualitatively and in some extent quantitatively in relatively good agreement. For instance, a new electronic band appears at the Fermi level in **Figure 13** due to the local electrostatic potential at the molybdenum backbone originated from the iodine atoms. This band is similar both in the DFT and DFTB methods. Another important feature is the crossing point between the  $a_1$  and  $a_2$  bands in the  $Mo_6S_6$  isomer (just below the Fermi level in **Figure 14**), which is characterized by similar position (about  $0.6 \pi/a_0$ ) and same energy (about  $-0.05$  eV) for the DFT and DFTB calculations. This is important finding, because at that point the band gap opens when the  $Mo_6S_6$  nanowire is twisted, which will be analyzed in detail in **Chapter 5**.



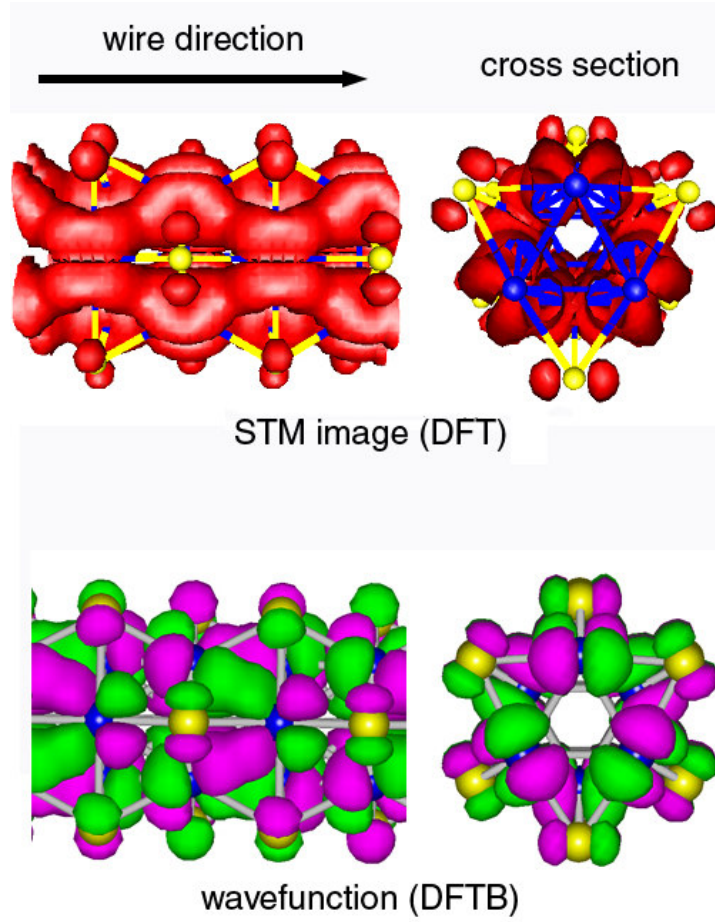


**Figure 15:** (upper panel) Electron density of  $Mo_6S_6$  wire obtained with DFT in the energy range ( $E_F+0.3$  eV,  $E_F+1.0$  eV) where only the  $a_2$  band is present. (lower panel) Wavefunction of the  $a_2$  state obtained with DFTB at the gamma point for the system with 2 unitcells in the supercell.

In order to compare the DFT and DFTB nature of the states around the Fermi level, the integrated electron density (calculated with DFT-Siesta, referred to as scanning tunneling microscopy (STM) image) and the corresponding wavefunctions (calculated with DFTB) were calculated in the energy regions corresponding to certain electronic bands and are shown in **Figure 15** and **Figure 16**. The simulated STM image of the  $Mo_6S_6$  nanowire obtained with DFT for the energy range ( $E_F+1.0$  eV,  $E_F+1.5$  eV) is shown in the upper panel of **Figure 15**. One DFTB wavefunction from this energy range is shown in the lower panel. It can be noticed that in both cases the state consists of  $d_{x^2-y^2}$  atomic orbitals on  $Mo$  sites, which are aligned orthogonal to the alternating triangles of the wire. These atomic orbital

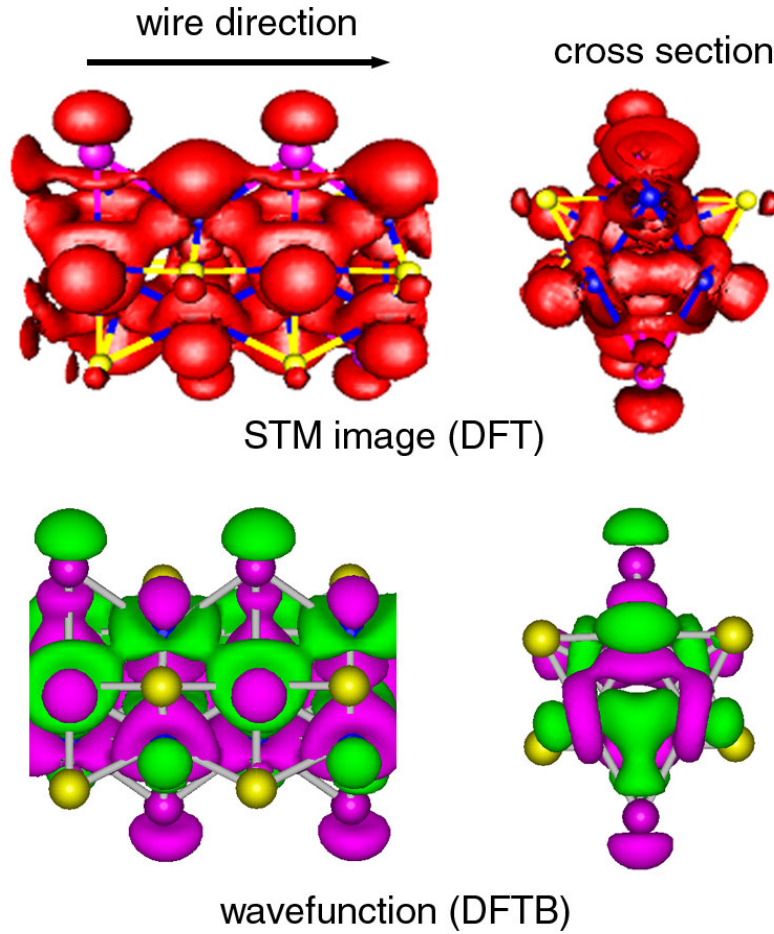


**Figure 16:** (upper panel) Electron density of  $Mo_6S_4I_2$  wire obtained with DFT in the energy range ( $E_F$ ,  $E_F+0.08$  eV) where the new band caused by the local change of the potential due to iodine atoms is present (see text). (lower panel) Wavefunction of this state obtained at the gamma point with DFTB for the system with 2 unitcells in the supercell.

s make  $dd-\sigma$  bonds between the  $Mo$  atoms along the wire. To further verify the good agreement between the DFT and DFTB nature of electronic bands, a similar comparison of STM image and the wavefunction is presented for the  $Mo_6S_4I_2$  isomer in **Figure 16**. In analogy to the previous figure, the upper panel of **Figure 16** shows a simulated STM image of the new band appearing due to the local potential introduced upon the iodine doping (for details see **Chapter 3**). The electron density is integrated in the energy range ( $E_F$ ,  $E_F+0.08$  eV) corresponding to the band mentioned above. In the lower panel a corresponding wavefunction obtained with DFTB method is shown. Inspecting **Figure 16** one can conclude again that DFT and DFTB calculations deliver the same qualitative behavior of the state in

question: It is constructed from the  $I-p$  and  $Mo-d_{z^2}$  orbitals lying in the plane of the alternating  $Mo$  triangles.

### **4.3 Conclusions**

It has been shown in this chapter that the electronic structure of molybdenum chalcogenide nanowires is accurately described by DFTB with respect to DFT. All main features of the electronic bands and density of states obtained with the DFT method are recovered in the DFTB method. Certain differences between the calculated binding energies exist: The most important result of DFT calculations, the stability of the “magic”  $Mo_6S_4I_2$  isomer, is not found with DFTB. However, the energy ordering within the set of isomers with same iodine content  $x$  ( $x = 1...5$ ) is identical both in DFT and DFTB methods.



## 5 Structural and electronic response of $\text{Mo}_6\text{S}_6$ nanowire to mechanical deformations

*The structural, electronic, and transport properties of mechanically deformed  $\text{Mo}_6\text{S}_6$  nanowires have been investigated using a density-functional based tight binding method extended with a Green's functions formalism. Two interesting and important results have been obtained that will be presented in the current chapter. First, the properties of the wire are not affected by bending, and second, a metal-insulator transition occurs when the wire is twisted. This indicates that molybdenum sulfide nanowires can be used as nanocables for flexible transfer of the information between the electromechanical switches that can be also constructed from the same wires. Hence, these interesting properties suggest the  $\text{Mo}_6\text{S}_6$  nanowire as a unique building block for the future nanodevices.*

### 5.1 Introduction

While detailed investigations of the effects of bending and twisting on the electronic transport in CNTs have been performed<sup>22, 123-125</sup>, the response of molybdenum-chalcogenide NWs to mechanical deformation has not been studied in detail, so far<sup>126, 127</sup>. Here, the electronic transport of bent and twisted NWs is investigated. Similar to CNTs, the  $\text{Mo}_6\text{S}_6$  NWs resist uniform bending; up to a curvature of about  $0.18 \text{ nm}^{-1}$ , which results in a bending by ninety degrees along twenty unit cells, the structural integrity of the NW appeared to be intact, and the electron transmission properties practically do not change. Therefore, this type of NW remains metallic even under such deformation, which is considerably larger than the one observed experimentally for Li-separated wires of the selenium analogue<sup>23</sup>. On the other hand, twisting of the NWs causes significant changes of the electronic properties and initiates a metal-insulator transition. Hence the molybdenum-sulfide NW may be used as an

electromechanical switch similar to one experimentally demonstrated with CNTs by Karni *et al.*<sup>22</sup>.

## 5.2 Computational details

The density-functional-based tight-binding (DFTB) method<sup>63, 114</sup> is employed for the calculations of the energies, and a DFTB variant extended by a Green's function formalism<sup>85, 86</sup> is used to determine the conductance properties (electron transmission  $T(E)$ ) which are presented in this chapter. The Ceperly-Alder parametrization of the exchange-correlation functional in the local density approximation (LDA) is employed, including scalar relativistic corrections. The initially unoccupied  $Mo5p$  atomic orbitals are included in the basis set. The parameters employed for the creation of the Hamiltonian and overlap matrices used in the DFTB calculations are described in detail in **Chapter 2.3**. The DFTB method has been used successfully for the successful description of various complex molybdenum-chalcogenide structures<sup>79, 115-117, 128</sup>, which indicates a high reliability of the method for the research of the  $Mo_6S_6$  nanowire.

## 5.3 The investigated geometries of the mechanically deformed nanowires

The investigated geometries of the mechanically deformed NWs are depicted in **Figure 17**. The bending region in **Figure 17** (a) contains twenty unit cells, corresponding to a length of around 9 nm. Prior to the structural relaxation, the initial geometry of the bent NWs is designed with the constraint that alternating triangles of the NWs are positioned perpendicular to the tangent of the bending path, and the wire axis of the bent fragment is aligned along the circle of radius  $R$ . Additionally, the length of the deformed fragment is identical to the corresponding segment of the ideal wire. The structural relaxation prior to the

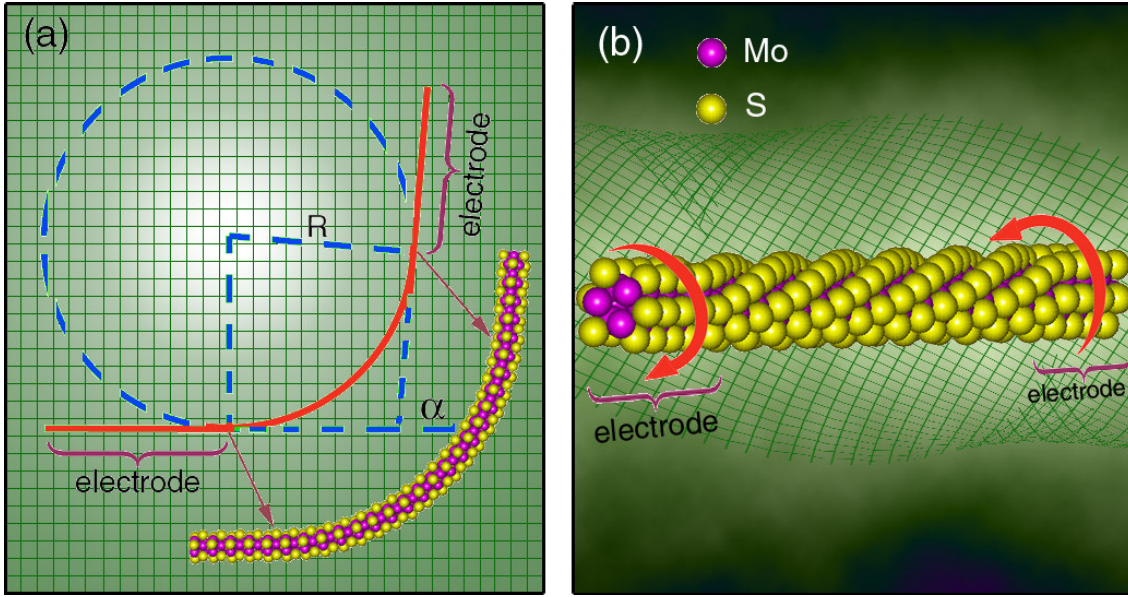


**Figure 17:** The geometry of twisted (a) and bent (b)  $\text{Mo}_6\text{S}_6$  nanowires prior to the structural relaxations. Bent and twisted regions consist of 20 unit cells. Bent region of the NW is along a circle of radius  $R$ , whereas the twisted region is considered as a straight fragment. The electrodes are semi-infinite, ideal, straight nanowires.

transport calculations have been done on finite nanowires, i.e. clusters composed of the deformed region and at its ends two straight wire's segments, both containing four unitcells, and each saturated with one sulfur atom. The atom positions of the straight parts were fixed during the structural relaxation. In the calculations of the transmission function, the straight segments were substituted with two straight semi-infinite  $\text{Mo}_6\text{S}_6$  NWs. The semi-infinite parts were considered as electrodes. The geometry of a twisted NW is shown in **Figure 17** (b). Like in the case of the bent NW, only a central region containing twenty unit cells is twisted, and wire ends are considered as straight finite (semi-infinite) fragments in the structural optimization (transport calculations). This corresponds closely to the experimental setup in the measurements of Karni *et al.*<sup>22</sup> with CNTs.

## 5.4 The energetic and structural properties

First the energetic and structural properties are analyzed. The potential energy of the deformations, defined as a difference between the total energies of straight and deformed NWs, are shown in **Figure 18**. The twisting angle is given in nanometers, and the bending angle  $\alpha$  (given in degrees) is defined as shown in **Figure 17** (a). The parabolic fit (see **Figure 18**) matches the calculated data very well up to a bending angle  $\alpha$  of 90 degrees, which corresponds to a curvature of around  $0.18 \text{ nm}^{-1}$ . This is an indication that the bending does not introduce any plastic deformation to the NW. Careful investigation of the relaxed geometries supports this conclusion; there are no significant reconfigurations of the atomic structure of the bent wire. This flexibility is higher than for carbon nanotubes<sup>123</sup>, which kink due to the bending.

In contrast to the bent NWs, for which the local symmetry of each pairs of the alternating *Mo*-triangles is only slightly perturbed, the homogeneous twisting *a priori* introduces significant changes to the local atomic structure of the nanowire. The *a posteriori*

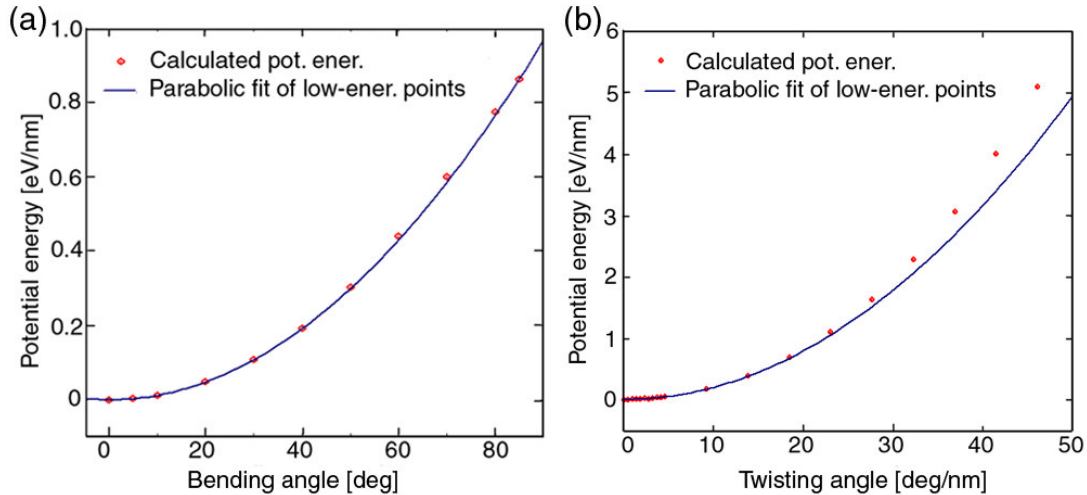


**Figure 18:** Potential energy of bent (a) and twisted (b) geometry. Bending angle corresponds to  $\alpha$  in Figure 17. Data represented with red diamonds in these graphs are obtained after the full structural relaxation. Blue lines are parabolic fits including only calculated energies less than 30 and 10 degrees for the bending and twisting case, respectively.



structural relaxation of the twisted nanowire does not introduce a remarkable additional relocation of the atoms, when the twisting angle is less than 50 deg/nm. For the larger angles the wires have a tendency to bend as observed for CNTs<sup>129</sup>. The deviation from the parabolic fit upon twisting (**Figure 18** (b)) is larger than upon bending, which indicates a plastic process coupled to stronger changes of the electronic structure as the twisting angle increases. Although the twisting energy of the wire is higher than the bending energy, both values are remarkably smaller than the twisting energy obtained for CNTs<sup>123</sup>. Hence, the molybdenum sulfide nanowires are relatively flexible and may easily adapt also to very fine features of a nanostructured template.

## 5.5 The electronic transmission

The dependence of the calculated transmission functions  $T(E)$  with respect to bending and twisting angles are illustrated in **Figure 19** (a) and (b), respectively. It has been shown previously that an ideal, undistorted  $Mo_6S_6$  nanowire<sup>128</sup> exhibits the following regions of constant transmission: From -0.4 eV to Fermi level three open channels exist, up to 0.8 eV there are two open channels, and one open channel is obtained below 1.7 eV. Below -0.4 eV, the transmission is not constant, but rather fluctuates similar to the density of states (DOS) in this energy region. Bending does not have any significant impact on the transmission for bending angles up to 90 degrees, i.e. for curvatures of up to  $0.18 \text{ nm}^{-1}$  an ideal metallic transmission along the wire is obtained.

In contrast, twisting causes significant changes in the transmission of the nanowires. The most remarkable one is the opening of the band gap, starting already at a small twisting angle of 10 deg/nm. The band gap widens linearly and monotonically with increasing twisting angle, and leads to a semiconducting state with a gap of about 0.3 eV for a twisting angle of 45 deg/nm. The oscillations in the transmission spectrum appear between the Fermi level and 0.8 eV. One can note absence of oscillations in PDOS in this region. This indicates that oscillations are not intrinsic to the twisted periodic wire. Therefore, the geometry of the whole device investigated here has to be considered in the analysis of the oscillations. The

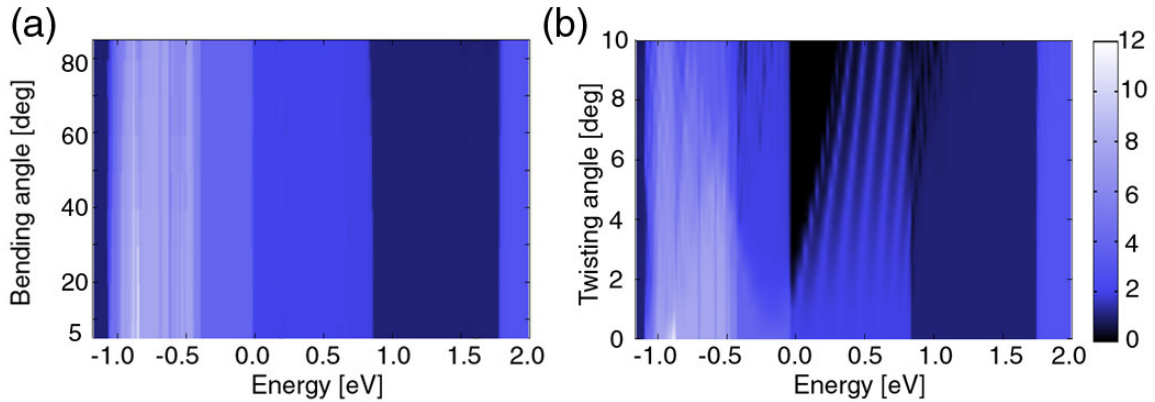


**Figure 19:** Transmission of the bent (a) and twisted (b) nanowire. Fermi level is at zero. On the right side a calibration of the electron transmission is given, where the white shade represents the maximum transmission of 12, and dark blue stands for the minimum one of zero. Y-axis in (b) represent the twisting angles between Mo-triangles. The transmission is calculated in the steps of 10 deg (a) and 1 deg (b), and the transmission data are *a posteriori* extrapolated.

further details will be given in the next paragraph, where the projected density of states is analyzed in detail. The highest value of transmission of the ideal wire is 12, which is about 0.8 eV below Fermi level. Upon twisting, this “hotspot” rapidly fades out as the twisting angle increases.

## 5.6 The origin of the metal-semiconductor transition in bent $Mo_6S_6$ nanowire

To gain a deeper insight into the mechanism of the gap opening in bent  $Mo_6S_6$  nanowire, the projected density of states (PDOS) as shown in **Figure 20** will be analyzed for the ideal non-twisted NW (solid lines) and for one example of a twisted wire (dashed lines), both calculated using periodic boundary conditions. In the twisted wire each subsequent alternating triangle is rotated by 10 degrees with respect to its preceeding one. A super cell consisting of 6 elementary cells is employed in order to generate a smooth twisting between the replicated sections along the wire direction. The Brillouin zone is sampled by 40 k-points

along the axis of the wire. For both wires the contribution from sulfur atoms is considerably smaller than the one from molybdenum atoms in the energy region around the Fermi level. In the ideal wire the states that contribute to the metallic conductivity at the Fermi level classify according to the  $C_{3v}$  symmetry of the wire as  $a_1$ -,  $a_2$ -, and  $e$ -type. The  $e$  state touches the Fermi level close to the  $\Gamma$  point, the  $a_1$  and  $a_2$  states intersect below the Fermi level close to  $k_z = 0.6 \pi/a$  ( $a$  is the lattice parameter). In a twisted NW the symmetry reduced to  $C_3$  and states may classify as either an  $e$ - or an  $a$ -type. In this way the distinction between the  $a_1$  and  $a_2$  bands is lifted and both states are of  $a$ -type character. This results in avoided crossing of the two bands, which opens up a band gap. Besides, two new van-Hove singularities appear at the edges of this band gap. However, the bands that constitute the singularities at these energies do not contribute to the electronic transport; therefore the gap in transmission (see **Figure 19** (b)) is somewhat larger. The maximum of the *Mo* PDOS at -0.8 eV is considerably decreased upon twisting, which explains the rapid decrease of the transmission "hotspot" with increasing the twisting angle. The oscillations that appear between Fermi level and 0.8 eV are not present in the PDOS. Since the PDOS is obtained from the periodic twisted nanowire, the oscillations in transmission function are not intrinsic property of the twisted wire. Therefore, it is necessary to analyze the complete device, which consists of a twisted region and two electrodes made of the ideal, non-twisted, semi-infinite wires. The PDOS of twisted wire by 10 deg between neighboring triangles is naturally 6-times "folded", because the lattice vector is 6 times larger in the wire's direction. In order to have a direct comparison between the electronic structure of twisted and non-twisted wires, the PDOS of the later one is obtained using a supercell containing 6 unitcells, as it is mandatory for the twisted wire. The band structures of the ideal and twisted wires are shown in **Figure 21** (a) and (b), respectively. The band structure calculated for one unitcell is given in **Figure 21** (c). The bands are marked with the corresponding labels according to their symmetry. For the twisted wire, as mentioned earlier, only  $a$ - and  $e$ -type bands are symmetrically determined.

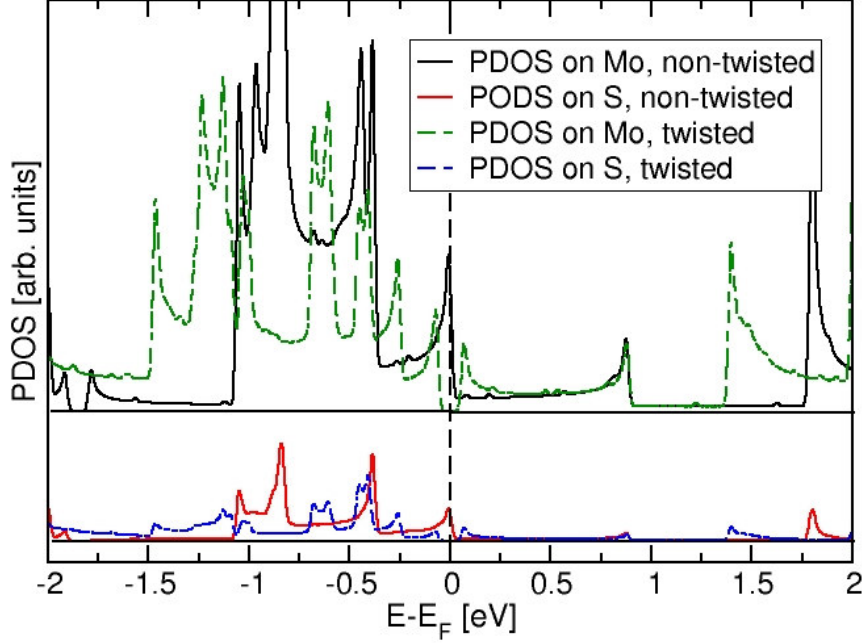


**Figure 20:** Projected density of states on Mo atoms (upper graph) and S atoms (lower graph) of the twisted wire by 10 deg between the neighboring alternating triangles, which corresponds to 45.87 deg/nm.

In **Figure 21** (b) the bands above Fermi level are denoted with  $C_{3v}$  labels, due to their small change with respect to the bands of the ideal wire. Only a small change of dispersion of these bands indicates that levels are not significantly affected upon twisting. In order to verify this statement further, in **Figure 22** the wavefunctions obtained in the  $\Gamma$ -point for certain energies above Fermi level are depicted. The wavefunction with  $a_1$  symmetry is composed of  $d_{z^2}$  atomic orbitals centered on the *Mo* atoms. Their “rings” obey a large overlap with each other, which yields a high delocalization of the wavefunction. The  $a_2$ -type state is composed of  $d_{x^2-y^2}$ -type atomic orbitals oriented orthogonal to the *Mo*-triangles. The form of the wavefunctions correspond well to ones obtained by Hughbanks and Hoffmann<sup>108</sup>. From **Figure 22** it can be noted that electronic states smoothly transform from their “perfect”  $a_1$ -, and  $a_2$ - type characters to their “approximate” correspondences. Dispersion of highest occupied and lowest unoccupied bands is very small, yielding two van-Hove singularities at

the edges of the band gap. This explains why the actual gap in the transmission function is somewhat wider than the band gap in the electronic structure; in the flat bands the group velocity of electrons is close to zero, i.e. the effective electron mass is large.

As mentioned above, the oscillations between Fermi level and 0.8 eV above Fermi level are not present due to the intrinsic change of the electronic properties of the nanowire

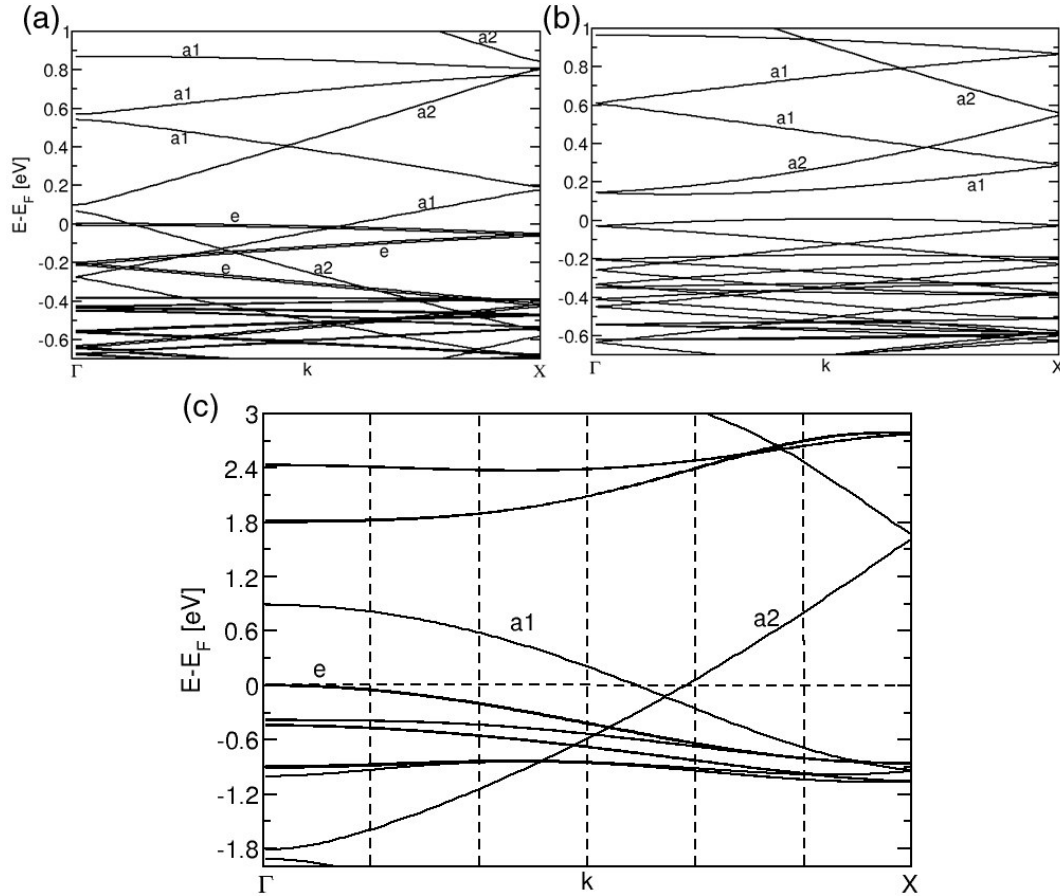


**Figure 21:** (a) Electronic band structure of the ideal nanowire (obtained for the supercell which contains 6 unitcells), (b) electronic band structure of the twisted nanowire by 10 degrees between neighboring triangles (6 unitcells in the supercell had to be included in order to obtain a smooth transition between original supercell and its periodic replica), (c) band structure of the ideal nanowire obtained for one unitcell. Dashed lines correspond to the  $k$ -points at which the band structure of (a) is folded. In (b) the  $a$  bands of the twisted wire are marked with  $a_1$  and  $a_2$  symbols in order to visually guide the reader to the correspondence to the bands of the ideal wire.

upon twisting. In the PDOS of twisted wire such oscillations do not exist. However, the  $a_1$ - and  $a_2$ - derived bands in the twisted wire are misaligned with respect to  $a_1$ -, and  $a_2$ -type bands in the electrodes that are made of the ideal wires. Therefore, the propagating electrons from/to electrodes to/from twisted region can reflect on the interfaces; otherwise they need to change the symmetry. In contrast to the states above Fermi level, electronic structure of the twisted wire is considerably affected upon twisting. The clear distinction between original  $a_1$ -, and  $a_2$ -type states vanishes. The states below Fermi level are mixtures of original states, i.e. both  $d_{z^2}$  -, and  $d_{x^2-y^2}$  - like atomic orbitals participate on the *Mo*-sites (see **Figure 23**).

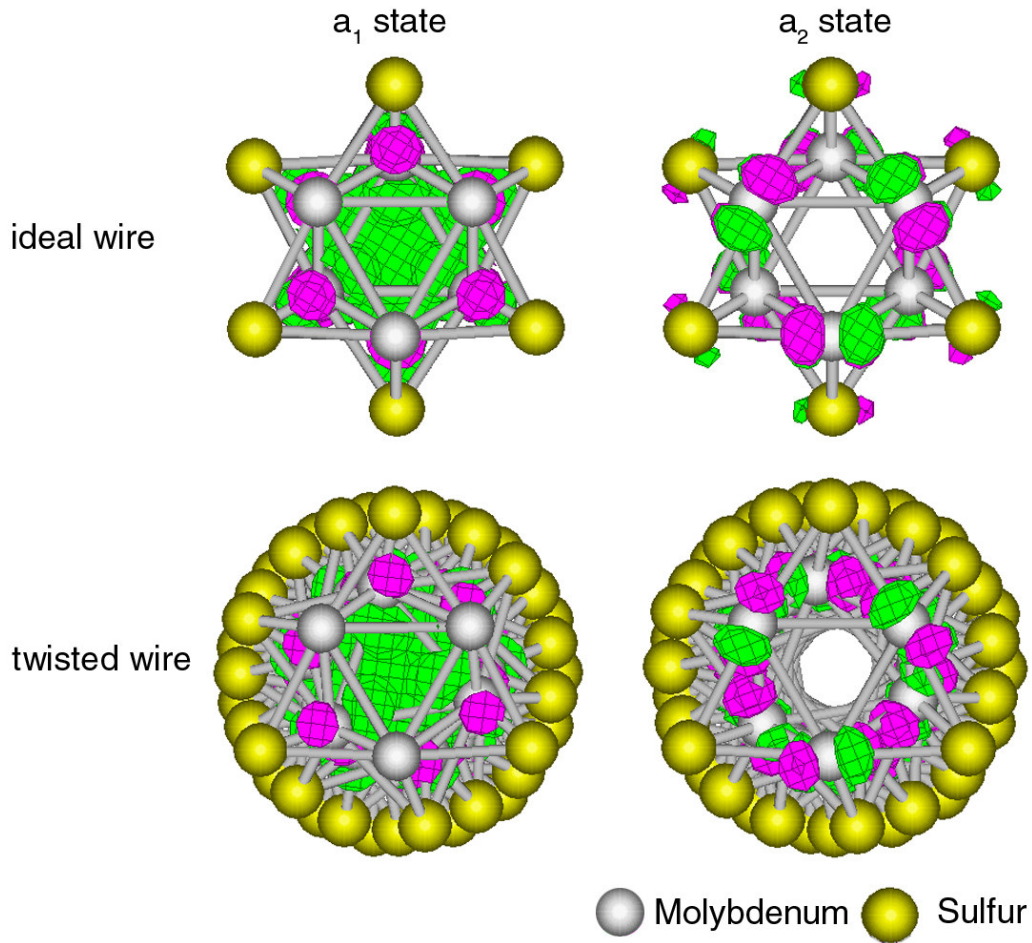


**Figure 22:** Wavefunctions of the  $a_1$ - and  $a_2$ -type states of the ideal nanowire (upper panel) and the corresponding states of the twisted by 10 deg. nanowire between neighboring *Mo*-triangles (lower panel).

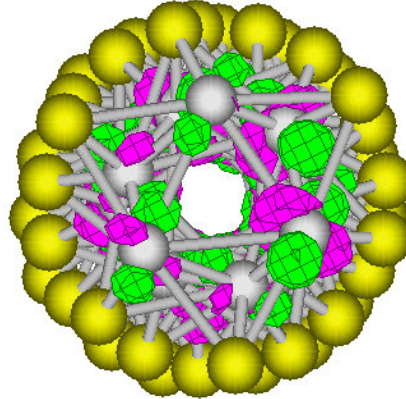


**Figure 23:** A characteristic state below Fermi level is a mixture of original  $a_1$ -, and  $a_2$ - type states, where both  $d_{z^2}$  -, and  $d_{x^2-y^2}$  - like atomic orbitals participate on the Mo-site.

In the ideal wire  $e$  band lies at Fermi level, whereas the first doubly-degenerate state of the twisted wire is shifted about 0.55 eV below Fermi level. The origin of the shift is in the energy of the crossing point of  $a_1$ -, and  $a_2$ -type bands of the ideal wire. The crossing point is around 0.14 eV under Fermi level, hence the  $a_1$  and  $a_2$  bands are partially filled by electrons above the crossing point (up to Fermi level). The “hybridization” of  $a_1$  and  $a_2$  states at crossing point results in the separation of the levels, when the mentioned electrons “settle” the new “hybridized” bands, which are now located above  $e$ -type band. Therefore, the doubly degenerate  $e$ -type band is effectively shifted lower with respect to Fermi level.

In contrast to CNTs, which conductance oscillates with the increase of the twisting angle <sup>22</sup>, the molybdenum sulfide NWs have the property of an unique unidirectional electromechanical *potentiometer*, as a consequence of their simpler atomic structure.

## 5.7 Conclusions

In conclusion of this chapter, the effects of mechanical deformations of  $Mo_6S_6$  nanowires on their structural, electronic, and transport properties were investigated. Two remarkable features have been presented in this chapter. First, a bending does not introduce any significant changes to the properties of the nanowire. This suggests the investigated metallic nanowires as flexible nanocables in future nanodevices. Second, the other type of

deformation, twisting, opens a band gap, which indicates that the wires have the potential to be used as a nanoscale *electromechanical switch* or a *potentiometer*. Thus, it is in principle possible to use all- $MoS_6$  systems in the future nanodevices.



## 6 Structural and electronic properties of $\text{Mo}_6\text{S}_8$ clusters deposited on a Au (111) surface

*Before proceeding to the research on the contacts between  $\text{Mo}_6\text{S}_6$  nanowires and Au electrodes, the binding between these two parts has to be analyzed. It is necessary to describe precisely the geometric structure of the wire-electrode interfaces, because the current injection through them strongly depends on the local geometry and electronic structure at the interfaces. In order to understand the connection between the systems investigated in this and the next chapter, where the contacts between  $\text{Mo}_6\text{S}_6$  nanowire and gold electrode will be analyzed, it is necessary to notice that  $\text{Mo}_6\text{S}_8$  cluster, with two sulfur atoms at opposite sides of the cluster removed, represents a unitcell of the  $\text{Mo}_6\text{S}_6$  nanowire. The contacting geometries that will be obtained in this chapter will be used as the contacting geometries for the  $\text{Mo}_6\text{S}_6$  wires connected to gold electrodes. It will be shown that electronic structure of the cluster and gold surface is changed only at the contacting atoms, whereas the other parts of the system are weakly affected. This indicates that much larger  $(\text{Mo}_6\text{S}_6)_n$  nanowires, as the structural extensions of  $\text{Mo}_6\text{S}_8$  cluster, bind to gold surface in the same way as  $\text{Mo}_6\text{S}_8$  clusters do, where only the contacting atoms contribute to the binding. This will be verified in next chapter. The stability of the ideal Au thin films is not fully understood yet, as it has been shown in the thesis on the basis of the different theoretical results; the instability is especially pronounced in the numerical calculations based on the DFTB method. With “full” DFT method the gold thin films seem to be stable<sup>130</sup>. Hence, in the present chapter the binding between  $\text{Mo}_6\text{S}_8$  cluster and Au (111) surface will be investigated using “full” DFT method employing the plane-wave basis set. The same method and the basis set was previously used for the research on binding of  $\text{Mo}_4\text{S}_6$  clusters to the gold surface<sup>130</sup>. Therefore, it is possible to directly compare the results for binding of  $\text{Mo}_6\text{S}_8$  and  $\text{Mo}_4\text{S}_6$  clusters on Au (111) surface, which will be also the subject of the present chapter. The detailed analysis includes not only the electronic and structural properties of  $\text{Mo}_6\text{S}_8$  clusters adsorbed on Au surface, but also an extensive research on the propensity for the self-organized growth of the molybdenum sulfide cluster  $\text{Mo}_6\text{S}_8$  on the Au (111) surface.*

## 6.1 Introduction

Depending on their size and composition molybdenum sulfide particles serve various key applications as solid lubricant<sup>131</sup>, electrode contact material<sup>132</sup>, or dehydrosulfurisation catalyst<sup>100</sup>. Bulk  $MoS_2$  is a semi-conducting lubricant of fairly low catalytic activity, which consists of weakly bonded units of sulfur-molybdenum-sulfur trilayers that can easily glide on each other<sup>133</sup>. However, the smallest units of  $MoS_2$  that remain stable when they are adsorbed onto gold are actually sulfur-deficient clusters with up to six  $Mo$  atoms, each containing a sulfur-decorated metalloid core<sup>130, 134</sup>. Such clusters are produced in a pulsed arc cluster ion source and exhibit pronounced peaks in the mass spectrum, which stem from  $Mo_4S_6$ ,  $Mo_6S_8$ ,  $Mo_9S_{11}$  etc. clusters. The stability and structural properties of these clusters have been investigated<sup>115, 135-138</sup>. Metal-supported molybdenum sulfide clusters are well-established desulfurization catalysts, e.g. for the production of ultra-low sulfur containing fuels<sup>139</sup>; hence recent theoretical studies have focused on the interaction of such clusters with small molecules like  $CO$  or  $H_2$ , and also with larger hydrocarbons and nitrogen-containing species<sup>140-145</sup>. With increasing sulfur content small clusters undergo a cluster-platelet transition to flat triangular nanoplatelets<sup>136</sup>. When supported on gold such platelets are excellent catalysts for the dehydrosulfurisation of fuels<sup>143, 145, 146</sup>; the atomistic and electronic factors of the reactivity have recently been revealed experimentally<sup>100, 140</sup>. In sulfur-rich platelet-shaped particles the interaction with the metal support can modify the catalytically active metallic edge state<sup>100, 146, 147</sup>, but leaves the sulfide cluster structurally intact. Theoretical and experimental investigations suggest that the flat platelets are stable under sulfur-rich preparation conditions for particle sized of up to 400-500 atoms. Larger particles exhibit three-dimensional structures up to 25000 atoms that assume a regular shape composed of nested octahedra, and still larger structures that grow into rounded inorganic fullerenes<sup>116, 148</sup> or even nanotubes<sup>79, 149</sup> or nanowires<sup>111</sup>.

For free clusters with more than three molybdenum atoms a cluster-platelet transition was found at a stoichiometry of  $Mo:S = 1:3$ , i.e. in the limit, when all molybdenum electrons are formally transferred to the sulfur sites, and no  $d$  electrons remain to make metallic  $Mo-Mo$  bonds. Both clusters investigated here,  $Mo_4S_6$  and  $Mo_6S_8$  are below this threshold and contain a metalloid  $Mo_4$  or  $Mo_6$  cluster core decorated by sulfur atoms. The most stable small cluster

is  $Mo_4S_6$  with a large energy gap of 0.8 eV<sup>115, 150</sup>, which suggests a weaker stability, but higher reactivity than  $Mo_4S_6$ . Comparable energy gaps of up to 0.6 eV have also been obtained from DFT calculations for small, Jahn-Teller distorted, pure molybdenum clusters<sup>151-153</sup> and indicate stability comparable to the one of  $Mo_6S_8$ . Major application of  $Mo_6S_8$  compounds is the use as a contact material in solid fuel cells, because the  $Mo_6S_8$ -based Chevrel phases may readily store or release lithium or magnesium ions<sup>132</sup>. Furthermore, the existence of network structures made of  $[Mo_{3n}S_{3n+1}]^{d-}$  cluster anions with *K*, *Cs*, and *In* counter ions<sup>154, 155</sup> indicates that the  $Mo_6S_8$  cluster may be at a negatively charged state.

The strong binding between sulfur and the noble metals gold and silver is widely used in basic and applied research, for linking the poorly reactive noble metal with polar materials, for instance for the integration of biochemical markers or the formation self-assembled monolayers based on functionalized thiol compounds<sup>156-162</sup>. Thus, the bonding between noble metal clusters or surfaces and thiol-substituted molecules has been investigated in great detail, including structural, electronic and conductivity properties<sup>163</sup>. Besides the above-mentioned ion storage capacity, the high reactivity of sulfur with noble metals makes  $Mo_6S_8$  electrode a good contact to the external metallic wiring, such that the molybdenum sulfide layer acts as an interface-active species, which enhances the wettability and the contact quality of the fuel cell interior by the wiring. Future applications may utilize this effect for generating structurally well-defined nano-contacts. However, it is desirable that the clusters can self-assemble on a *Au* (111) template to a uniform inorganic monolayer. Scanning tunneling microscopy images suggest an ordered growth of the sulfur rich nanoplatelets on the *Au* (111) surface<sup>100</sup>, which indicates a non-negligible cluster-support interaction. Likewise, calculations showed that the magic  $Mo_4S_6$  cluster is strongly bound on *Au* (111), and only internal structural relaxations are induced<sup>130</sup>. Recent experiments have demonstrated<sup>164</sup> that self-assembly may also be achieved with the small molybdenum sulfide cluster  $(Mo_3S_4)^{4+}$ . In this way, redox-active, purely inorganic monolayers on the noble metal can be formed. As the smaller cluster cation  $(Mo_3S_4)^{4+}$  indeed forms such redox-active inorganic monolayers on length scales of up to a micron<sup>164</sup>, the propensity of  $Mo_6S_8$  towards template-mediated self-assembly is also investigated in this chapter. Other recent experiments have revealed that even larger  $Mo_4S_6$ ,  $Mo_6S_8$ , and  $Mo_7S_{10}$  clusters may be successfully deposited on the *Au* (111) surface<sup>165</sup>. Calculations showed that the magic  $Mo_4S_6$  cluster is

strongly bound on  $Au$  (111) and only internal structural relaxations are induced<sup>130</sup>. This is not the case for small pure  $Mo_n$  clusters, which undergo significant atom rearrangements and have been observed to form thiol-selective, less reactive gold-covered core-shell particles by sulfur alloying<sup>166, 167</sup>. The theoretical understanding of the stability and the reactivity of the  $Mo_6S_8$  clusters upon deposition on metal surfaces is far from complete. In the present chapter are clarified these key issues in the formation of novel structured inorganic monolayers by the adsorption of the smaller  $Mo_mS_n$  clusters on the  $Au$  (111) surface.

The bottom line of the results is given as follows. The quasi-cubic  $Mo_6S_8$  cluster preferentially adsorbs via a face and remains structurally intact. It experiences a strong, mostly non-ionic attraction to the surface at several quasi-isoenergetic adsorption positions. A scan of the potential energy surface exhibits only small barriers between adjacent strong adsorption positions. Hence, the cluster may move in a potential well with degenerate local energy minima at room temperature. The analysis of the electronic structure reveals a negligible electron transfer and S-Au hybridised states, which indicate that the cluster-surface interaction is dominated by S-Au bonds, with minor contributions from the Mo atom in the surface vicinity. All results indicate that  $Mo_6S_8$  clusters on the  $Au$  (111) surface can undergo a template-mediated self-assembly to an ordered inorganic monolayer, which is still redox active and may be employed as surface-active agent in the integration of the noble metal and ionic or biological components within nano-devices. Therefore, a classical potential model was developed on the basis of the DFT data, which allows studying the larger cluster assemblies on the  $Au$  (111) surface. As already mentioned above, the gold surface is unstable within DFTB method, hence the classical potential model was employed.

## 6.2 Computational details

Density functional theory (DFT)<sup>43, 105</sup> has been used to determine all structural, energetic, and electronic properties. The ABINIT code<sup>168</sup> has been employed, which uses plain-wave basis to represent the valence states and norm-conserving pseudo potentials to

**Table 3:** Surface energy in electronvolts of 1x1x3 supercell for the gold surface with respect to (m, m,1) (m = 3 up to 12) k-point grid (rows) and the energy cutoff of the plane wave basis (columns).

	551.00eV	605.42eV	659.84eV	714.26eV	768.68eV	823.10eV
(3, 3, 1)	-0.73	-0.73	-0.74	-0.74	-0.74	-0.74
(4, 4, 1)	-0.49	-0.49	-0.49	-0.49	-0.49	-0.49
(5, 5, 1)	-0.64	-0.65	-0.65	-0.65	-0.65	-0.65
(6, 6, 1)	-0.62	-0.62	-0.62	-0.62	-0.62	-0.62
(7, 7, 1)	-0.59	-0.59	-0.59	-0.59	-0.59	-0.59
(8, 8, 1)	-0.60	-0.60	-0.60	-0.60	-0.60	-0.60
(10, 10, 1)	-0.60	-0.60	-0.60	-0.60	-0.60	-0.60
(12, 12, 1)	-0.60	-0.60	-0.60	-0.60	-0.60	-0.60

describe the core-valence interaction<sup>43, 105</sup>. A plane wave basis set and norm-conserving Troullier-Martins pseudopotentials at the local density<sup>61</sup> and generalized gradient approximation (Becke-Perdew)<sup>54</sup> levels were chosen. In detail, Troullier-Martins-type pseudopotentials for the configurations [Kr]5s25p0.54d3.5 of *Mo*, [Ne]3s23p3.53d0.5 of *S*, and [Xe]6s1.755d9.756p0.5 of *Au* were employed.

The convergence of the *k*-point grid and the cutoff energy for the plane wave basis were tested for the surface energy of the substrate, the pure *Au* (111) surface with 1 x 1 x 3 gold atoms in the supercell. The value is converged for a (8,8,1) Monkhorst-Pack type *k*-point mesh and an energy cutoff of 550 eV. Hence, a (2,2,1) Monkhorst-Pack type *k*-point mesh is used for the calculations with supercells, which consist of 4 x 4 x 3 gold slab. To verify the “completeness” of the *k*-point mesh for the supercell, the calculations on certain final structures with the slab and deposited cluster were repeated with denser *k*-point samplings, but the same results were obtained. Therefore, the (2,2,1) *k*-point mesh is used for all further calculations. The  $\Gamma$ -point approximation has been employed during the preoptimization of the model structures, and also for scanning the energy surface for the cluster-substrate interaction. The structures were optimized in a two-step procedure, employing the local density approximation<sup>61</sup>, and a refinement was carried out at the generalized gradient approximation (Becke-Perdew)<sup>54</sup> level. The maximum force per atom in optimized structures was  $5 \cdot 10^{-4}$  Ha/Bohr atom. Upon cluster adsorption, the relaxation of the *Au* (111) surface was restricted to the first layer, in order to simulate a semi-infinite surface.

Atomic charges were calculated by the Bader technique<sup>169</sup>. In order to obtain a local, chemical representation of the electronic interactions, total and projected density of states (PDOS) curves were analyzed within the density functional tight binding (DFTB) method<sup>63, 114</sup>. The forms of the total DOS obtained in local (DFTB) and plane wave (Abinit) basis set match very well (see **Figure 30**), which justifies the use of a local basis for projecting of the DOS. For better pictorial representation, the densities of electronic states are *a posteriori* broadened by convolution with Gaussian functions of 0.5 eV width at half maximum.

### 6.3 Geometries

As the band-structure approach is based on the three-dimensionally periodic boundary conditions, a repeated-slab supercell had to be employed. The supercell is composed of 48 gold atoms, 16 per layer, and the  $Mo_6S_8$  cluster on top of the surface, as it is presented in **Figure 24** (a). The lengths of the hexagonal supercell lattice vectors are 11.54 Å in plane, and 30.00 Å in the direction orthogonal to the gold surface. The z-axis is aligned perpendicular to the surface. Thus, the model represents an unreconstructed  $Au$  (111) surface, which is densely covered by the  $Mo_6S_8$  clusters with inter-cluster separations of 6.16 Å - 6.60 Å (shortest distances between atoms which belong to two neighboring clusters) and separated from the periodic replica along the surface normal by a vacuum region of more than 15 Å. The centers of neighboring clusters are spaced by 8.64 Å. During optimization of the free cluster its initial  $O_h$  symmetry is lowered to near  $D_{2h}$  due to a Jahn-Teller distortion. The  $\sigma_h$  plane is defined by atoms 7, 10, and 13, and  $\sigma_v$  by the atoms 2, 3 and 4. The  $C_2$  rotation axis penetrates the bond centers between the molybdenum atoms 2 to 3 and 4 to 6. This pre-optimized cluster is placed at high-symmetry sites of the ideal gold surface with a cubic lattice constant of 4.08 Å (**Figure 24** (b)). The position of the cluster on the high-symmetry points of the surface is denoted with respect to the cluster atom, which is the closest to the surface.

The following four high-symmetry positions were investigated (**Figure 24** (b)):

- *on-top* of the gold atoms,
- at the *bridge position* between two neighboring gold atoms,
- and at the *hollow* sites coordinated by three gold atoms.

For the latter position the distinction is made between

- *hollow site 1*, which is the hcp site with one gold atom below the adsorption site in the subsurface gold layer,
- and *hollow site 2*, which is the fcc site, where the adsorbed atom continues the ABC stacking sequence of the face-centered-cubic gold bulk.

*At each position, two orientations of the cluster with respect to the surface were investigated:*

- In the *tip* orientation, the cluster bonds via a sulfur atom at the corner of the  $Mo_6S_8$  cluster, and the space diagonal of the cluster is orthogonal to the surface;
- In the *square* orientation the cluster adsorbs via a face of the  $Mo_6S_8$  cube, such that one molybdenum atom and four sulfur atoms are situated in a plane parallel to the surface.

For the *square* orientation the adsorption position is given with respect to the central molybdenum atom, whereas the surrounding four sulfur atoms must occupy different sites due to the incommensurability of the cubic cluster structure and the hexagonal atom arrangement of the  $Au$  (111) surface. Thus, the *square bridge* position of the molybdenum places two sulfur atoms on top, and the other two close to bridge sites. For the *square hollow* position, the sulfur atoms are slightly shifted away from the hollow sites. For the *square on-top* position two sulfur atoms occupy bridge sites and the other two sulfur atoms are slightly shifted from on-top sites towards the hollow sites. These site, position, and orientation definitions will be used in the following sections.

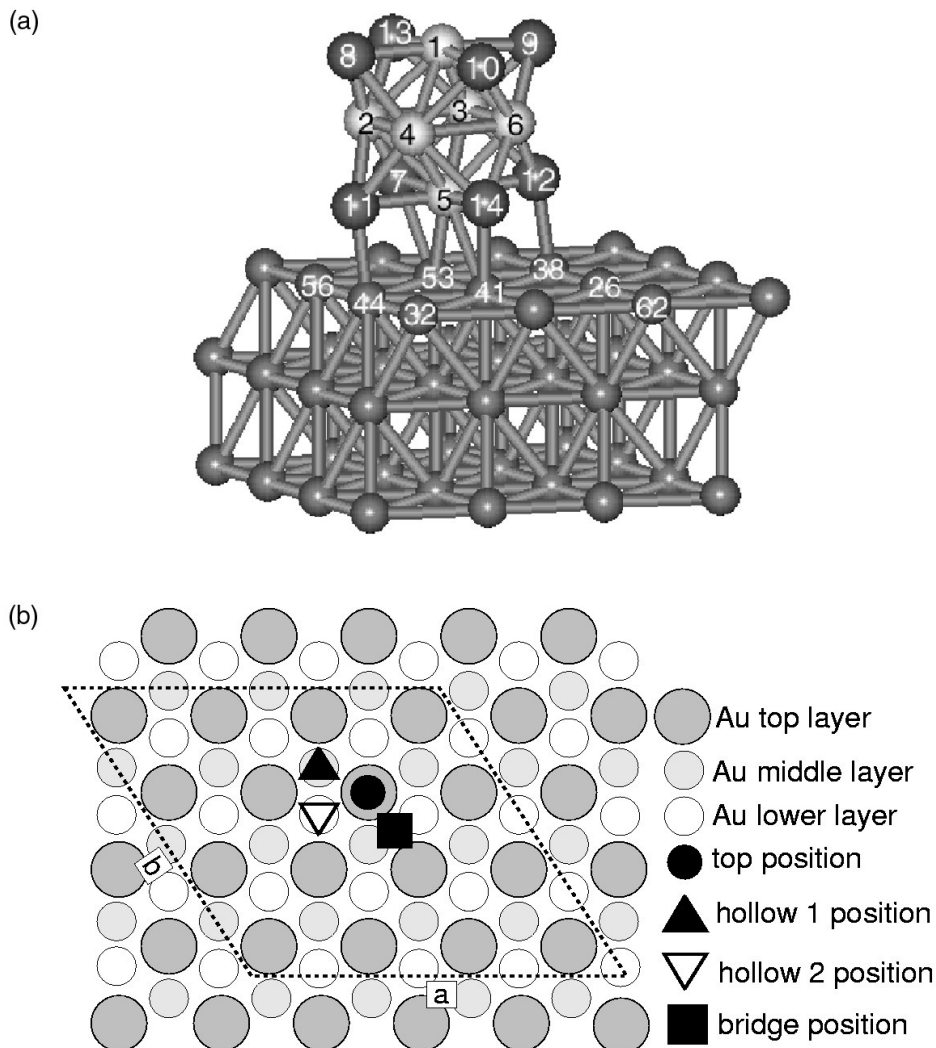


**Figure 24:** (a) The atom labeling of the cluster and the contact atoms on the surface for *square bridge* position. (b) Schematic representation of the supercell geometry. The investigated high-symmetry adsorption sites on the *Au* (111) surface are indicated.

## 6.4 Structural properties

In order to assess the influence of the adsorption on the structural properties, a two-step optimization was carried out: first, the cluster-surface distance was varied with cluster and surface fixed to the equilibrium geometry of the free fragments (see **Figure 26**), and



second, the geometries of the adsorbed cluster and the surface gold layer were completely optimized. A free, unreconstructed  $Au$  (111) surface exhibits bulk-type bond lengths between all gold atoms. A free  $Mo_6S_8$  cluster consists of a roughly octahedral  $Mo_6$  metal core, whose eight faces are capped by sulfur atoms at distances of 2.47 to 2.52 Å. The  $Mo_6$  cluster core is Jahn-Teller distorted to a squeezed octahedron, and the two apex atoms are slightly shifted off-center, such that five short  $Mo-Mo$  bonds of about 2.60 Å and nine long bonds of about 2.70 Å are formed. As a consequence, the sulfur atoms form a distorted cube with edge lengths of about 3.40 and 3.60 Å. At fixed cluster and surface geometries, the following optimum values are obtained from the curves of  $E_{bind}$  as a function of the cluster-surface distance (**Figure 26**): 2.30-2.60 Å for the *square*-oriented clusters and 1.80-2.00 Å for the *tip*-oriented ones with the exception of the *tip on-top* position, whose distance amounts to 2.40 Å. After full optimization the cluster-surface distance shrinks further by another 0.1 Å, and both fragments undergo distortions. The optimized distances between the lower sulfur and molybdenum atoms and their first gold neighbors are given in **Table 4**, whereas **Figure 25** displays the cluster-induced shifts of the gold atoms underneath the cluster with respect to their positions in the free surface.

First, the most stable adsorption geometries, the *square* arrangements, are discussed. The most preferred *square bridge* adsorption position exhibits an equilibrium cluster-surface distance of 2.27 Å, such that the two  $Mo-Au$  bonds as well as two of the four  $S-Au$  bonds assume lengths, which are very close to the respective sums of the covalent radii  $r_c(Mo) = 1.36$  Å,  $r_c(S) = 1.02$  Å, and  $r_c(Au) = 1.44$  Å<sup>170</sup>. The cluster-surface interaction is accompanied by structural changes in both fragments. A lateral in-plane relaxation elongates the bond between the two  $Mo$ -bridged gold atoms by more than 0.2 Å with respect to the free surface. The two sulfur atoms, which coordinate to the  $Au$  surface at on-top sites, induce an outward relaxation of the gold atoms by 0.08 Å. The Jahn-Teller distortion of the cluster is diminished; all  $Mo-Mo$  distances are elongated to values between 2.70 and 2.74 Å, and accordingly, also the S-S distances become more uniform. In order to match the on-top and bridge sites of the  $Au$  (111) surface, the sulfur atoms of the lower layer form a square with S-S distances of about 3.60 Å, whereas the unbound sulfur atoms at the cluster top relax inwards to a square of about 3.50 Å edge length. Thus, the cluster symmetry is close to  $C_{4v}$  with the four-fold rotation axis parallel to the surface normal. These asymmetric relaxations

indicate, that the bonding within the  $Mo_6S_8$  cluster is slightly weakened especially in the lower cluster part, which is closer to the  $Au$  (111) surface. The cluster is shifted towards the surface by around 0.13 Å during optimization.

For the low-symmetry *square hollow* positions the equilibrium distance between the cluster and surface amounts to 2.17 Å, which is again in good agreement with the sums of covalent radii for the  $Mo-Au$  bonds, but leads to a considerable elongation of the  $S-Au$  bonds by more than 0.1 Å even after optimization. The geometry changes in the cluster and gold surface layer are of the same character as for the *square bridge* adsorption position. At both *square-hollow* position the central molybdenum atom is located at the centre of the hollow site, and the  $Au$ -coordinated sulfur atoms exhibit shifts along the z-direction of 0.07-0.15 Å away from the surface and from the  $Au$ -coordinated molybdenum atom.

The *square on-top* position exhibits an unfavourably low  $Mo-Au$  distance of 2.624 Å, but still moderately to strongly elongated  $S-Au$  bonds. Due to the high-symmetry of the adsorption position, the shifts within the  $Au$  surface are negligible. For the cluster the relaxation pattern is comparable with the one of the other *square* positions: the lower triangle of molybdenum atoms is elongated to bond lengths of 2.75 - 2.79 Å, whereas the lengths of the upper triangle all amount to  $2.72 \pm 0.01$  Å.

**Table 4:** Optimized distances between  $S$  and  $Mo$  atoms and their first gold neighbors. The values in brackets correspond to  $S$  atoms on opposite sides with respect to the lower  $Mo$  atom 5.

Position	$Mo-Au$ (Å)	$S-Au$ (Å)
square on-top	2.62	(2.59;2.72),(2.98;3.14)
square hollow 1	2.84;2.84;2.83	(2.57;2.59),(2.70;2.81)
square hollow 2	2.82;2.83;2.84	(2.59;2.57),(2.71;2.81)
square bridge	2.78;2.81	(2.48;2.49),(2.69;2.75)
tip on-top		2.39
tip hollow 1		2.50;2.52;2.51
tip hollow 2		2.53;2.48;2.51
tip bridge		2.50;2.49

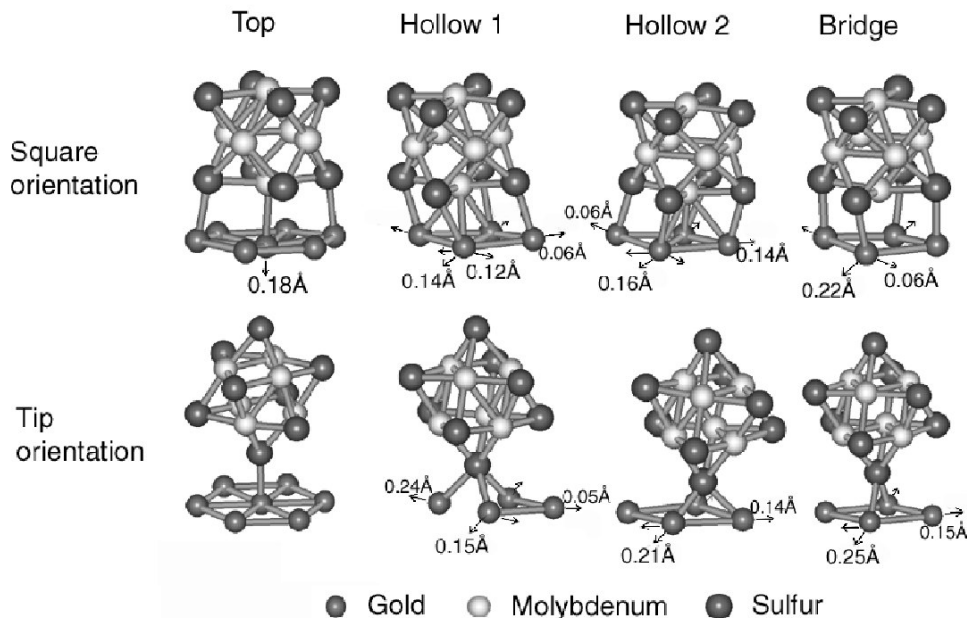


**Figure 25:** The influence of the adsorbate-surface interaction on the geometry of the substrate is indicated by the shifts of the *Au* atoms underneath the cluster with respect to their positions in the free surface (in angstroms).

For the *tip* orientation shorter cluster-surface distances are obtained, however the adsorption induced structure changes of the two fragments are lower than for the *square* orientation. The cluster assumes a symmetry very close to  $C_{3v}$ , which matches the symmetry of the surface. As for the *square* positions, the cluster atoms closer to the surface exhibit larger interatomic distances than the ones pointing away from the surface. This indicates that also in the *tip* orientation the bonding within the cluster is slightly weakened by the interaction with the gold surface, but a Jahn-Teller distortion remains.

At the *tip on-top* position only those sulfur atoms shifted, which are second nearest neighbors to the surface. With 2.386 Å the *S-Au* distance is, however, shorter than the sum of the covalent radii. In the *tip hollow* position the gold atoms coordinated to the sulfur atom of the cluster relax away from each other and towards the cluster by 0.03-0.04 Å. Due to this relaxation, the *S-Au* contact distances are also increased by 0.02-0.09 Å, although the cluster

moves towards the surface by about 0.06 Å upon optimization. For both adsorption positions the *S-Au* distances are close to the favourable range of 2.45 to 2.50 Å for the *S-Au* bond. Similar *S-Au* bond length values are also obtained for the *tip bridge* position, where the structural relaxation of the *Au* (111) surface at the bridge site is more pronounced than around the other adsorption sites.

## 6.5 Binding energies

The calculated binding energies are shown in **Table 5**. The cluster-surface binding energy is calculated as the difference between the total energy of the whole model structure and the values of the separate *MoS<sub>8</sub>* cluster and the *Au* (111) surface. In order to avoid numerical inaccuracies the separate fragments were calculated in the same supercell as the

**Table 5:** Comparison of the binding energies for *MoS<sub>8</sub>* at the different adsorption position of the *Au* (111) surface. In the second and third columns are the energies for the optimized cluster-surface distances prior to the full structural optimization at the LDA and GGA levels, respectively. The fourth and fifth columns list binding energies of the fully optimized structures, both at the LDA and the GGA level. The sixth column shows the difference of the binding energies between optimized and non-optimized structures at the LDA level as a measure of the correlation between structural relaxation and binding energy.

Position	LDA nopt. (eV)	GGA nopt.(eV)	LDA opt.(eV)	GGA opt.(eV)	E1 (eV)
square on-top	-2.81	-1.10	-3.54	-1.53	0.73
square hollow 1	-3.28	-0.98	-3.94	-1.46	0.66
square hollow 2	-3.29	-0.99	-3.97	-1.44	0.68
square bridge	-3.49	-1.32	-4.07	-1.69	0.58
tip on top	-0.97	-0.22	-1.44	-0.56	0.47
tip hollow 1	-1.27	0.13	-2.01	-0.55	0.74
tip hollow 2	-1.26	0.12	-2.09	-0.48	0.83
tip bridge	-1.20	-0.07	-1.80	-0.57	0.60

whole model structure. First, the dependence of the binding energy,  $E_{bind}$ , is investigated as a function of the distance between the cluster and the substrate. **Figure 26** shows the binding energies for the different adsorption sites as a function of the cluster-surface distance obtained from local-density-functional calculations with fixed atomic coordinates. Generally, the *square* orientations are by 2 eV more preferable than the *tip* ones for all positions. The difference in the binding energies between the least stable *square* and the most stable *tip* cluster orientation still amounts to 1.6 eV at the LDA level. Hence, the higher coordination number of the *square* arrangement is more favourable. The *square-bridge* position exhibits the strongest adsorption of all positions and cluster orientations. In this position, two sulfur atoms occupy on-top sites, and the other two are close to such a site. In comparison, the *square on-top* position is considerably less stable by 0.6 eV. Thus, the adsorption of the cluster on top of a gold atom via a direct molybdenum gold interaction is unfavourable for a good cluster-surface binding. This finding underlines the importance of the gold-surface interaction for the cluster-surface bonding. An adsorption of the cluster via the *tip* orientations is energetically favourable at the LDA level with binding energies of about 1.2 eV.

The structures corresponding to the minima of these curves were chosen as initial structures for a full structural optimization. After a full optimization of the adsorbed cluster and the first layer of the Au (111) surface the *square-bridge* position remains the most favourable one with a binding energy of  $E_{bind} = 4.07$  eV. At the *square hollow 1* and *square hollow 2* positions the cluster binds with 3.94 eV and 3.97 eV, respectively, the *on-top* position is again less favourable by about 0.6 eV. The two *hollow sites* are energetically degenerate, which suggests that the gold atoms of the sub-surface layer do not participate in the binding such that the interaction mechanism is confined to the gold surface layer. The difference between the binding energies of optimized *square*- and *tip*-oriented structures is in the range 1.45-2.63 eV, hence the adsorption via a face of the cluster remains the most stable arrangement after optimization. After refinement of these results at GGA level the binding energies are reduced by 0.75-2.53 eV and the potential energy landscape is less strongly corrugated. As the major findings are not changed by the GGA refinement, the LDA was employed for the more detailed structure investigations described below.

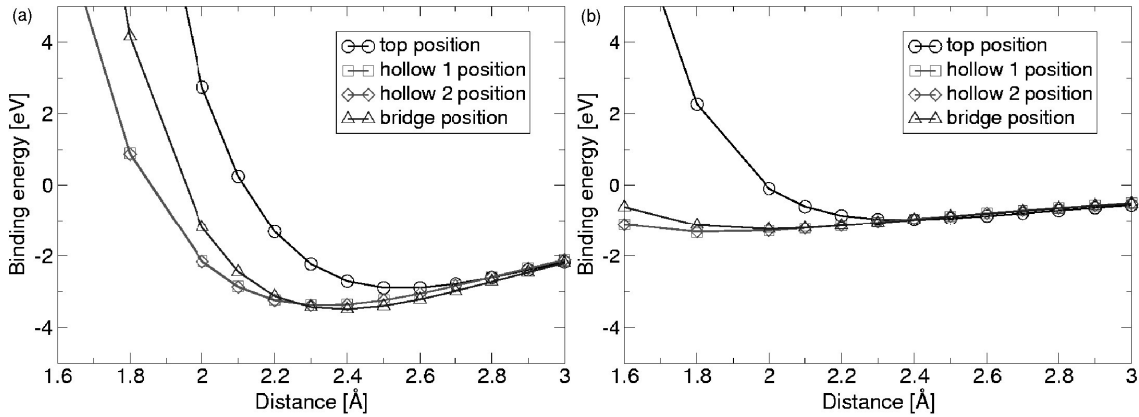


**Figure 26:** Binding energies for the adsorption of the unrelaxed  $Mo_6S_8$  cluster at the “square” (a) and “tip” orientation as a function of the cluster-surface distance (LDA,  $\Gamma$ -point approximation).

A comparison of the binding energies before geometry optimization, given in columns 2 and 3 of **Table 5**, and after optimization (columns 4 and 5) demonstrates the importance of the structural changes upon adsorption; e.g. the adsorption on *tip hollow site* positions is only favorable after further optimization. Thus, the geometry changes upon adsorption at the high-symmetry positions will be analyzed in the following.

## 6.6 Potential energy surface

The propensity for the formation of self-assembled monolayers may be investigated by calculating the potential hyper-surface, which constrains the free mobility of the cluster after deposition on the surface. In the following is assumed that the vibrational degrees of freedom may be neglected due to the strong cluster-surface interaction. From the remaining six rotational and translational degrees the vertical translation of the cluster along the surface normal has already been discussed above.

Two orientational degrees can transform the cluster from a *square*-oriented adsorption position to a *tip*-oriented one. As all *tip*-oriented adsorption sites are considerably less stable than the *square*-oriented ones such a geometry change is not very likely to occur, even at room temperature. Nevertheless, one such rotation from the *square* to the *tip* orientation has

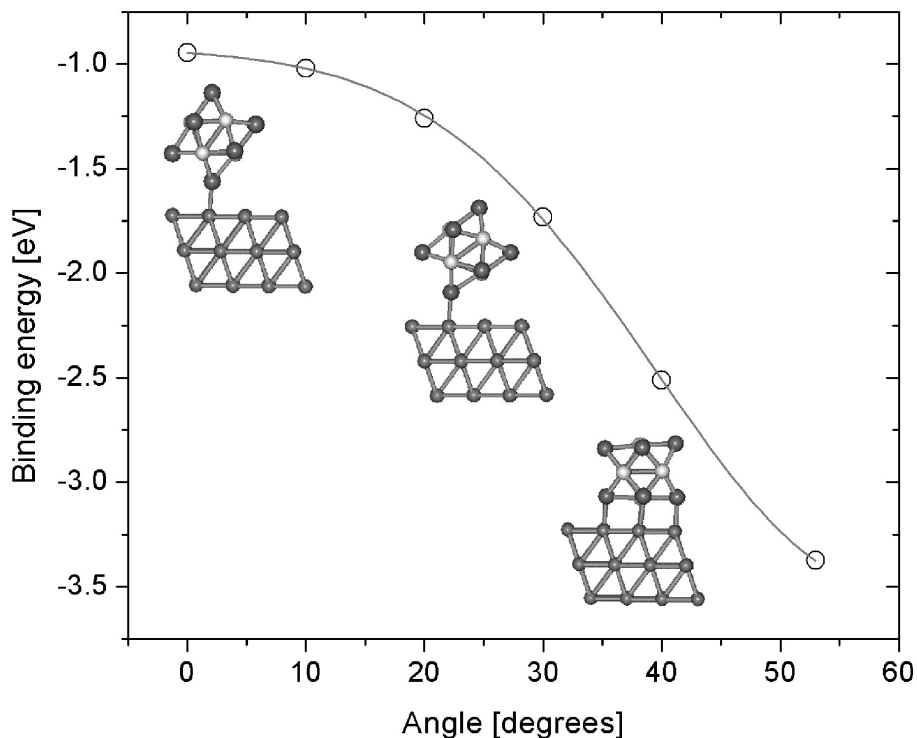


**Figure 27:** Binding energy of  $Mo_6S_8$  cluster on  $Au(111)$  surface as a function of the rotational angle for the transition from the *tip on top* to *square-bridge* position as depicted by the sketches of the adsorption geometry.

been examined, because there may exist additional metastable intermediates during the cluster deposition. By this transition the most unfavourable *tip on-top* position can be transformed into the most preferred *square bridge* position by rotating of the cluster as shown in **Figure 27**. From the initial *tip* orientation, the cluster is first rotated around the surface normal by 30 degrees, and then rotated into the *square-bridge* position around the lower sulfur atom. The obtained binding energy curve is given in **Figure 27** as a function of the tilt angle. The monotonous decrease of the slope shows that no intermediate adsorption geometries occur as stable local minima, but that the system strongly prefers the *square-oriented* adsorption on the bridge site.

Thus, from the six degrees of freedom, only three are relevant for the mobility of the cluster: the lateral translations parallel to the surface and the rotation around an axis parallel to the surface normal. The vertical translation, i.e. the cluster-surface distance, is chosen as linear interpolation between the respective optimized values at the high-symmetry position. The remaining four-dimensional potential surface was rastered in small steps using  $\Gamma$ -point calculations. At each lateral step the cluster was rotated around an axis parallel to the surface normal, which penetrates the centre of mass of the cluster. For a better graphical representation the dimensionality is restricted further and only the minimum energy for the optimum rotational angle is shown in **Figure 28** as a function of the position on the *Au* (111) surface, both as a contour plot and as a full three-dimensional surface.

The triangle at the bottom of the figure represents a part of the gold surface, with

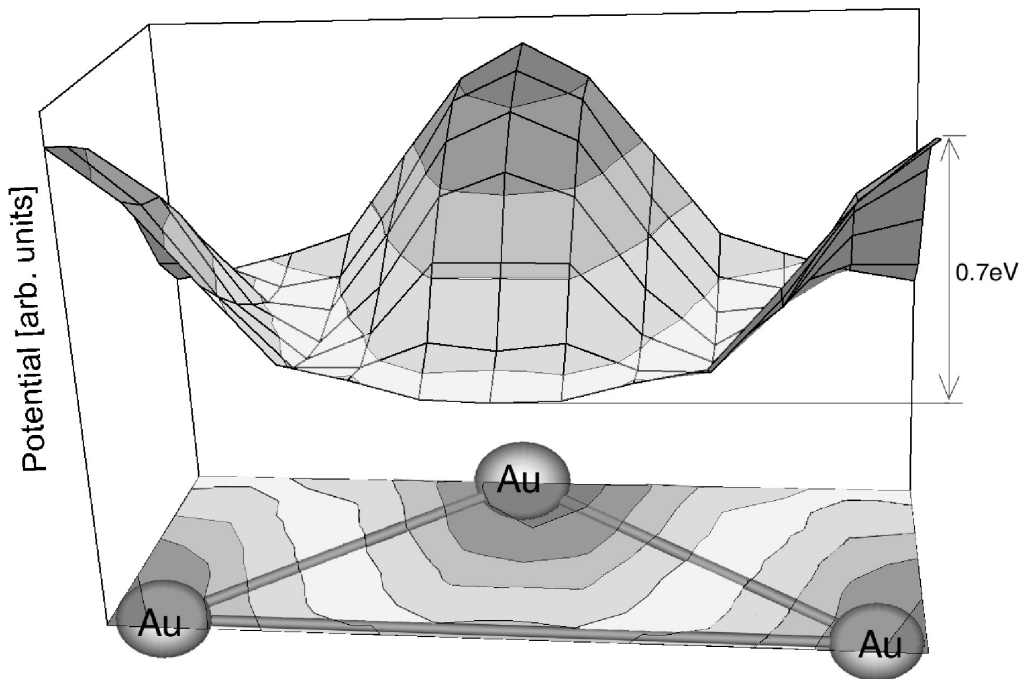


**Figure 28:** Potential energy surface for the lateral motion of  $Mo_6S_8$  cluster on *Au* (111) surface, both as three- and two-dimensional representation. The  $x$  and  $y$  coordinates specify the position of the central *Mo* atom with respect to the *Au* atoms of the surface, as drawn schematically in the lower part of the figure. At each position the rotation state with respect to the surface normal was optimized, and the cluster-surface distance was interpolated from the values at the nearest high-symmetry sites.



three gold atoms at the corners. The minima of the energy surface are located at the *bridge* positions, and maxima of 0.6 eV (LDA) or 0.2 eV (GGA) occur at the *on-top* positions. The trajectory between two neighbouring *bridge* positions crosses a relatively small (about 0.1 eV) potential barrier. Thus, at room temperature one can expect that the cluster can move from one *bridge* position to the neighbouring one across the *hollow site* position in-between, and that the cluster may dwell temporarily in these local minima. Due to the larger height of the *on-top* potential barrier the diffusion on the surface has mostly translational character around a surface normal, which penetrates the centre of mass of the cluster. The cluster remains *square* oriented, because the rolling motion of the cluster on the surface is energetically not favourable.

## 6.7 Classical model for the self-assembly

The propensity of  $Mo_6S_8$  clusters to form self-assembled layers must be discussed in comparison with recent experimental evidence for self-organized growth of redox-active inorganic monolayers from small sulfur-poor  $(Mo_3S_4)^{4+}$  clusters on the  $Au$  (111) surface<sup>164</sup>. The local adsorption geometry via three sulfur atoms at  $Au$ - $Au$  bridging sites suggested for  $(Mo_3S_4)^{4+}$  on the basis of conductivity and atomic force microscopy measurements is in very good agreement with previous results for  $Mo_4S_6$  cluster on  $Au$  (111) surface. As  $Mo_4S_6$  is structurally closely related to  $(Mo_3S_4)^{4+}$  by the exchange of the central  $\eta^3$ -bound sulfur atom with a  $MoS_3$  moiety, the experiment indicates that also  $Mo_4S_6$  may self-assemble to stable inorganic monolayers on the  $Au$  (111) surface. However, the large HOMO-LUMO gap (3 eV) of the  $Mo_4S_6$  cluster suggests expect only a low redox activity, thus  $Mo_4S_6$  may be more prominent as an inorganic template layer for the nano-structured integration of gold and biological components. The  $Mo_6S_8$  cluster investigated here has a smaller band gap of only 0.8 eV, hence regular  $Mo_6S_8$  monolayers might be better candidates for redox active inorganic layers such as nanoplatelets<sup>147</sup>. As the incommensurability of the cuboid  $Mo_6S_8$  cluster and the trigonal  $Au$  (111) surface makes most of the high-symmetry adsorption sites energetically degenerate. The small barriers in-between allow the cluster to move freely in a potential well, assuming different rotation states with respect to the surface normal. In this

**Table 6:** Fit parameters of the Gupta potential:  $A$  and  $B$  (Ha),  $p$  and  $q$  (dimensionless) as determined for the six pair potentials from fits to DFT reference structures.

	$V(Mo-Mo)$	$V(S-S)$	$V(Mo-S)$	$V(Mo-Au)$	$V(S-Au)$	$V(Au-Au)$
$A$	4.474	0.517	0.124	0.004	1.493	0.551
$B$	4.680	0.779	0.394	0.016	1.505	0.638
$p$	4.479	5.411	7.061	9.252	5.431	5.635
$q$	4.288	3.842	2.216	2.683	5.393	4.850

way, the adsorbed  $Mo_6S_8$  clusters are more free to rearrange to a structurally uniform monolayer than the trigonal  $Mo_4S_6$  clusters.

Less regular assemblies of molybdenum sulfide nanoparticles on the gold surface require too large supercell for a routine treatment at the full density-functional level. Furthermore, a Bader analysis of the electron redistribution upon cluster adsorption shows that no net charge transfer occurs between cluster and surface. Within the  $Mo_6S_8$  cluster only small Bader partial charges of up to 0.14 electrons are obtained and these partial charges induce smaller, even negligible image charges in the first surface layer of the  $Au$  slab. Hence, the interactions within the system may be re-expressed in terms of classical two-centre and three-centre contributions.

Gold nanostructures have been successfully modeled by Gupta-type potentials with a repulsive short-range term  $V_{rep}$  and an attractive term  $V_{attr}$  at intermediate range:

$$V_c = \sum_{i=1}^N [V_{rep}(r_{ij}) - V_{attr}(r_{ij})]$$

where

$$V_{rep}(r_{ij}) = \sum_{j=1; j \neq i}^N \left[ A \exp \left( -p \left( \frac{r_{ij}}{r_0} - 1 \right) \right) \right]$$

and

$$V_{attr}(r_{ij}) = \sqrt{\sum_{j=1; j \neq i}^N \left[ B^2 \exp \left( -2q \left( \frac{r_{ij}}{r_0} - 1 \right) \right) \right]}$$

The potential minimum  $V_{min}$  is numerically defined as  $V_{min} = |B| - |A|$  and is located at the optimum inter-atomic distance  $r_0$ .

$A$ ,  $B$ ,  $p$ , and  $q$  are fitting parameters, which have to be determined for each atom combination. In order to describe the cluster-surface interaction, the six interatomic potentials  $V(Mo-Mo)$ ,  $V(S-S)$ ,  $V(Au-Au)$ ,  $V(Mo-S)$ ,  $V(Mo-Au)$ , and  $V(Au-S)$  were generated. The fitting was performed with respect to potential energy curves calculated by DFT for small reference structures like the dimers, trimers and tetramers. For the  $Au-Au$  interaction potential also the data of DFT slab calculations were included in the database for the fit. The bond-specific values for the parameters  $A$ ,  $B$ ,  $p$ , and  $q$  are listed in **Table 6**. A Fermi-type cutoff function was used to smoothly confine the interatomic interactions within the nearest neighbour sphere, thus, the  $V(S-S)$  pair potential does not contribute to the cluster-surface interaction.

With binding energies of  $-3.47$  eV for the *bridge* position,  $-3.17$  eV for the *hollow* site positions and  $-2.84$  eV for the *on-top* position the description of the interaction by classical potential reproduces very well the binding energies for the unrelaxed cluster calculated at the LDA level ( $-2.74$  to  $-3.47$  eV). The calculated cluster-surface distances at DFT-optimized high-symmetry positions were included in the data set for the parameter optimization of the Gupta potentials, hence, the cluster surface distances of the most stable positions are reproduced by the classical potentials.

The analysis of the potential energy hypersurface focuses on the lateral translation state at the optimum rotation angle  $\phi$  around the surface between adjacent minima. However, the low-energy transition path between two such minima also involves a rotation around the angle  $\phi$ , which must not be neglected when studying the motion of a  $Mo_6S_8$  cluster on the  $Au$  (111) surface. Thus the potential energy surface as a function of the lateral cluster motion on the  $Au$  (111) surface has been complemented by the corresponding angle distribution plot. **Figure 29** provides this information: panel (a) shows the binding energy landscape as obtained from the full DFT treatment of a regular monolayer of  $Mo_6S_8$  clusters as described above; panel (b) displays the corresponding binding energy calculated with the model potentials for

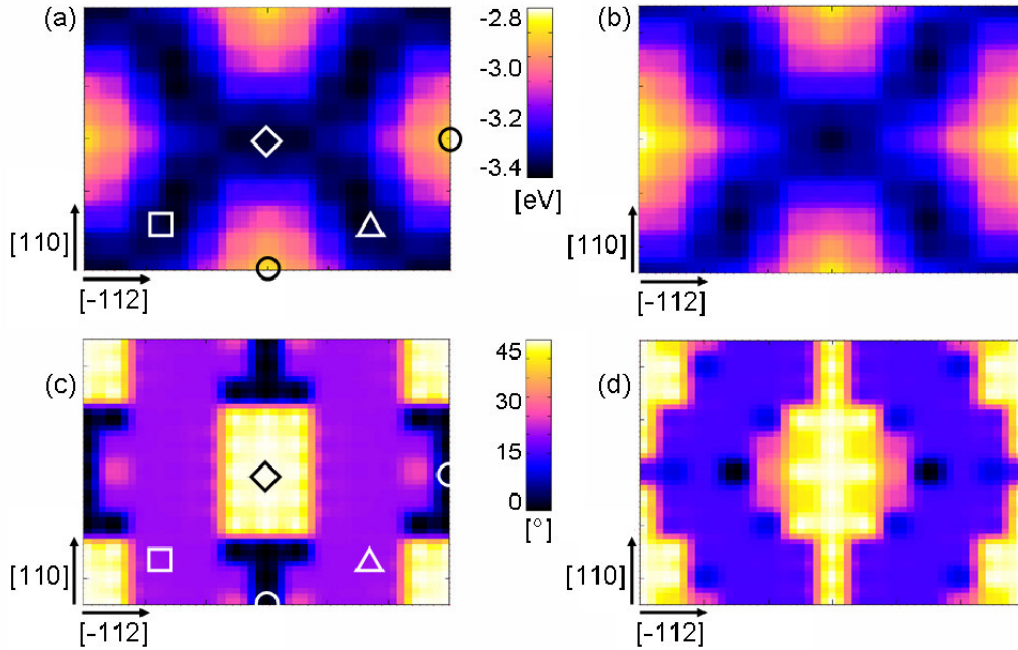


**Figure 29:** Comparison of the potential energy surfaces calculated by full DFT (left panels) and with the classical model potentials (right panels). Panels (a) and (b) give the binding energy as a function of the position of the cluster on the surface, panels (c) and (d) give the corresponding rotation angle  $\phi$  of the square around an axis parallel to the surface normal. For  $\phi = 0$  two edges of the square are parallel to the  $\langle 111 \rangle$  direction.

a single  $Mo_6S_8$  cluster on the  $Au$  (111) surface. The lower part of **Figure 29** gives the corresponding angle distributions for the rotation of the cluster around the axis parallel to the surface normal, in (c) for the full DFT, in (d) for the classical modeling. For  $\phi = 0$  two edges of the square are parallel to a  $\langle 111 \rangle$  direction of the surface.

The comparison yields two major results of importance for the description of the self-assembly process. First, the extrema and the saddle points of the potential energy surfaces (a) and (b) are in very good agreement, although the saddle point geometries and energies were not included in the data used for the potential fitting. Hence, the thermodynamics of the cluster adsorption is well represented in the classical picture. Differences between the plots (a) and (b) occur in the close vicinity of the minima, where the classical modeling overestimates the curvature and pins the cluster more strongly to the optimum positions. This

deviation is not crucial, because the cluster deposition and self-assembly dynamics of interest here is a high-temperature process dominated by the translational and rotational motion of the cluster. Only the low-temperature dynamics of localized clusters would be dominated by the vibrational degrees of freedom, which were neglected in the classical model for the sake of simplicity.

Second, the angle distributions calculated by DFT (panel (c)) and by classical modeling (panel (d)) fully agree at the low-energy positions and exhibit an average deviation of only up to five degrees around the saddle points between those minima. Thus, the classical model reproduces the trajectory of the cluster inside the potential well of the surface almost quantitatively. The only pronounced deviation that occurs is for the rotation state at the most unfavourable *square on-top* position. As this global maximum is 0.7 eV higher than the global minimum and at least 0.3 eV higher than the highest transition state, this discrepancy will not play a role in modeling the coverage of Au (111) by  $Mo_6S_8$  clusters with classical potentials.

## 6.8 Electronic structure

An analysis of the electronic structure yields insight in the nature of the cluster-surface interaction, which determines the adsorption strength and the potential reactivity change upon adsorption. For  $Mo_6S_8$  on Au (111) two interaction mechanisms may play a role: an ionic attraction between the cluster ions and the induced image charges or charge transfer states in the gold surface and, second, the formation of directed covalent bonds. The ionic contribution was estimated with the help of the Bader charges enclosed in polyhedra bounded by zero-flux surfaces. **Table 7** displays the Bader charges for the atoms of the most stable *square bridge* arrangement, the free cluster and surface, and the corresponding differences. In the free cluster each molybdenum atom donates 0.09-0.14 electrons to sulfur, thus, nominally more than 5 electrons remain at each molybdenum atom to form the *Mo-Mo* bonds of the  $Mo_6$  cluster core. This strong, non-ionic bonding in the cluster core is essential for maintaining the structural integrity of the cluster. However, the low partial charges in the free cluster already suggest, that only very small image charges may be expected on the gold atoms, and that

changes of the Bader charges are more likely due to electron transfer processes. After deposition, the largest charge transfer occurs at the sulfur atoms close to the surface, which lose 0.05 electrons each, whereas the other sulfur atoms as well as the molybdenum atoms have negligible charge difference. After the deposition the cluster remains neutral with a negligible electron loss of 0.01 electrons totally. As the charge transfer after the deposition is negligibly small, no significant ionic contribution to the cluster-surface interaction is expected.

The covalent character of the cluster-surface interaction was investigated with the help of site (and angular-momentum) projections of the density of electronic states. In addition to the plane-wave DFT calculations presented so far, the density of states was also computed with the density-functional-based tight-binding method (DFTB), which employs a minimal atomic orbital basis set. In the latter approach the site- and angular-momentum specific projection of the density of electronic states on the basis functions provides chemical insight into the interaction mechanism between the cluster and the surface. Furthermore, an inspection of the highly unspherical Bader polyhedra (not shown here) explains that a standard projection of DOS on spherical harmonics within atomic spheres will fail to catch all relevant features. The atomic orbitals basis set, on the contrary, adapts to the anisotropy and allows for a lossless decomposition of DOS onto atomic sites. Total DOS obtained by the two approaches (see **Figure 30**) for the most stable *square bridge* position coincide quite well, hence the DFTB method was employed for the further site-specific analysis. Two sulfur 3s peaks occur at around -13 eV, whereas the DOS curve of the free cluster exhibits only one peak. This splitting is a consequence of the symmetry reduction, which the cluster experiences due to the adsorption via only four of its eight sulfur atoms. At less negative binding energies there are the valence bands which originate from sulfur 3p, molybdenum 4d and 5s levels, and gold 5d and 6s levels. As they provide the cluster-surface bonding, this part of DOS will be investigated in more detail in the following.

The site-projected partial DOS curves (PDOS) for the contacted gold surface atoms (a), for the molybdenum (b) and sulfur (c) atoms of the cluster are shown in **Figure 31**. The dashed lines correspond to PDOS of the free cluster and the surface, and the solid line shows

**Table 7:** Bader charges on atoms in the free cluster and surface (column 2), in the optimized *square bridge* position (column 3), and their difference. The numbering of the atoms corresponds to **Figure 24** (a).

Atom number	atomic charges in free components (eV)	atomic charges upon deposition (eV)	difference (eV)
1	0.91	0.91	0.00
2	0.91	0.87	0.04
3	0.90	0.87	0.03
4	0.91	0.88	0.03
5	0.86	0.87	-0.01
6	0.87	0.87	0.00
7	-0.67	-0.63	-0.04
8	-0.67	-0.67	0.00
9	-0.67	-0.67	0.00
10	-0.67	-0.67	0.00
11	-0.67	-0.62	-0.05
12	-0.67	-0.62	-0.05
13	-0.66	-0.67	0.01
14	-0.67	-0.62	-0.05
15	-0.02	-0.02	0.00
16	0.05	0.04	0.01
26	-0.02	-0.02	0.00
32	-0.02	-0.02	0.00
38	-0.02	0.02	-0.04
41	-0.02	-0.07	0.05
44	-0.02	0.02	-0.04
52	0.05	0.03	0.02
53	-0.02	-0.09	0.07
55	0.05	0.03	0.02
56	-0.02	-0.01	-0.01

the PDOS curves for the cluster on the *square bridge* position; only the valence band energy region is included in the graphs.

For the atoms of the free Au (111) surface, a parabola-shaped s-electron PDOS is overlayed by the more localized d states with maxima at -5.8 eV, -4.5 eV, -4.0 eV, -3.0 eV, and -2.1 eV, and shoulders at -6.7 eV and -1.4 eV (see **Figure 31** (a), dashed lines). Except for

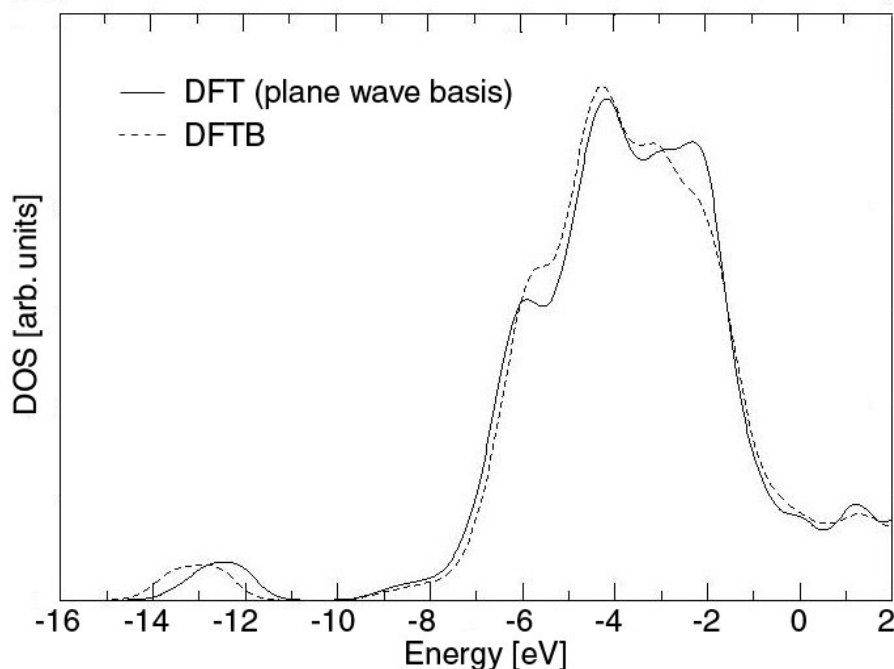


**Figure 30:** Comparison of DOSs of the most stable *square bridge* position calculated with DFT with plane wave basis and density-functional-based tight binding method. Fermi level is set to zero.

the shoulder at -1.4 eV, all other peaks are influenced by the adsorption of the cluster and the concomitant surface relaxation (solid lines). All states are shifted by -0.2 eV on average, i.e. to more negative energies; states below -4.5 eV gain in intensity, states above that threshold are reduced. The changes are most pronounced at those gold atoms (41 and 53), which are bridged by the molybdenum atom of the cluster, and which experience the largest in-plane relaxations.

The PDOS curves of the free  $\text{Mo}_6\text{S}_8$  cluster exhibit Mo-d states from -5.1 eV up to the Fermi level (**Figure 31** (b), dashed lines), whereas S-p states range mainly from -5.1 eV to -2.0 eV (**Figure 31** (c), dashed lines). Hence Mo-S binding states may be found between -5.1 and -2.0 eV, whereas the states above -2.0 eV are Mo-Mo bonding and non-bonding states of the  $\text{Mo}_6$  cluster core as indicated in ref. <sup>136</sup> in the discussion of the cluster-platelet transition. An energy gap of 0.8 eV separates the occupied and non-occupied states. The states on either side of this gap are composed of Mo-d states. As seen in **Figure 31** (b) and (c)



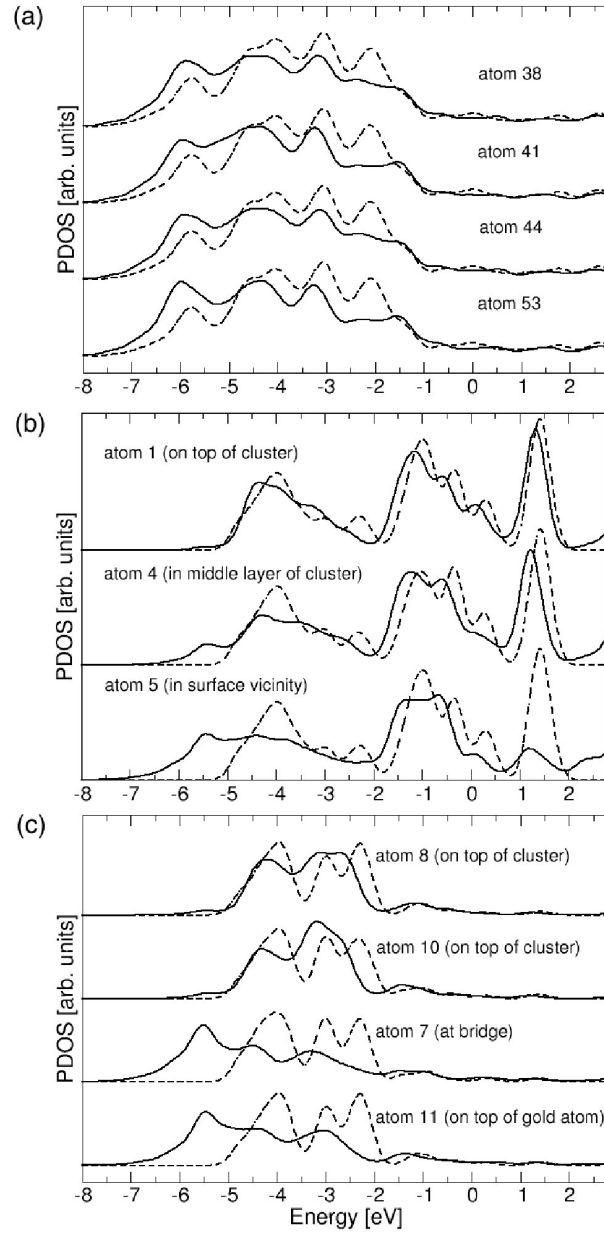


**Figure 31:** Partial densities of states projected on the (a) gold (b) molybdenum and (c) sulfur atoms (dashed line: free cluster and surface, solid line: deposited cluster on surface at *square bridge* position). The Fermi level is set to zero; the atom labeling is according to **Figure 24** (a).

two symmetry-inequivalent sites can be distinguished in the free cluster for both the molybdenum and the sulfur atoms due to the initially mentioned Jahn-Teller distortion. The

major difference between the two inequivalent Mo sites shows up for the *Mo-Mo* *d*-type bonding and non-bonding states, where the incomplete shell filling leads to different intensity patterns of the states around the Fermi level. The influence of the distortion on the *Mo-S* bonding states is much weaker, indicating that the *Mo-S* bonds of the free cluster are all equally stable. Adsorption of this cluster on the surface lifts the degeneracies further, because only the former  $\sigma_h$  symmetry element of the cluster is retained. Now, the cluster exhibits three non-equivalent molybdenum atoms and four non-equivalent sulfur atoms, and the PDOS curves for each symmetry type are displayed in **Figure 31** (b) and (c) by solid lines. The PDOS curves show that the influence of the surface on the cluster states decreases with increasing of height of the cluster atom above the surface. For the upper molybdenum apex atom (1) and the surrounding sulfur atoms (atoms 8 and 10 and their symmetry-equivalent partners) only the DOS intensity profile changes, but no major shifts and no additional peaks below the valence band of the free cluster occur. The splitting of the *Mo-S* bonding states is diminished as a consequence of the more uniform bond lengths within one layer of the adsorbed cluster, and a minor shift of the *Mo-Mo* bonding states by -0.2 eV is obtained. In contrast, the atoms in direct contact with the gold surface (atom 5 in **Figure 31** (b) and atoms 7 and 11 in (c)) are strongly influenced. Here, the shift of the *Mo-Mo* bonding states is accompanied by intensity changes, both the splitting and the absolute intensity of the *Mo-S* bonding states is reduced, and additional states occur just below the lower edge of the valence band between -7 and -4.5 eV. Thus, the cluster exhibits the same redistribution of the PDOS from states above -4.5 eV binding energy to new states below this threshold as the atoms of the gold surface do. This finding is a strong indicator for the formation of *Mo-Au* and *S-Au* bonding states at the expense of the *Mo-S* bonds, and, to a lower degree, also of the *Mo-Mo* bonds. Furthermore, it is fully consistent with the bond length changes discussed above. Finally, the molybdenum atoms of the middle layer of the cluster (atom 4 in **Figure 31** (b)) “experiences” an average situation and their PDOS can be interpreted as an overlay of the PDOS curves of the two apex molybdenum atoms.

## 6.9 Discussion and conclusions

The potential for practical applications of  $Mo_6S_8$  assemblies on  $Au$  (111) can be assessed by comparing these new results with established theoretical and experimental expertise on related small clusters and the substrate-mediated changes of their stability and reactivity upon adsorption. A quantitative comparison can be made with the adsorption of the exceptionally stable, magic  $Mo_4S_6$  cluster, which has been studied recently with identical computational settings; for other systems, the comparison is of a more qualitative nature. Concerning the stability of the cluster, the present investigation shows, that at the  $Mo:S$  ratio of 3:4 the central  $Mo_6$  cluster core is still sufficiently well passivated by the surrounding sulfur atoms to prevent the alloying with the  $Au$  (111) surface, reported by experiments on small  $Mo$  clusters on  $Au$  (111). Similar to the more sulfur-rich  $Mo_4S_6$  cluster,  $Mo_6S_8$  can also strongly adsorb on gold via a cluster face, since it provides a maximal number of  $Mo-Au$  and  $S-Au$  bonding interactions. In both clusters the  $Mo-Mo$  and  $Mo-S$  bond lengths in the vicinity of the surface are elongated by up to 0.3 Å, and the overall bond lengths equilibrate: Yet, both clusters exhibit no cluster-platelet transition upon adsorption, therefore the critical sulfur content for the transition to platelet shapes must be above the ratio of  $Mo:S = 3:4$  also for adsorbed clusters. Quantitatively, from these two clusters the  $Mo_4S_6$  cluster interacts three times stronger with the  $Au$  (111) surface, because  $Mo_4S_6$  possesses the same trigonal symmetry as  $Au$  (111), whereas the cuboid  $Mo_6S_8$  is incommensurate to it. Thus, the  $Mo-Au$  and  $S-Au$  distances are closer to their optimum values in case of the  $Mo_4S_6$  adsorption. Following the same reasoning, it may be expected that an  $Au$  (100) surface is better suited for the soft landing and stable adsorption of  $Mo_6S_8$  clusters.

Second, support-mediated reactivity changes of sulfur-rich, platelet-shaped molybdenum sulfide clusters have been reported experimentally and were related theoretically to the change of the electronic structure especially along the reactive edges<sup>100, 146, 147</sup>. The small, sulfur-poor  $Mo_4S_6$  and  $Mo_6S_8$  clusters do not show such a behavior, presumably because the corrugation of the electron density above the cluster occurs on a larger length scale<sup>100, 146, 147</sup>. As the electron transfer between cluster and surface as well as the more local changes of Bader-type atomic partial charges are negligible for both investigated small clusters, there are no ionic contributions from the cluster-surface bonding,

which could induce a change of the cluster reactivity. Quite on the contrary, the present PDOS analysis for  $Mo_6S_8$  on  $Au$  (111) and the fragment-resolved analysis of the DOS of  $Mo_4S_6$  on  $Au$  (Ref. <sup>130</sup>) both show that directed  $Mo-Au$  and  $S-Au$  bonding interactions occur at the expense of  $Mo-S$  and  $Mo-Mo$  bonding. For the larger cluster,  $Mo_6S_8$ , the concomitant changes of the electronic structure are, however, limited to the cluster face, which is in direct contact with the  $Au$  surface. The top surface exposed to potential reaction partners experiences only some minor modifications related to the change of the cluster geometry upon adsorption.

The local adsorption geometry via three sulfur atoms at  $Au-Au$ -bridging sites suggested <sup>164</sup> for  $(Mo_3S_4)^{4+}$  on the basis of conductivity and atomic force microscopy measurements is in very good agreement with data on the adsorbed  $Mo_4S_6$  cluster <sup>130</sup>. This is expected since  $Mo_4S_6$  is structurally closely related to  $(Mo_3S_4)^{4+}$  by the exchange of the central  $\eta^3$ -bound sulfur atom with a  $MoS_3$  moiety. Given the high interaction energy, such a  $Mo_4S_6$  layer can even be more long-term stable and better organized than the experimentally generated  $(Mo_3S_4)^{4+}$  layers. However, due to the large HOMO-LUMO gap (3 eV) of the  $Mo_4S_6$  cluster, a redox activity comparable with the  $(Mo_3S_4)^{4+}$  layer is not predicted. In contrast,  $Mo_6S_8$  has a smaller band gap of only 0.8 eV, hence  $Mo_6S_8$  monolayers are better candidates for basically neutral, but redox active inorganic layers. As discussed above the incommensurability of the cuboid  $Mo_6S_8$  cluster and the trigonal  $Au$  (111) makes most of the high-symmetry adsorption sites energetically degenerate. In this way, the adsorbed  $Mo_6S_8$  clusters have more degrees of freedom to rearrange to a structurally uniform monolayer than the trigonal  $Mo_4S_6$  clusters, which strongly bind to the three-fold hollow sites.

The potential energy surface of  $Mo_6S_8$  cluster deposited on  $Au$  (111) surface has an extended well of degenerate local minima, which are separated by energy barriers lower than 0.1 eV. A Bader analysis of the electronic structure revealed no net ionic contribution to the cluster-surface interaction. Thus, the cluster-surface interaction has been modeled successfully by classical pair potential of the Gupta type. Within the temperature range relevant for the deposition and assembly processes the potential energy hypersurface calculated with these classical potentials reflects all properties of the surface obtained from full DFT calculations.

The  $Mo_6S_8$  cluster exhibits all prerequisites as building block for the formation of stable, but still redox-active inorganic monolayers on a gold substrate. Apart from their electronic activity, such strongly bound, inorganic monolayers are very important interface-active agents, which enhance the wettability of the otherwise poorly wettable noble metal gold by ionic compounds or which provide a structured template for the ordered adsorption of biological substances.

Considering the  $Mo_6S_8$  cluster as the unitcell of the  $Mo_6S_6$  nanowires, which are the main subject of the thesis, two findings are of most importance. First, the cluster binds strongly with  $Au$  surface via  $S-Au$  bonds with some  $Mo-Au$  contribution. Second, the adsorption of the cluster on the surface affects only the cluster atoms that directly contribute to binding with the gold surface, leaving almost intact the atoms on top of the cluster. Since the electronic structures of the free  $Mo_6S_6$  nanowire and the free  $Mo_6S_8$  cluster are very similar around their Fermi energies, the electronic structure of  $Mo_6S_6$  nanowire is expected to change also in a similar way upon its bonding to the gold electrodes. This may have important effects on the electron transmission in  $Au - (Mo_6S_6)_n - Au$  geometry setup. In the following chapter the physics of such interfaces will be analyzed in detail.



## 7 Unique electronic and transport properties of contacts between $\text{Mo}_6\text{S}_6$ nanowires and gold electrodes

*Changes in the electronic and structural properties of  $\text{Mo}_6\text{S}_8$  clusters upon their deposition on Au (111) surface were analyzed in the previous chapter. It has been shown that their contact geometry is changed only at the very narrow region of the contacts. The electronic density of states projected on cluster atoms, which are not in direct contact to the gold surface is almost intact. The  $\text{Mo}_4\text{S}_6$  cluster obey the similar physics upon their deposition on Au (111) surface<sup>130</sup>. It should be noticed that  $\text{Mo}_6\text{S}_8$  cluster, without two opposite sulfur atoms (e.g. atom 8 and atom 12 in **Figure 24** (a)), represents a unitcell of an infinite  $\text{Mo}_6\text{S}_6$  nanowire, and electronic properties of  $\text{Mo}_6\text{S}_8$  cluster evolve in the asymptotic case into electronic structure of the infinite  $\text{Mo}_6\text{S}_6$  nanowire by extending the  $\text{Mo}_6\text{S}_8$  cluster with additional unitcells<sup>108</sup>. Real systems in physical and chemical laboratories are never infinite, hence only finite segments (i.e. clusters) of  $\text{Mo}_6\text{S}_6$  nanowires exist. In the following text the electronic and transport properties of contacts between the molybdenum sulfide nanowire and gold electrode will be discussed. The most stable geometry between  $\text{Mo}_6\text{S}_8$  cluster and Au (111) surface (see previous chapter) will be utilized as one type of the contacts between  $\text{Mo}_6\text{S}_6$  nanowires and gold electrodes. The relaxed geometry of the system consisting of  $\text{Mo}_4\text{S}_6$  cluster deposited on Au (111) surface will be utilized as another contact type. As it is already mentioned above, the changes in the electronic properties of these clusters upon their deposition on a gold surface is strongly localized only at contacting atoms of gold and the cluster; Hence it is reasonable to assume that contacting geometries of the  $\text{Mo}_6\text{S}_6$  nanowires (finite clusters) and gold electrodes match well with the contacting geometries of  $\text{Mo}_6\text{S}_8$  and  $\text{Mo}_4\text{S}_6$  clusters on the gold surface. It will be shown that electric current can be easily injected through the contacts. “Observed” high transparency of the contacts for the charge carrier injection is the consequence of a “task sharing” between sulfur and molybdenum atoms at the interface with the gold electrode, where sulfur binds the nanowire to the electrode, and the current flows unperturbed through the direct Au-Mo channels. The unique structural, electronic, and transport properties of the contacts may solve*

*the major drawbacks of the usual contacts in the molecular electronics devices and nanotechnology, like the weak physical bonding between carbon nanotubes and electrodes, as well as difficulties for the current injection from the electrodes into conjugated carbon-based molecules via the usual thiol bonds.*

## 7.1 Introduction

Recent years have witnessed a great amount of both fundamental and applied research in molecular electronics<sup>6-8, 10-17, 171</sup>. A fundamental requirement for a molecule or a nanotube to be considered as a molecular wire is the ability to transport charge carriers with a reasonably low resistance. However, at the contacts between molecular wires and electrodes, an additional "parasitic" resistance is usually present, which determines the overall transport properties of the device. As molecular wires, conjugated carbon-based molecules (CCBM) or carbon nanotubes (CNT)<sup>21</sup> have been considered so far. In the systems with CCBM, sulfur is a common "alligator clip" used for coupling of the molecules with the<sup>25, 172-174</sup> electrodes. Albeit the presence of *S-Au* hybridization, the charge carrier injection into the molecular systems is difficult<sup>172, 174</sup>. Since the valence resonances of atoms with high electronegativity tend to lie well below the Fermi level of the electrodes, the resonant transmission is suppressed at the molecule-electrode interface<sup>175, 176</sup>.

While the CCBMs are usually coupled to gold electrodes via chemically robust thiolate bonds<sup>25</sup>, the CNTs only weakly physisorb to electrodes. Opposite to the unique mechanical and electronic properties of CNT<sup>177</sup>, the current injection through CNT-electrode contacts is difficult, because of the usually indispensably high potential barrier at CNT-electrode contacts<sup>178</sup>. That drawback can be compensated with a large contact area<sup>179</sup>, however, the electrode of the coated CNT can induce the pressure onto CNT, which can additionally affect the electronic transport<sup>180</sup>.

In this chapter the quality of contacts between molybdenum sulfide  $Mo_6S_6$  nanowires (NWs) and a gold electrode is investigated. The structural, electronic, and optical properties of the infinite  $Mo_6S_6$  and related NWs are theoretically and experimentally investigated in detail by



various authors<sup>108-111, 119, 126, 128, 181, 182</sup>, and also in this thesis. It has been shown in the thesis in **Chapter 3** that many shortcomings presented in the systems with CNTs may nicely be resolved within the systems consisting of  $Mo_6S_{6-x}I_x$  NWs<sup>128</sup>. However, in contrast to popular CCBMs and CNTs, their potential to become unique building blocks of nanodevices, which generally consist of the nanowires coupled to electrodes, has barely researched so far<sup>23</sup>. After successful synthesis and the measurements of the electronic transport properties of the isoelectronic  $Mo_6Se_6$  NWs<sup>23</sup>, recent years witnessed the series of the experiments of the related  $Mo_xS_yI_z$  NWs<sup>93, 104</sup>. Additionally, the nanowires tend to self-assemble into the networks, interconnecting the gold particles<sup>93, 104</sup>, which can be the crucial step towards the integration of the nanostructures into the integrated electronic devices.

The main idea presented in this chapter is to explore the possibility of an ideal, point Ohmic contact between  $(Mo_6S_6)_n$  nanowire and the gold electrodes. The nanowire is formed by a  $Mo$ -backbone, "decorated" with  $S$  atoms (side view shown in **Figure 32**). The  $Mo$  core consists of  $Mo$  trimers of alternating orientation forming a chain. Within such geometry, upon coupling with the electrodes by sulfur atoms, the metallic molybdenum backbone would be in direct contact with the electrodes, hence the metal to metal transmission channels would be opened for the current injection.

## 7.2 Computational details

Density functional based tight binding (DFTB) method<sup>63, 114</sup> extended with Green's function formalism<sup>85, 86</sup> is used to determine all properties presented in this paper. Ceperly-Alder parametrization of the exchange-correlation functional in the local density approximation (LDA) is employed, including scalar relativistic corrections. The parameters employed for the creation of the Hamiltonian and overlap matrices which are used in the DFTB calculations are described in detail in **Chapter 2.3**. The DFTB method has been used successfully for description of many molybdenum-chalcogenide structures<sup>79, 116, 117, 128</sup>, as well as gold nanoparticles<sup>183</sup>.

Two cluster types are considered: the bare fragments  $(Mo_6S_6)_n$  with  $n$  unitcells ( $n = 1...20$ ), and the same fragments capped with two sulfur atoms, one per each end of the wire (one of them is indicated by the arrow in **Figure 32**). The clusters with  $n = 20$  unitcells are analyzed in detail, where the properties of smaller systems are just briefly discussed. The optimized geometries with NWs consisting of only eight unitcells (in order to gain an comprehensive view of the whole structures) are shown in two lower panels of **Figure 32**, whereas the two upper panels depict a detailed view of the electrode-NW contacts. In the following the two contact geometries will be referred as *type A* and *type B* contacts, respectively. For *type A* contact, the cluster axis is aligned along the leads, when the alternating *Mo* trimers of the cluster layers continue A-B-C stacking of the gold electrodes. It is not the case for the *type B* geometry, where the cluster is inclined by 54.7 degrees with respect to the direction of electrodes. In the latter

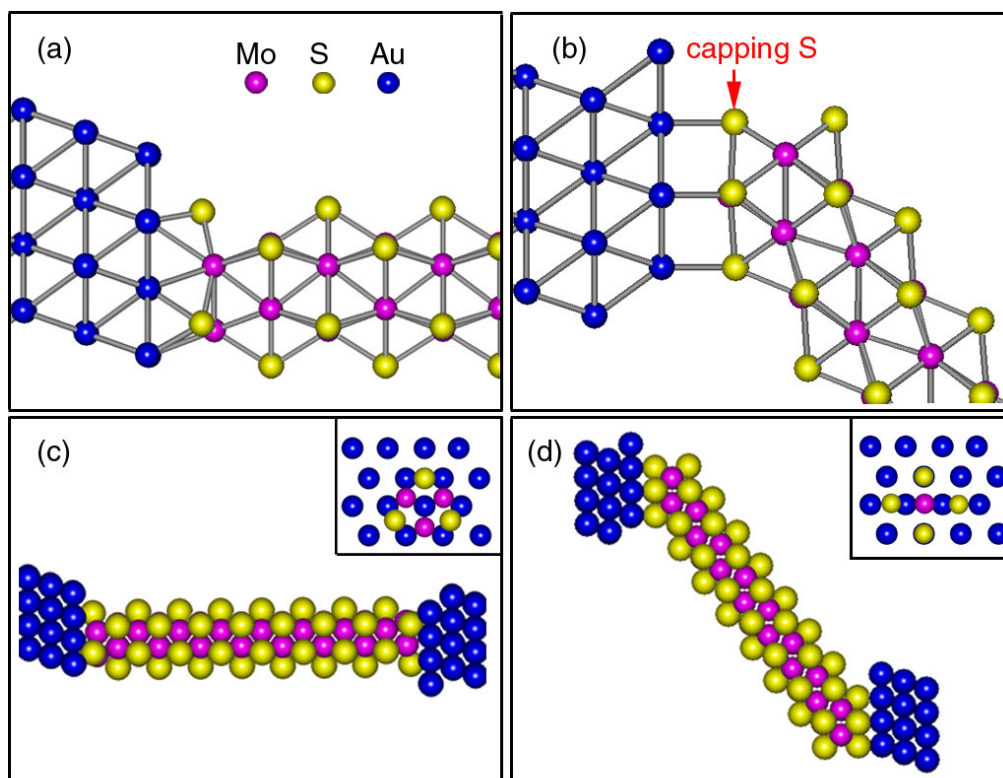


**Figure 32:** Comprehensive view of the geometry of a  $Mo_6S_6$  nanowire in contact of *type A* (a) and *type B* (b) with the gold electrode. Whole device consisting of the nanowire with eight unitcells coupled to two gold electrodes with *type A* (c) and *type B* (d) contacts geometries.

geometry, only one *Mo* atom is in direct contact with the gold surface, whereas in the former one there are three *Mo* atoms. Before connecting to the leads, the geometries of the free clusters were fully optimized. Each electrode consists of *Au* (111) surface, with four rows of *Au* atoms in both directions, and *Au*-*Au* bondlength of 2.88 Å. The adsorption geometries of the elongated clusters on the *Au* (111) surface correspond to data obtained by DFT (see <sup>130, 184, 185</sup> and **Chapter 6**) relaxations of  $\text{Mo}_6\text{S}_8$  and  $\text{Mo}_4\text{S}_6$  cluster upon their deposition on *Au* (111) surface. It will be shown in the following text that electronic structure of the adsorbed nanowires is changed only on the atomic sites which are in direct contact to the gold electrodes. This property is obtained also for  $\text{Mo}_6\text{S}_8$  and  $\text{Mo}_4\text{S}_6$  clusters on the gold surface <sup>130, 184</sup>. This finding in addition to the fact that  $\text{Mo}_6\text{S}_6$  nanowires are structural extensions to the  $\text{Mo}_6\text{S}_8$  cluster are indications that  $\text{Mo}_6\text{S}_6$  wires bind to gold in similar way as  $\text{Mo}_6\text{S}_8$  cluster (or  $\text{Mo}_4\text{S}_6$  cluster for the  $\text{Mo}_6\text{S}_6$  wire saturated with 2 sulfur atoms at its ends). In the insets of **Figure 32** are shown the positions of the contacting atoms, as seen from the surface normal direction.

### 7.3 Electronic and transport properties

#### 7.3.1 Transport properties

The calculated transmission spectra of  $(\text{Mo}_6\text{S}_6)_{20}$  NWs sandwiched between two gold electrodes are shown in **Figure 33**. Electronic transmission of infinite periodic  $\text{Mo}_6\text{S}_6$  nanowire is also shown in the figure for the comparison. In contrast to the transmission of the periodic wire, which is part-by-part constant at different energy regions, the transmission of the finite nanowires segment is discrete, with distinguishable peaks around the Fermi energy. Except in very short segments (which transmission curves are not shown here), where the electronic transport is of mainly ballistic character due to overlapping of the electrodes' states, the transmission resonances at zero bias closely mirrors the intrinsic electronic structure of the fragments; hence the electronic transport is of resonant type. In the calculated range of the bias, the conductance is by around 10-20 percent smaller in the case of a tilted cluster. The current shown in **Figure 34** is obtained for the electronic temperature of 300 K. It obeys a linear form around zero bias, indicating a good Ohmic contacts, which corresponds to the reported experimental data of an isoelectronic  $\text{Mo}_6\text{Se}_6$  NW<sup>23</sup>. Comparing the transmission coefficient of the wires fragment and free, infinite NW, one may naïvely conclude that the electronic transport

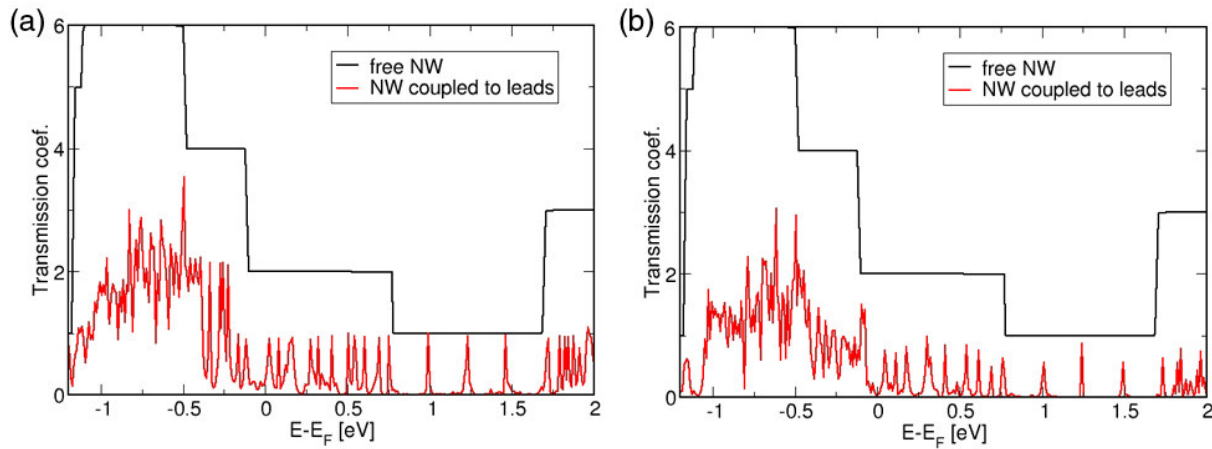


**Figure 33:** Electronic transmission of the system with *type A* (a) and *type B* (b) contacts are shown with red lines. Black lines represent the transmission of an ideal periodic  $\text{Mo}_6\text{S}_6$  nanowire.

is significantly reduced due to introduction of the contacts. In the energy region between 1.2 and 1.7 eV, the Lorentzian-shaped peaks have maximum value of one in *type A* contact. Left from this range, down to -0.2 eV, the density of the resonancies is increased, but each of them retains the height of the almost ideal transmission. In the infinite nanowire, two bands are formed in that energy region (marked with red and blue in **Figure 35** (a)), hence the two conducting channels are opened, with a total transmission coefficient of two. For long enough wire fragments, the transmission peaks would merge and form the same continuous transmission spectra observed for infinite NW. Data in **Figure 33** (a) indicate the ideal transmission of the charge carriers in the energy region between -0.2 eV and 1.7 eV. Following the work of Nemec *et al.*, where the contacts between electrode and CNTs are investigated, we find the *contact reflection coefficient*  $\rho = 1/\langle T \rangle - 1/T_{band}$  in that energy region to be  $\sim 10^{-3}$ . In the last formula, the averaging of transmission is done over the above-mentioned energy regions. On the other hand, the potential barrier at the CNT-electrode contacts prevents the easy carrier injection; in order to achieve the similar values of  $\rho$ , the large contact area is mandatory<sup>179</sup>.

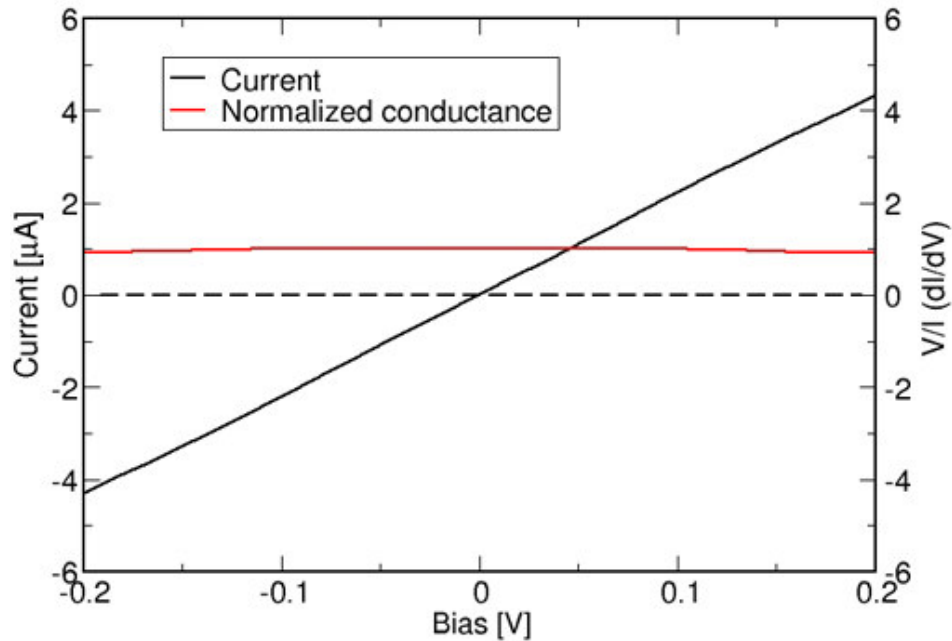


**Figure 34:** Current (black) and normalized differential conductance (red) of *type A* contact.

### 7.3.2 Electronic properties

To get a deeper insight into the physical origin of the transport properties, density of states (DOS) projected on the contacting atoms is analyzed, at third layer of the wire (0.9 nm distant from electrode), and in its mid-point within *type A* contact geometry (**Figure 35** (b,c, and d)). The electronic structure of the terminating *Mo* atoms in the free cluster differs significantly from the ones originating at other layers of the cluster. Above Fermi level many localized states are immanent, which originate from unsaturated (dangling) bonds. The projected density of

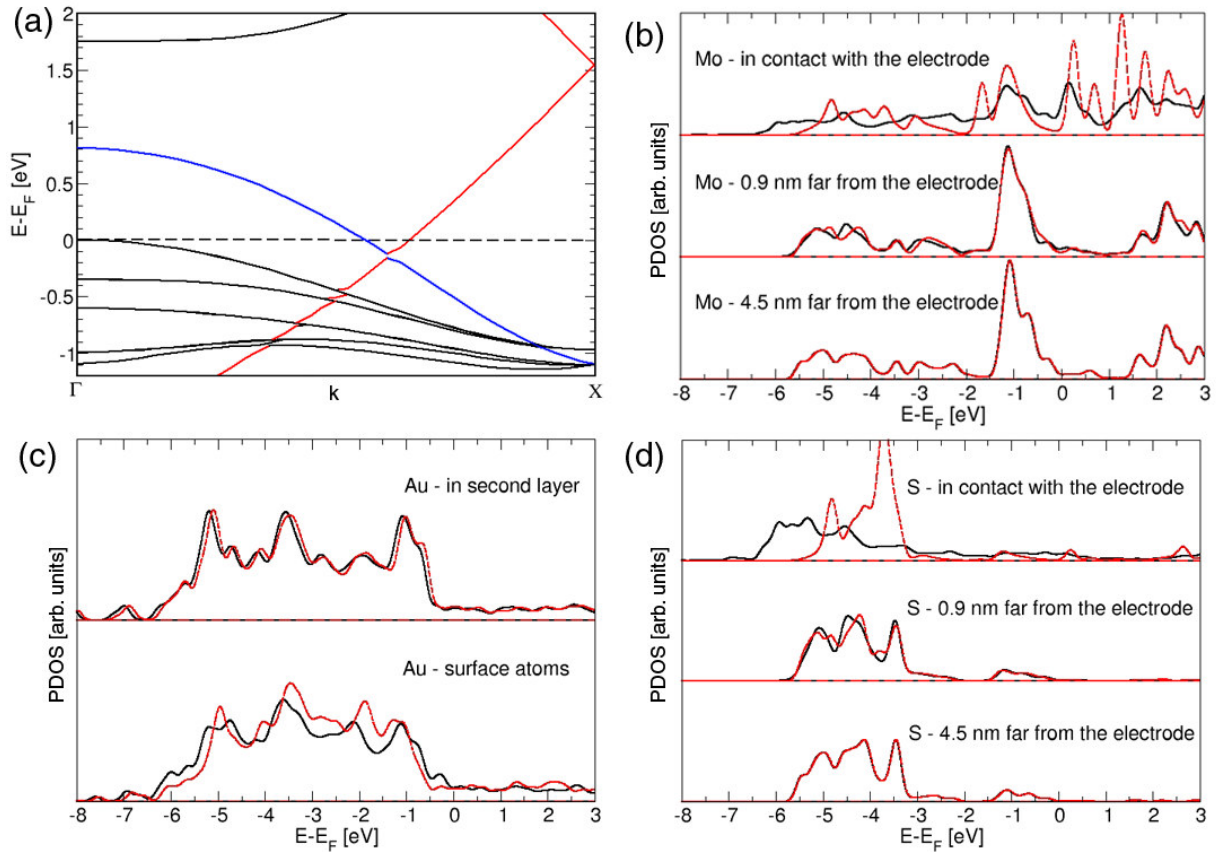


**Figure 35:** Band structure of a periodic  $\text{Mo}_6\text{S}_6$  nanowire (a). Projected density of states on Mo (b), Au (c) and S (d) atoms in *type A* contact. Dashed-red curves correspond to the free  $(\text{Mo}_6\text{S}_6)_{20}$  cluster and free electrode, whereas black curves correspond to the cluster coupled to the gold electrode. For better pictorial representation, DOS is *a posteriori* broadened by convolution with Gaussian functions of 0.01 eV width at half maximum.

states (PDOS) of the third cluster layer resembles to intrinsic, non-perturbed electronic levels, which indicates the altering of the electronic structure only at the narrow region of the contact area. PDOS of *S* atoms of the free cluster is considerably smaller above -2 eV, where the cluster levels are primarily of *Mo* bonding and non-bonding character. Upon the coupling of NW to leads, new states appear between -0.6 eV and Fermi level, indicating the existence of *Mo-Au* bonds. The influence of the electrodes is screened by the metallic nanowire already at the third cluster layer, whose electronic structure converges rapidly towards the intrinsic one (at the wires midpoint). Below -5 eV the PDOS is increased, especially on *S* and *Au* sites, indicating the presence of *S-Au* bonds. After deposition, PDOS on *S* atoms remains small in the energy region  $\pm 2$  eV around Fermi level, similar to systems with CCBMs<sup>175, 176</sup>. The overall electronic structure is very similar to one obtained for *Mo<sub>4</sub>S<sub>6</sub>* and *Mo<sub>6</sub>S<sub>8</sub>* clusters deposited on *Au* (111) surface. This confirms the idea that *Mo<sub>6</sub>S<sub>6</sub>* nanowire binds to *Au* (111) surface in the same way as the mentioned clusters do. As it is already noted, the small PDOS of *S* atoms around Fermi level causes difficulties in the current injection from electrodes to CCBMs through usual thio-bonds. However, the small PDOS of *S* atoms does not affect the transmission through *Au-Mo<sub>6</sub>S<sub>6</sub>* contacts, due to a unique "task sharing" between *Mo* and *S* atoms: while *S* atoms bind the NW to the electrodes, charge carrier transmission reside primarily through direct metal to metal, *Mo-Au* channels.

In the free clusters without capping *S* atoms, the charges are non-equally distributed; on ending sulfur atoms it is -0.60 e per atom (negatively charged), and -0.45 e on *S* atoms towards the nanowires midpoint. The *Mo* atoms obey even larger charging, up to 1.58 e at ends of the wire, and down to 0.38 e at its midpoint. Very important is the charge redistribution upon coupling of the NWs to the leads, when the charge on sulfur at contacts is only -0.05 e per atom, and -0.18 e farther from them. Charge redistribution across *Mo* atoms is equilibrated to the same value of 0.18 e per atom, with the exception of the three first layers of the wire, where the charge increases from 0.12 e at the very end of the wire up to 0.18 e towards the wires midpoint. Only about 0.12 electrons are transferred from the cluster to the electrodes. The absence of the larger charging spots in the *Mo*-backbone causes the lack of the mirror charges in the metallic leads and the electrostatic dipol at the cluster-gold interfaces. The mirror charges are usual in the contacts

with metals. The absence of the dipole and its electric field at the contact causes a good transparency for the unperturbed flow of electric current through the system.

In recent experiments with related molybdenum chalcogenide nanowires<sup>93, 94</sup> has been explored a unique self-assembling mechanism. Namely, after deposition of these nanowires on a semiconducting surface randomly covered by gold nanoparticles, the nanowires take the orientations such that they interconnect the gold nanoparticles. They contact the nanoparticles only with their ends, whereas there were not observed some contacts with the gold nanoparticles towards the middle points of the wires. In such way, unique networks are formed, with nodes made of gold nanoparticles, and interconnections consisted of the nanowires. The finding of the charge distribution in free clusters indicates a possible mechanism for the process of the self-assembling. The highly localized large charges and the unsaturated dangling bonds at the ends of the free nanowires can yield the tendency of the nanowires for their bonding with the gold particles (nodes of the network), primarily at these wires' ends.

### 7.3.3 The potential barrier

The potential barrier is of special importance for the current injection, since the electron transmission through the barrier exponentially decays with the width and height of the barrier. In **Figure 36** is shown the electrostatic potential at *Au*-nanowire contacts, which is evaluated self-consistently from the charge density. *Type A* contact is completely transparent with only a negligibly high barrier, while in *type B* contact the barrier height amounts to 0.4 eV. The potential is calculated utilizing Poisson equation on 65 x 65 x 260 grid in the real space. In **Figure 36** is depicted the potential at one cross-sections along wires axis, (a scan of the potential at other cross section is also obtained).



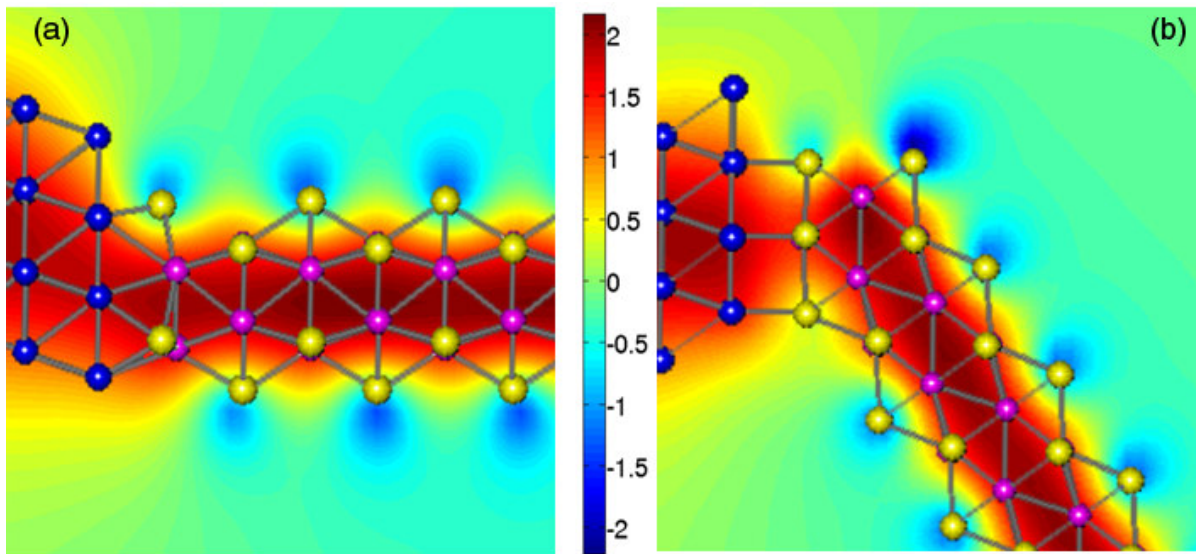


**Figure 36:** Electrostatic (Hartree) potential at *type A* (a) and *type B* (b) contacts. The scale is given in units of electronvolts.

*Type A* contact is completely transparent with only a negligibly high barrier, while in *type B* contact the barrier height amounts up to 0.4 eV. Local density of states of the single *Mo* atom at the contact B is not high enough to screen out the negative potential of the four surrounding *S* atoms. That degrades the transmission with respect to *type A* contact **Figure 33** (b)). In contrast, the local density of states originating from three *Mo* atoms at the *type A* contact is still high enough for the complete screening of the potential originating from three contacting *S* atoms, which are only weakly charged. Hence, the applied bias on the electrodes probes the intrinsic electronic structure of the molybdenum sulfide NWs, rather than the contact properties.

## 7.4 Conclusions

In conclusion, a novel type of electronic contacts between molybdenum sulfide NW and gold electrode is investigated. It is found that the contact A is ideally transparent for the carrier injection. Opposite to the thiol-based contacts where all current through the system is transmitted through sulfur atoms, in our system the sulfur atoms bind the NW to the electrodes, but do not significantly influence the electron transmission, because they are spatially and electronically distinct from the pathway of the current. Molybdenum is the main carrier of the current, which

passes through the direct Au-(Mo backbone)-Au conducting channels. In contrast to CNT-Au contacts, the lack of the potential barrier between the Mo-backbone and the electrodes assures the easier injection of the charge carrier into the nanowires. Additionally, the symmetry of the Mo-backbone is close to the symmetry of the electrodes, which further decreases the backscattering of the propagating waves at the contacts. The unique "task sharing" between the contacting atoms is a general idea which can be a guidance for choice of appropriate molecular conductors in future nanodevices.

## 8 Summary

Molybdenum chalcogenide nanowires were investigated in detail, including their structural, electronic, and transport properties. It has been shown that nanowires have the following very similar properties as carbon nanotubes despite their different atomic structures:

1. A very high axial stiffness, which is five orders of magnitude larger than the axial stiffness of steel;
2. The electronic band structure of the molybdenum chalcogenide nanowires around the Fermi level closely corresponds to the band structure of armchair carbon nanotubes: Two linear bands intersect at the Fermi level. The first van Hove singularities close to the Fermi level in case of (13,13) CNT and the most stable  $\text{Mo}_6\text{S}_4\text{I}_2$  isomer of molybdenum chalcogenide nanowires are found with the same energy.

Apart from these similarities, the molybdenum chalcogenide nanowires can overcome some major drawbacks of CNTs as well as of molecular electronics devices:

1. A free-standing nanowire can be easily separated from its bundle since nanowires in the bundle in average<sup>7</sup> attract each other weaker than CNTs due to larger higher anisotropy.
2. Nanowires are always metallic that is in contrast to CNTs, which electronic properties sensitively depend on their internal “variables”, such as chirality.
3. Multi-wall CNTs (MWCNTs) are usually synthesized in laboratories. The SWCNTs are often not constituted from identical CNTs, but rather from different ones with different properties. The overall properties of a MWCNT depend in a complex way on the properties of each CNT it contains, and on mutual interactions between these CNTs in the MWCNT. Molybdenum chalcogenide nanowires do not make similar nested systems, because of their simpler geometries.
4. In contrast to CNTs, which kink upon their bending that causes changes in their transport properties, the bent molybdenum sulfide nanowires retain their structural integrity and their metallicity.
5. Twisting of molybdenum sulfide nanowires causes a metal–insulator transition. A gap in transmission spectra opens monotonically with the torsional angle. This is in

---

<sup>7</sup> In average over their orientational angle. For details see Chapter 3

contrast to CNTs, which conductance oscillates with the torsional angle. Therefore, a molybdenum sulfide nanowire can be utilized as a unique *switch*, or even a potentiometer in future nanodevices.

6. Bending energy of  $\text{Mo}_6\text{S}_6$  nanowires is by an order of magnitude smaller than the corresponding energy of CNTs. Since the wire remains metallic irrespective of its bending angle, this observation implies that  $\text{Mo}_6\text{S}_6$  wires can easily adapt to fine features of nano-templates, and flexibly transmit electronic current
7. Ohmic-like properties of contact between a  $\text{Mo}_6\text{S}_6$  wire and a gold electrode are observed in the results of calculations. The transparency of contacts is characterized by the *contact reflection coefficient* (CRC), which is  $\sim 10^{-3}$  for such point contact. The same small value of CRC for contacts employing CNTs can be obtained only with considerably larger contact area.
8. Molybdenum chalcogenide nanowires have sulfur atoms as their integral part. Sulfur is usually utilized for binding various conjugated carbon-based molecules (CCBMs) to noble metal electrodes. In these systems with sulfur atoms as “alligator clips” electrons have difficulties to tunnel the potential barrier that often appears at the molecule-S atom-electrode interfaces. The origin of these difficulties is in two reasons: First, the local density of states on S atoms, which should “carry” the current, is usually very small in such systems. Second, S atoms introduce a potential barrier at the interfaces. The electrode- $\text{Mo}_6\text{S}_6$  nanowire contacts utilize a unique feature termed as “task sharing” in the thesis. Sulfur atoms are spatially and electronically distinct from molybdenum atoms. Their local density of states is also small around the Fermi level, which however, does not effect the transport through the system since the electronic current flows through direct *Mo*-electrode conduction channels.

To conclude, the molybdenum chalcogenide nanowires possess unique properties not found in other nanosystems. They can be utilized as nanocables to flexibly transmit the informations between logic elements in integrated devices. The  $\text{Mo}_6\text{S}_6$  nanowires have a potential to be used also as logic elements, thanks to their unique switching property. Integration of the nanowires with other materials via gold electrodes is also feasible through their perfect, point-like, Ohmic contacts. Therefore, molybdenum chalcogenide nanowires

have large potential for their utilization in almost every part of future nanometer-sized devices.



## 9 Bibliography

1. G. E. Moore, *Electronics* **1965**, 38, 114.
2. J. R. Heath; P. J. Kuekes; G. S. Snider; R. S. Williams, *Science* **1998**, 280, 1716.
3. M. A. Reed; J. M. Tour, *Sci. Am.* **2000**, 292, 86.
4. D. E. Whitney, *Res. Eng. Des.* **1996**, 8, 125.
5. A. Hand, *Semiconductor Intl.* **2001**, 24, 62.
6. F. Pump; G. Cuniberti, *Surf. Sci.* **2007**, 601, 4109.
7. N. Armstrong; R. C. Hoft; A. McDonagh; M. B. Cortie; M. J. Ford, *Nanolett.* **2007**, 7, 3018.
8. F. Chen; J. Hihath; Z. Huang; X. Li; N. J. Tao, *Ann. Rev. Phys. Chem.* **2007**, 58, 535.
9. Y. Q. Zhu; W. B. Hu; W. W. Hsu; M. Terrones; N. Grobert; T. Karali; J. P. Hare; P. D. Townsend; H. W. Kroto; D. R. M. Walton, *Adv. Mater.* **1999**, 11, 844.
10. P. A. Derosa; J. M. Seminario, *J. Phys. Chem. B* **2000**, 105, 471.
11. C. Joachim; J.K.Gimzewski; A. Aviram, *Nature (London)* **2000**, 408, 541.
12. P. Samori; N. Severin; K. Mullen; J. P. Rabe, *Adv. Mater.* **2000**, 12, 579.
13. A. Nitzan, *Annu. Rev. Phys. Chem.* **2001**, 52, 681.
14. M. A. Reed; J. Chen; A. M. Rawlett; D. W. Price; J. M. Tour, *Appl. Phys. Lett.* **2001**, 78, 3735.
15. J. R. Heath; M. A. Ratner, *Phys. Today* **2003**, 56, 43.
16. J. M. Tour, *Molecular Electronics*. World Scientific: Singapore, 2003.
17. S. Datta, *Electronic transport in mesoscopic systems*. University Press: Cambridge, 1997.
18. M. D. Valle; R. Gutierrez; C. Tejedor; G. Cuniberti, *Lett. to Nature* **2007**, 2, 176.
19. G. S. Ohm, *Die Galvanische Kette, Mathematisch Bearbeitet*. Riemann: Berlin, 1827.
20. S. Iijima, *Nature (London)* **1991**, 354, 56.
21. S. Iijima; T. Ichihashi, *Nature* **1993**, 363, 603.
22. T. C. Karni; L. Segev; O. S. Lavi; S. R. Cohen; E. Joselevich, *Nature Nanotech.* **2006**, 1, 36.
23. L. Venkataraman; C. M. Lieber, *Phys. Rev. Lett.* **1999**, 83, 5334.
24. F. Zahid; M. Paulsson; S. Datta, *Electrical conduction through molecules*. Academic Press: 2003.
25. A. N. Andriotis, *Phys. Rev. B* **2007**, 76, 045412.
26. S.-H. Ke; H. U. Baranger; W. Yang, *J. Chem. Phys.* **2005**, 122, 074704.
27. Z.-L. Liang; B. Zou; C. K. Wang, *Phys. Rev. B* **2006**, 73, 075326.
28. A. A. Farajian; R. V. Belosludov; H. Mizuseki; Y. Kawazoe, *Physica E* **2003**, 18, 253.
29. A. Kahn; N. Hoch, *J. Polymer Sci. B* **2003**, 41, 2529.
30. I. G. Hill; A. Rajagopal; A. Kahn, *Appl. Phys. Lett.* **1998**, 73, 662.
31. J. M. Seminario; C. E. De La Cruz; P. A. Derosa, *J. Am. Chem. Soc.* **2001**, 123, 5616.
32. Y. Hu; Y. Zhu; H. Gao; H. Guo, *Phys. Rev. Lett.* **2005**, 95, 156803.
33. H. Grönbeck; A. Curioni; W. Andreoni, *J. Am. Chem. Soc.* **2000**, 122, 3839.
34. Y. Yourdshahyan; H. K. Zhang; A. M. Rappe, *Phys. Rev. B* **2001**, 63, 81405.
35. T. Hayashi; Y. Morikawa; H. Nozoye, *J. Chem. Phys.* **2001**, 114, 7615.
36. H. Kondoh; M. Iwasaki; T. Shimada; K. Amemiya; T. Yokoyama; T. Ohta; M. Shimomura; S. Kono, *Phys. Rev. Lett.* **2003**, 90, 66102.

37. K. M. Berdmore; J. D. Kress; N. Gronbech-Jensen; A. R. Bishop, *Chem. Phys. Lett.* **1998**, 286, 40.
38. A. Grigorijev; J. Skoldberg; G. Ewendin; Z. Crljen, *Phys. Rev. B* **2006**, 74, 045401.
39. H. Kondo; H. Kino; J. Nara; T. Ozaki; T. Ohno, *Phys. Rev. B* **2006**, 73, 235323.
40. J. Tomfohr; O. F. Sankey, *J. Chem. Phys.* **2004**, 120, 1542.
41. S.-H. Ke; H. U. Baranger; W. Yang, *J. Am. Chem. Soc.* **2004**, 126, 15897.
42. H. Baschand; M. A. Ratner, *J. Chem. Phys.* **2004**, 120, 5771.
43. P. Hohenberg; W. Kohn, *Phys. Rev.* **1964**, 136, B864.
44. J. F. Janak, *Phys. Rev. B* **1978**, 18, 7165.
45. J. P. Perdew; G. P. Robert; L. Mel; L. B. Jose, *Phys. Rev. Lett.* **1982**, 49, 1691.
46. D. M. Ceperley; B. J. Alder, *Phys. Rev. Lett.* **1980**, 45, 566.
47. W. Koch; M. C. Holthausen, *A Chemist's Guide to Density Functional Theory*. Wiley-VCH: 2001.
48. M. Filatov; W. Thiel, *Mol. Phys.* **1997**, 91, 847.
49. J. P. Perdew, *Unified Theory of Exchange and Correlation Beyond the Local Density Approximation*. Akademie, Verlag: Berlin, 1991.
50. G. J. Laming; V. Termath; N. C. Handy, *J. Chem. Phys.* **1993**, 99, 8765.
51. A. D. Becke, *J. Chem. Phys.* **1986**, 84, 4524.
52. J. P. Perdew, *Phys. Rev. B* **1986**, 33, 8822.
53. D. J. Lacks; R. G. Gordon, *Phys. Rev. A* **1993**, 47, 4681.
54. J. P. Perdew; K. Burke; M. Ernzerhof, *Phys. Rev. Lett.* **1996**, 77, 3865.
55. J. P. Perdew; A. Zunger, *Phys. Rev. B* **1981**, 23, 5048.
56. S. Goedecker; M. Teter; J. Huetter, *Phys. Rev. B* **1996**, 54, 1703.
57. J. A. Appelbaum; D. R. Hamann, *Phys. Rev. B* **1973**, 8, 1777.
58. J. R. Shlutter; S. G. Chelikowsky; S. G. Loui; M. L. Cohen, *Phys. Rev. B* **1975**, 12, 4200.
59. C. F. Melius; W. A. Goddard, *Phys. Rev. A* **1974**, 10, 1528.
60. A. Zunger; M. L. Cohen, *Phys. Rev. Lett.* **1978**, 41, 53.
61. N. Troullier; J. L. Martins, *Phys. Rev. B* **1991**, 43, 1993.
62. G. Seifert; G. Eschrig, *Zeitschrift fuer physikalische Chemie (Leipzig)* **1986**, 267, 629.
63. D. Porezag; T. Frauenheim; T. Koehler; G. Seifert; R. Kaschner, *Phys. Rev. B* **1995**, 51, 12947.
64. M. Elstner; D. Porezag; G. Jungnickel; J. Elsner; M. Haugk; T. Frauenheim; S. Suhai; G. Seifert, *Phys. Rev. B* **1998**, 58, 7260.
65. C. Koehler; G. Seifert; U. Gerstmann; M. Elstner; H. Overhof; T. Frauenheim, *Phys. Chem. Chem. Phys.* **2001**, 3, 5109.
66. T. A. Niehaus; S. Suhai; F. Della Salla; P. Luigi; M. Elstner; G. Seifert; T. Frauenheim, *Phys. Rev. B* **2001**, 63, 085108.
67. T. Heine; M. Buhl; P. W. Fowler; G. Seifert, *Chem. Phys. Lett.* **2000**, 316, 373.
68. S. Hazebroucq; G. S. Picard; C. Adamo; T. Heine; S. Gemming; G. Seifert, *J. Chem. Phys.* **2005**, 123, 134510.
69. J. Frenzel; S. Gemming; G. Seifert, *Phys. Rev. B* **2004**, 70, 235404.
70. J. Frenzel; A. F. Oliveira; H. A. Duarte; T. Heine; G. Seifert, *Zeitschrift fuer anorganische und allgemeine Chemie* **2005**, 631, 1267.
71. J. Frenzel; J.-O. Joswig; P. Sarkar; G. Seifert; M. Springborg, *Eur. J. Inorg. Chem* **2005**, 18, 3585.
72. T. Heine; P. W. Fowler; G. Seifert, *Sol. Stat. Comm.* **1999**, 111, 19.
73. M. Haugk; J. Elsner; T. Frauenheim; T. Staab; C. Latham; R. Jones; H. Leipner; T. Heine; G. Seifert; M. Sternberg, *Phys. Stat. Sol. B* **2000**, 217, 473.



74. C. Chen; H. Jiao; G. Seifert; A. H. C. Horn; D. Yu; T. Clark; W. Thiel; O. V. R. Schleyer, *J. Comp. Chem.* **2003**, 24, 948.
75. M. Elstner, *Theor. Chimica Acta* **2006**, 116, 316.
76. V. Ivanovskaya; T. Heine; S. Gemming; G. Seifert, *Phys. Stat. Sol. B* **2006**, 243, 1757.
77. A. N. Enyashin; G. Seifert, *Phys. Stat. Sol. B* **2005**, 242, 1361.
78. K. M. Rogers; P. Fowler; G. Seifert, *Chem. Phys. Lett.* **2000**, 332, 43.
79. G. Seifert; H. Terrones; M. Terrones; G. Jungnickel; T. Frauenheim, *Phys. Rev. Lett.* **2000**, 85, 146.
80. M. Elstner; T. Frauenheim; E. Kaxiras; G. Seifert; S. Suhai, *Phys. Stat. Sol. B* **2000**, 217, 357.
81. T. Koehler; T. Frauenheim; G. Jungnickel, *Phys. Rev. B* **1995**, 52, 11837.
82. K. Jackson; M. R. Pederson; D. Porezag; Z. Hajnal; T. Frauenheim, *Phys. Rev. B* **1997**, 55, 2549.
83. T. Heine; G. Seifert; P. Fowler; F. Zerbetto, *J. Phys. Chem. A* **1999**, 103, 8738.
84. M. Sternberg; G. Galli; F. T., *Comp. Phys. Comm.* **1999**, 118, 200.
85. A. Pecchia; A. D. Carlo, *Rep. Prog. Phys.* **2004**, 67, 1497.
86. A. D. Carlo; M. Gheorghe; A. Bolognesi; P. Lugli; M. Sternberg; G. Seifert; T. Frauenheim, *J. Comp. Elec.* **2002**, 1, 109.
87. H. Eschrig, *The optimized LCAO method and Electronic Structure of Extended Systems*. Akademie-Verlag: Berlin, 1988.
88. A. N. Goldstein; C. M. Echer; A. P. Alivisatos, *Science* **1992**, 256, 1425.
89. K. Koepnick; G. Eschrig, *Phys. Rev. B* **1999**, 59, 1743.
90. R. Pariser, *J. Chem. Phys.* **1956**, 24, 125.
91. R. G. Parr; R. G. Pearson, *J. Amer. Chem. Soc.* **1983**, 105, 1503.
92. N. Takeuchi; C. T. Chan; K. M. Ho, *Phys. Rev. B* **1991**, 43, 13899.
93. B. Bercic; U. Pirnat; P. Kusar; D. Dvorsek; D. Mihailovic, *Appl. Phys. Lett.* **2006**, 88, 173103.
94. M. I. Ploscaru; S. J. Kokalj; M. Uplaznik; D. Vengust; D. Turk; A. Mrzel; D. Mihailovic, *Nanolett.* **2006**, 7, 1445.
95. F. Guinea; C. Tejedor; F. Flores; E. Louis, *Phys. Rev. B* **1983**, 28, 4397.
96. M. P. S. Lopez; J. M. S. Lopez; J. Rubio, *J. Phys. F: Mat. Phys.* **1984**, 14, 1205.
97. M. P. S. Lopez; J. M. S. Lopez; J. Rubio, *J. Phys. F: Mat. Phys.* **1985**, 15, 851.
98. A. Umerski, *Phys. Rev. B* **1997**, 55, 5266.
99. A. Simon, *Angew. Chem. Int. Ed.* **1988**, 27, 159.
100. J. V. Lauritsen; J. Kibsgaard; S. Helveg; H. Topsoe; B. S. Clausen; E. Laegsgaard; F. Besenbacher, *Nature Nanotechnology* **2007**, 2, 53.
101. L. Rapoport; Y. Bilik; Y. Feldman; M. Homyonfer; S. R. Cohen; R. Tenne, *Nature (London)* **1997**, 387, 791.
102. L. Joly-Pottuz; F. Dassenoy; M. Belin; B. Vacher; J. Martin; N. Fleischer, *Tribol. Lett.* **2005**, 18, 477.
103. M. S. Dresselhaus; G. Dresselhaus; P. Avouris, *Carbon Nanotubes: Synthesis, Structure, Properties and Applications*. Springer: Berlin, 2001.
104. D. Vrbancic; M. Remskar; A. Jesih; A. Mrzel; P. Umek; M. Ponikvar; B. Jancar; A. Meden; B. Novosel; S. Pejovnik; P. Venturini; J. C. Coleman; D. Mihailovic, *Nanotech.* **2004**, 15, 635.
105. W. Kohn; L. Sham, *Phys. Rev.* **1965**, 140, A1133.
106. J. Taylor; H. Guo; J. Wang, *Phys. Rev. B* **2001**, 63, 245407.

107. M. Brandbyge; J.-L. Mozos; P. Ordejon; J. Taylor; K. Stokbro, *Phys. Rev. B* **2002**, 65, 165401.
108. T. Hughbanks; R. Hoffmann, *J. Am. Chem. Soc.* **1983**, 105, 1150.
109. M. Potel; R. Chevrel; M. Sergent; J. C. Armici; M. Decroux; O. Fischer, *J. Sol. State Chem.* **1980**, 35, 286.
110. F. J. Ribeiro; D. J. Roundy; M. L. Cohen, *Phys. Rev. B* **2002**, 65, 153401.
111. S. Gemming; G. Seifert; I. Vilfan, *Phys. Stat. Sol. B* **2006**, 243, 3320.
112. J. M. Soler; E. Artacho; J. D. Gale; A. Garcia; J. Junquera; P. Ordejon; D. Sanchez-Portal, *J. Phys. Condens. Matter* **2002**, 14, 2745.
113. L. Kleinman; D. M. Bylander, *Phys. Rev. Lett.* **1982**, 48, 1425.
114. G. Seifert; D. Porezag; T. Frauenheim, *Int. J. Quant. Chem.* **1996**, 58, 185.
115. S. Gemming; G. Seifert, *Novel Elongated Molybdenum Sulfide Nanostructures in Proc. 19th International Winterschool on Electronic Properties of Novel Materials* **2005**.
116. A. N. Enyashin; S. Gemming; M. Bar-Sadan; R. Popovits-Biro; S. Hong; Y. Prior; R. Tenne; G. Seifert, *Angew. Chem. Int. Ed.* **2007**, 46, 623.
117. A. N. Enyashin; S. Gemming; G. Seifert, *Eur. J. Phys. S. T.* **2007**, 149, 103.
118. D. Hohl; R. O. Jones; R. Car; M. Parrinello, *J. Chem. Phys.* **1988**, 89, 6823.
119. T. Yang; S. Okano; S. Berber; D. Tománek, *Phys. Rev. Lett.* **2006**, 96, 125502.
120. L. Zhechkov; T. Heine; S. Patschkovskii; G. Seifert; H. Duarte, *J. Chem. Theory Comput.* **2005**, 1, 841.
121. Y.-K. Kwon; D. Tománek; Y. H. Lee; K. H. Lee; S. Saito, *J. Mater. Res.* **1998**, 13, 2363.
122. Y.-K. Kwon; D. Tománek, *Phys. Rev. Lett.* **2000**, 84, 1483.
123. A. Rochefort; P. Avouris; F. Lesage; D. R. Salahub, *Phys. Rev. B* **1999**, 60, 13824.
124. A. A. Farajian; B. I. Yakobson; H. Mizuseki; Y. Kawazoe, *Phys. Rev. B* **2003**, 67, 205423.
125. Y. He; C. Zhang; C. Cao; H. P. Cheng, *Phys. Rev. B* **2007**, 75, 235429.
126. I. Vilfan, *Eur. Phys. J. B* **2006**, 51, 277.
127. D. Cakir; E. Durgun; O. Gülseren; S. Ciraci, *Phys. Rev. B* **2006**, 74, 235433.
128. I. Popov; T. Yang; S. Berber; G. Seifert; D. Tománek, *Phys. Rev. Lett.* **2007**, 99, 085503.
129. B. I. Yakobson; C. J. Brabec; J. Bernholc, *Phys. Rev. Lett.* **1997**, 76, 2511.
130. S. Gemming; G. Seifert, *Appl. Phys. A* **2006**, 82, 175.
131. Z. R. Zhou; L. Vincent, *Wear* **1999**, 229, 962.
132. M. D. Levi; D. Aurbach, *J. Power Sources* **2005**, 146, 349.
133. Y. R. Hacheco; R. Popovits-Biro; Y. Prior; S. Gemming; G. Seifert; R. Tenne, *Phys. Chem. Chem. Phys.* **2003**, 5, 1644.
134. N. Bertram; Y. D. Kim; G. Ganteför, *Appl. Phys. A: Mater. Sci. Process.* **to be published**.
135. N. Bertram; Y. D. Kim; G. Ganteför; Q. Sun; P. Jena; J. Tamueltine; G. Seifert, *Chem. Phys. Lett.* **2004**, 396, 341.
136. G. Seifert; J. Tamueltine; S. Gemming, *Comput. Mater. Sci.* **2006**, 35, 316.
137. X. D. Wen; T. Zeng; Y. W. Li; J. Wang; H. Jiao, *J. Phys. Chem. B* **2005**, 109, 18491.
138. M. Brändle; G. Calzaferri; M. Lanz, *Chem. Phys.* **1995**, 201, 141.
139. S. Brunet; D. Mey; G. Perot; C. Bouchy; F. Diehl, *Appl. Catal. A* **2005**, 278, 143.
140. H. Topsoe; B. Hinnemann; J. K. Nørskov; J. V. Lauritsen; F. Besenbacher; P. L. Hansen; R. G. E. Hytøft, R.G.; K. G. Knudsen, *Catal. Today* **2005**, 107, 12.
141. A. Logadottir; P. G. Moses; B. Hinnemann; N. Y. Topsoe; K. G. Knudsen; H. Topsoe; J. K. Nørskov, *Catal. Today* **2006**, 111, 44.

142. J. V. Lauritsen; M. V. Bollinger; E. Laegsgaard; K. W. Jacobsen; J. K. Norskov; B. S. Clausen; H. Topsøe; F. Besenbacher, *J. Catal* **2004**, 221, 510.
143. X.-D. Wen; T. Zeng; B.-T. Teng; F.-Q. Zhang; Y.-W. Li; J. Wang; H. Jiao, *J. Mol. Catal. A: Chem.* **2006**, 249, 191.
144. T. Zeng; X. D. Wen; Y.-W. Li; H. Jiao, *J. Mol. Catal. A: Chem.* **2005**, 241, 219.
145. J. M. Lightstone; M. J. Patterson; M. G. White, *Chem. Phys. Lett.* **2005**, 413, 429.
146. M. V. Bollinger; J. V. Lauritsen; K. W. Jacobsen; J. K. Norskov; S. Helveg; F. Besenbacher, *Phys. Rev. Lett.* **2001**, 87, 196803.
147. S. Gemming; G. Seifert, *Nat. Nanotechnol.* **2007**, 2, 21.
148. M. Bar-Sadan; A. N. Enyashin; S. Gemming; R. Popovits-Biro; S. Y. Hong; Y. Prior; R. Tenne; G. Seifert, *Phys. Chem. B* **2006**, 110, 25399.
149. R. Tenne, *Nature Nanotech.* **2006**, 1, 103.
150. P. Murugan; V. Kumar; Y. Kawazoe; N. Ota, *Phys. Rev. A* **2005**, 71, 063203.
151. W. Zhang; X. Ran; H. Zhao; L. Wang, *J. Chem. Phys.* **2004**, 121, 7717.
152. R. P. Diez, *Int. J. Quantum Chem.* **2000**, 76, 105.
153. V. Koteski; B. Cekić; N. Novaković; Belošević-Čavor, *Mater. Sci. Forum* **2005**, 494, 79.
154. D. Salloum; R. Gautier; P. Gougeon; M. Potel, *Solid State Commun.* **2004**, 177, 1672.
155. S. Picard; D. Salloum; P. Gougeon; M. Potel, *Acta Crystallog., Sect. C: Cryst. Struct. Commun.* **2004**, C60, i61.
156. Y.-W. Cao; R. Jin; C. Mirkin, *Science* **2002**, 297, 1536.
157. T. Li; I. Chao; Y. Tao, *J. Phys. Chem. B* **1998**, 102, 2935.
158. N. Krings; H. Strehlow; J. Kohnert; H. Martin, *Electrochim. Acta* **2003**, 49, 167.
159. R. Michalitsch; P. Lang; A. Yassar; G. Nauer; F. Garnier, *Adv. Mater.* **1997**, 9, 321.
160. P. Kornilovich; A. Bratkovsky; R. Williams, *Phys. Rev. B* **2002**, 66, 165436.
161. M. Rampi; O. Schueller; G. Whitesides, *Appl. Phys. Lett.* **1998**, 82, 1781.
162. A. Ghosh; P. Dample; S. Datta; A. Nitzan, *MRS Bull* **2004**, 29, 391.
163. J. Bourgoin; C. Kergueris; E. Lefevre; S. Palacin, *Thin Solid Films* **1998**, 327, 515.
164. J. Kristensen; J. Zhang; I. Chorkendorff; J. Ulstrup; B. L. Ooi, *Dalton Trans.* **2006**, 33, 3985.
165. J. M. Lightstone; M. J. Patterson; J. Lofaro; P. Liu; M. G. White, *Proceedings of the XIII International Symposium on Small Particles and Inorganic Clusters, Göteborg, Sweden* **2006**, p.155.
166. M. M. Biener; J. Biener; R. Schalek; C. M. Friend, *Surf. Sci.* **2005**, 594, 221.
167. D. V. Potapenko; J. M. Horn; R. J. Beuhler; Z. Song; M. G. White, *Surf. Sci.* **2005**, 574, 244.
168. *The ABINIT code is a common project of the Universite Catholique de Louvain, Corning Incorporated, and other contributors*, <http://www.abinit.org>.
169. R. Bader, *Atoms in Molecules: A Quantum Theory*. Oxford University: New York, 1990.
170. J. E. Huheey; E. A. Keiter; R. L. Keiter, *Inorganic Chemistry: Principles of Structure and Reactivity*. 4th ed. ed.; Harper Collins: New York, 1993.
171. Y.Q.Zhu; W. B. Hu; W. W. Hsu; M. Terrones; N. Grobert; T. Karali; J. P. Hare; P. D. Townsend; H. W. Kroto; D. R. M. Walton, *Adv. Mater.* **1999**, 11, 844.
172. L. J. Wan; M. Terashima; H. Noda; M. Osawa, *J. Phys. Chem. B* **2000**, 104, 3563.
173. K. Stokbro; J. Taylor; M. Brandbyge; J. L. Mozos; P. Ordejón, *Comput. Mat. Sci.* **2003**, 27, 151.
174. Z. -L. Li, B. Zou, and C. -K. Wang, *Phys. Rev. B* **2006**, 73, 075326.
175. N. D. Lang; C. R. Kagan, *Nanolett.* **2006**, 6, 2955.

176. N.D. Lang and A.R. Williams, *Phys. Rev. Lett.* **1976**, 37, 212.
177. M.S. Dresselhaus, G. Dresselhaus, and P. Avouris, *Carbon Nanotubes: Synthesis, Structure, Properties and Applications*. Springer: Berlin, 2001.
178. S. Heinze; J. Tersoff; R. Martel; V. Derycke; J. Appenzeller; P. Avouris, *Phys. Rev. Lett.* **2002**, 89, 106801.
179. N. Nemec; D. Tomanek; G. Cuniberti, *Phys. Rev. Lett.* **2006**, 96, 076802.
180. N. Park; D. Kang; S. Hong; S. Han, *Appl. Phys. Lett.* **2005**, 87, 013112.
181. P. Murugan; V. Kumar; Y. Kawazoe; N. Ota, *Nanolett.* **2007**, 7, 2214.
182. A. Kis; G. Csanyi; D. Vrbancic; A. Mrzel; D. Mihailovic; A. Kulik; L. Forro, *Phys. Stat. Sol. B* **2007**, 96, 076802.
183. P. Koskinen; H. Haekkinen; G. Seifert; S. Sanna; T. Frauenheim; M. Moseler, *New J. Phys.* **2006**, 8, 9.
184. I. Popov; S. Gemming; G. Seifert, *Phys. Rev. B* **2007**, 75, 245436.
185. I. Popov; T. Kunze; S. Gemming; G. Seifert, *Eur. Phys. J. D* **2007**, 45, 439.

## Acknowledgement

This thesis is dedicated to my mother **Verica** and father **Zlatoje**.

I am very thankful to:

**Sibylle Gemming** with whom I realized a productive cooperation from the beginning of my Ph.D studies and who shared generously with me her large experience in the material science and numerical calculations;

**David Tománek, Yang Teng** and **Savas Berber** on very inspiring and fruitful cooperation, which enthusiasm and expertise lifted my research one precious level further;

**Nitesh Ranjan, Gianaurelio Cuniberti, Alessandro Pecchia** and **Aldo di Carlo** for their programs for electronic transport and the support for them;

**Andrey Enyashin** for our interesting discussions and ideas born from them, as well as for nice friendship;

**Sergey Yurchenko** for large help during writing the thesis, for always intriguing discussions, as well as being a good partner for table tennis;

**Gotthard Seifert** for the chance to work in his group, and to realize my ambitions in the beautiful city of Dresden;

**Agnieszka Jaron-Becker, Agnieszka Kuc, Regina Luschtinetz, Luciana Guimarães, Igor Chaplygin, Robert Barthel, Bassem Assfour, Knut Vietze, Augusto Oliveira, Shinya Okano, Mathias Rapacioli, Johannes Frenzel, Thomas Heine, Lyuben Zhekov, Walter Alsheimer, Sandrine Hazebroucq, Viktoria Ivanovskaya, Gabriel Merino, Alberto Zobelli, Yuekui Wang, Siegrid Hehme** and others for any help and enjoying time spent together in last 4 years.



## **Versicherung nach § 5 Abs. 1 Nr. 5**

Versicherung nach § 5 Abs. 1 Nr. 5 der Promotionsordnung der Fakultät Mathematik und Naturwissenschaften an der Technischen Universität Dresden in der Fassung vom 16. April 2003:

- a) Hiermit versichere ich, dass ich die vorliegende Arbeit ohne unzulässige Hilfe Dritter und ohne Benutzung anderer als der angegebenen Hilfsmittel angefertigt habe; die aus fremden Quellen direkt oder indirekt übernommenen Gedanken sind als solche kenntlich gemacht. Die Arbeit wurde bisher weder im Inland noch im Ausland in gleicher oder ähnlicher Form einer anderen Prüfungsbehörde vorgelegt.
- b) Die vorliegende Arbeit wurde in der Arbeitsgruppe Theoretische Chemie am Institut für Physikalische Chemie an der Technischen Universität Dresden unter der wissenschaftlichen Betreuung von Prof. Gotthard Seifert angefertigt.
- c) Hiermit versichere ich, dass ich keine früheren erfolglosen Promotionsverfahren bestritten habe.
- d) Hiermit erkenne ich die Promotionsordnung der Fakultät Mathematik und Naturwissenschaften an der Technischen Universität Dresden in der Fassung vom 16. April 2003 an.

Datum

Unterschrift